

Département des Géosciences - Minéralogie et Pétrographie
Université de Fribourg (Suisse)

Characterization of Chrysotile, Tellurium and Imogolite Nanotubes

Thèse présentée à la Faculté des Sciences de l'Université de Fribourg (Suisse)

pour l'obtention du grade de *Doctor Rerum Naturalium*

par

Cédric Métraux
de Hermenches (VD), Suisse

Thèse N°1609

Imprimerie Saint-Paul

2008

Acceptée par la Faculté des Sciences de l'Université de Fribourg (Suisse) sur la proposition de :

Prof. Bernard Grobéty, Université de Fribourg, Suisse (Directeur de thèse)

Prof. Peter Ulmer, ETH Zürich, Suisse (Expert)

Prof. Andreas Züttel, EMPA, Suisse (Expert)

Prof. André Strasser, Université de Fribourg, Suisse (Président du Jury)

Fribourg, le 3 juillet 2008

Le Directeur de thèse :

A handwritten signature in blue ink, appearing to read 'B. Grobéty'.

Prof. Bernard Grobéty

Le Doyen :

A handwritten signature in blue ink, appearing to read 'Titus Jenny'.

Prof. Titus Jenny

Remerciements

Je souhaite remercier le professeur Bernard Grobéty pour m'avoir permis d'effectuer ce travail tout en ayant une activité professionnelle parallèle. Je remercie les professeurs Vincent Serneels et Marino Maggetti pour m'avoir accueilli au sein de l'institut de Minéralogie et Pétrographie.

Je tiens à exprimer toute ma gratitude à l'équipe du Département des Géosciences, Minéralogie et Pétrographie de l'Université de Fribourg, Jean-Paul Bourqui pour la préparation des échantillons, pour sa bonne humeur et ses encouragements, Christoph Neururer pour son aide au SEM et pour ses conseils avisés au four à induction magnétique, Odette Marbacher pour son aide à la LECO et notre secrétaire Nicole Brugger pour son travail administratif et sa force de persuasion.

Je souhaite remercier le Dr. Mohammed Dadras du Département de microscopie électronique du CSEM à Neuchâtel pour son aide au TEM. Je tiens aussi à exprimer ma gratitude au Prof. Peter Ulmer et au Dr. Andreas Hafner de l'ETHZ pour m'avoir initié aux expériences à hautes pressions et hautes températures.

Toute ma gratitude à l'ensemble des membres du Département des Géosciences de l'Université de Fribourg en particulier à mes collègues Folco Giacomini, Anna Lepora, Lenny Winkel, Jessica Chiaverini, Simonpietro di Pierro, Rémi Martineau, Sophie Wolf, Gisela Thierrin-Michael, Jeanne Bonzon, Giacomo Eramo, Peter Berner, Marco Schwab, Kuno Matzinger, Jacques Maradan, Gregory Barboni, Elisa Robledo, Andrea Storni, Pierre Vonlanthen, Luc Braillard, Damien Becker, Stephan Dall'Agnolo, Elias Samankassou, Sebastien Perret, Claire Blanc pour m'avoir fait connaître Romain Duris moi qui n'admirais que Fabrice Luchini, Cécile Bonnet, Maëlle Lhemon, Barbara Guenette-Beck et Martin Bochud.

Je remercie chaleureusement mes amis et complices de toujours Alexandre Junod, Fabrice Junod, Maxime Bagnoud, Charles Robert-Charrue, Olivier Boillod, Thomas Affolter et Olivier Sill qui m'ont aidé à maintenir le cap. J'exprime toute ma gratitude à mes parents et à ma soeur Florence pour leur soutien de chaque instant ainsi qu'à mes grands-parents qui n'auront malheureusement pas vu ce jour. Enfin je remercie par dessus tout mon amie Carole sans qui ce travail n'aurait ni commencé ni pris fin.

Contents

1	Abstract	2
2	Résumé	4
3	Introduction	6
3.1	Historical background	6
3.2	Nanowires and nanotubes	7
3.2.1	Carbon nanotubes	7
3.2.2	Structure of carbon nanotubes	9
3.2.3	Physical properties of carbon nanotubes	9
3.2.4	Applications of carbon nanotubes	11
3.2.5	WS ₂ and MoS ₂ nanotubes	11
3.2.6	BN nanotubes	12
3.2.7	Se nanorods	12
3.2.8	Te nanotubes	13
3.2.9	Chrysotile nanotubes	16
3.2.10	Imogolite nanotubes	16
3.3	Goals of the present work	16
3.4	Experimental Methods	17
3.4.1	Johannes type piston-cylinder pressure apparatus	17

3.4.2	Mercury porosimetry	17
3.4.3	Magnetic Induction Furnace	18
3.5	Analysis methods	18
3.5.1	Transmission Electron Microscopy	18
3.5.2	Scanning Electron Microscopy	20
3.5.3	X-ray diffraction	20
3.5.4	High temperature X-Ray diffraction	20
3.5.5	IR-spectrometry	20
4	Chrysotile nanotubes	22
4.1	Introduction	22
4.2	Crystallographic Structure	22
4.3	Thermal stability	26
4.4	Pore structure	33
4.5	Metal injection	33
4.5.1	Choosing the metals	36
5	Article: Filling of chrysotile nanotubes with metals	44
5.1	I. INTRODUCTION	45
5.2	II. EXPERIMENTAL	45
5.2.1	A. Starting materials	45
5.2.2	B. Thermal analysis of chrysotile nanotubes	46
5.2.3	C. Filling experiments with Hg	46
5.2.4	D. Filling experiments with Pb and Sn	46
5.2.5	E. Transmission Electron Microscopy	47
5.3	III. RESULTS AND DISCUSSION	48
5.3.1	A. Thermal properties of chrysotile nanotubes	48

5.3.2	B. Filling experiments with Hg	50
5.3.3	C. Filling experiments with Pb and Sn	50
5.4	IV. CONCLUSIONS	53
5.5	ACKNOWLEDGMENTS	54
5.6	REFERENCES	54
6	Tellurium nanotubes	56
6.1	Introduction	56
6.2	Physical vapor deposition principles	56
7	Article: Tellurium nanotubes and -rods synthesized by Physical Vapor Deposition	60
7.1	Abstract	60
7.2	I. INTRODUCTION	61
7.3	II. EXPERIMENTAL	62
7.3.1	A. PVD in an induction furnace	62
7.3.2	B. PVD in a high vacuum coating system	62
7.3.3	C. Electron microscopy	63
7.4	III. RESULTS AND DISCUSSION	63
7.4.1	A. Induction furnace	63
7.4.2	B. High vacuum coating system	68
7.5	IV. CONCLUSIONS	68
7.6	ACKNOWLEDGMENTS	69
7.7	REFERENCES	69
8	Imogolite nanotubes	71
8.1	Introduction	71
8.2	Potential and known applications	71

8.3	Synthesis	72
8.4	Formation	73
8.5	Crystal structure of the tube	73
8.6	Geometry of bundles	77
8.7	XRD calculations	77
8.8	Thermal stability	78
9	Article: Structural model and XRD calculations of imogolite aluminosilicate nanotubes	79
9.1	Abstract	79
9.2	Introduction	80
9.3	Structural Model	81
9.4	Experimental	84
9.5	Sensitivity of calculated XRD patterns to structural parameters	86
9.6	Fitting natural imogolite	87
9.7	Fitting synthetic imogolite	90
9.8	Simulation of the low angle region (4-13 2θ CuK α). The bundle geometry.	91
9.9	Discussion	93
9.10	Conclusions	94
9.11	Acknowledgements	94
9.12	References	95
10	Conclusions and outlook	97
	Appendices	97
A	XRD patterns on chrysotile nanotubes	98
B	IR spectrometry on chrysotile	103

CONTENTS	1
Bibliography	103
C Curriculum Vitae	120

Chapter 1

Abstract

The discovery of C60 (R. Smalley et al.) and carbon nanotubes CNTs (S. Iijima) in 1985 and 1991 respectively was a milestone in the field of nanoscience. Since 1991, WS₂, MoS₂, BN, Se, Te nanotubes were synthesized and analyzed. These nanotubes are promising materials for many applications in the field of catalysis, electronic, polymer synthesis, etc. In this study, we characterized the crystallographic and chemical properties of two natural and one synthetic nanotubes: 1) chrysotile nanotubes 2) tellurium nanotubes and 3) imogolite nanotubes. An introductory chapter gives general information on the crystallography, crystal chemistry, thermal stability, synthesis of the materials. A second chapter contains a published or submitted paper on a specific aspect of the treated nanotube material.

The first nanotube material presented is chrysotile, which is nanotubular mineral of the serpentine family. A formalism derived from the description of carbon nanotubes has been developed. A potential application of chrysotile nanotubes as template for metallic nanowires manufacturing is proposed. An important parameter for such a procedure is the thermal stability of the nanotube. We show that chrysotile dehydroxilation takes place around 490°C and that the tubular morphology is stable up to 700°C (at atmospheric pressure). Metals with a melting temperature under 700°C can potentially be injected in chrysotile nanotubes to produce metallic nanowires. Successful injections of Mercury and Lead were performed under high pressure conditions (4-10 Kbar).

In the second case study the synthesis of tellurium nanotubes through physical vapor deposition (PVD) is presented. Tellurium is a metallic element used for the synthesis of semiconducting materials such as Bi₂Te₃, CdTe and ZnTe. The synthesis of tellurium nanotubes through wet chemical routes has already been achieved by several research groups. In this study we show that tellurium nanotubes can also be synthesized through physical vapor deposition between 150°C and 200°C without using any catalyst or template. The nanotubes show a crystallographic preferred orientation relative to the silicon wafer used as target, the (001) plane of the tellurium nanotubes being parallel to the (111) plane of the silicium.

In the third case study the tubular and bundle crystallographic structure of imogolite nanotubes is investigated. Imogolite is a natural nanotubular mineral discovered in volcanic soils of the Kyushu Island (Japan). Imogolite can also be synthesized through aqueous solution. A numerical rigid-body model of the structure of individual imogolite nanotubes and bundles has been developed and

calculations of powder X-ray patterns were performed. The structural model proposed by Cradwick et al. in the '70 is confirmed. We show that the 'bundle geometry' of imoglite can be monoclinic or tetragonal. The X-rays patterns calculated in this study may eventually be used in future work and may permit better interpretations of the measured x-rays spectrums.

Chapter 2

Résumé

La découverte de la molécule de C60 en 1985 (R. Smalley et al.) et celle des nanotubes de carbone (CNTs) en 1991 (S. Iijima) ont lancé nombre de scientifiques sur la voie des nanosciences. Depuis les années '90, des nanotubes de WS₂, MoS₂, BN, Se, Te, etc. ont été synthétisés et analysés ainsi que de nombreux autres 'nanomatériaux'. Ces matériaux présentent un fort potentiel d'application dans des domaines aussi variés que la catalyse, l'électronique, la synthèse des polymères, etc. Cette étude a pour but de caractériser d'un point de vue cristallographique et minéralogique trois types de nanotubes ainsi que de proposer de potentielles applications. Les trois nanotubes étudiés sont 1) les nanotubes de chrysotile, 2) les nanotubes de tellurium et 3) les nanotubes d'imogolite. Ces trois formes de nanotubes sont abordées par un chapitre d'introduction où leurs caractéristiques générales (cristallographie, stabilité thermique, synthèse, etc.) sont exposées puis par un article publié (ou en voie de publication) traitant d'un aspect plus spécifique.

La première étude est consacrée à une analyse de la stabilité thermique et de la structure cristallographique de 8 échantillons de nanotubes de chrysotile. Le chrysotile est un minéral nanotubulaire de la famille des serpentinites. Un formalisme cristallographique proche de celui employé pour la classification des nanotubes de carbone est proposé. Il est montré que la dehydroxylation des nanotubes de chrysotile débute aux alentours de 490°C mais que la structure tubulaire est stable jusqu'à 700°C (à pression atmosphérique). Une application potentielle des nanotubes de chrysotile utilisés en tant de "moules" pour l'injection de nanofils métalliques est présentée. Les métaux ayant une température de fusion inférieure à 700°C sont potentiellement injectables dans les tubes de chrysotile afin de produire de nanofils métalliques. Des injections de mercure et plomb ont été effectuées sous haute pression (4-10 Kbar) avec succès.

La deuxième étude présente la synthèse par "dépôt physique en phase vapeur" de nanotubes et nanofils de tellurium dans un four à induction magnétique. Le Tellurium est un élément métallique rentrant dans la composition de nombreux composants semiconducteurs tels le Bi₂Te₃, le CdTe et le ZnTe. La synthèse de nanotubes de tellurium par voie chimique a été réalisée par différents groupes de recherche. Dans cette étude, nous démontrons que la synthèse de nanotubes de tellurium est également réalisable par dépôt physique en phase vapeur entre 150°C et 200°C sans utilisation de catalyseur. Les nanotubes obtenus présentent une orientation cristallographique préférentielle par rapport au support de silicium utilisé comme cible lors de la synthèse, le plan (001) des nanotubes

de tellurium étant parallèle au plan (111) du silicium.

Dans la troisième étude, la structure cristalline tubulaire et l'organisation spatiale (en 'bundle') de nanotubes d'imogolite sont analysées. L'imogolite est un minéral naturel de forme nanotubulaire découvert dans des sols volcaniques de l'île de Kyshu (Japon), pouvant être synthétisé en laboratoire par chimie douce. Il est montré par simulation informatique d'un modèle rigide cristallographique et par calculs de spectres de rayons-X que la structure proposée par Cradwick et al. dans les années '70 est correcte. Il est également démontré que la géométrie des groupes des nanotubes ('bundles') est monoclinique ou tétragonale. Les spectres de rayons-X calculés pour différentes configurations du modèle rigide permettront dans le futur une meilleure interprétation des spectres expérimentaux.

Chapter 3

Introduction

In this chapter we would like to shortly depict the history of the concepts that led to the discovery of nanotubular carbon, which ignited an intense research activity to understand the physical properties and to look for potential applications of such materials. The structure, synthesis and properties of the nanotube material dealt in this thesis i.e. chrysotile, tellurium nanotubes and imogolite will be introduced with the help of concepts from the description of carbon nanotubes.

3.1 Historical background

In 1985, two physicists from Rice University R. Smalley and R. Curl, Houston, Texas, USA and H. Kroto from the University of Sussex, UK, discovered a new kind of carbon they called C₆₀ [1]. This molecule consists of 60 carbon atoms organized as a combination of regular polyhedrons showing hexagonal as well as pentagonal faces. The C₆₀ molecule was named "fullerene" (see fig. 3.1) after the name of an american architect called R. Buckminster Fuller who designed the geode building (the american pavilion) of the Montreal Universal Exposition in 1967 which shape is similar to the fullerene's shape. Until 1985, only two forms of crystallized carbon were known i.e. diamond (isomeric or hexagonal) (see fig. 3.2) and graphite (hexagonal) (see fig. 3.3). Five years later, in 1990, W. Krätschmer and D. Huffman from the University of Heidelberg, Germany, were able to synthesize substantial amounts of fullerene allowing bulk physical as well as bulk chemical studies of these new material. The discovery of C₆₀ has focused the attention of many researchers on nanosized materials. In 1991, using transmission electron microscopy (TEM), S. Iijima from NEC laboratories in Tsukuba, Japan, identified for the first time Multiwalled Carbon Nanotubes as by-products of fullerene synthesis [3]. The same year he and Bethune discovered "Single Walled Carbon Nanotubes". Carbon nanotubes are tubular structures with a radius of up to tenth nanometers and a length ranging from nanometers to millimeters. They consist of a rolled up graphene sheet which is closed at each end by two half-fullerenes. Carbon nanotubes have immediately attracted the curiosity of many scientists because their properties fall in the range where quantum effects become important [4]. In 1992, scientists at the Weizmann Institute suggested that layered metal dichalcogenides could form tubular nanostructures. They were able to synthesize crystalline molecular cylinders composed of Tungsten and Sulfur (WS₂) [5]. Before this

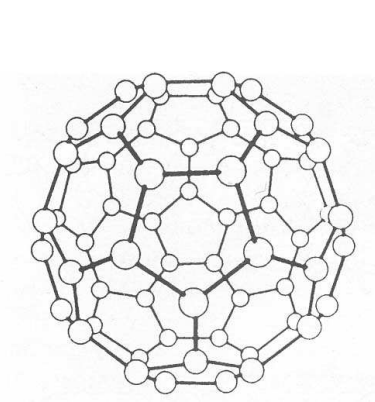


Figure 3.1: C60 ([2]).

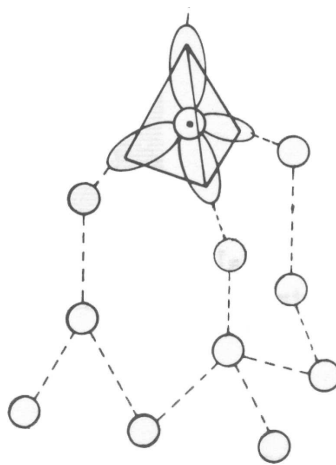


Figure 3.2: Diamond.

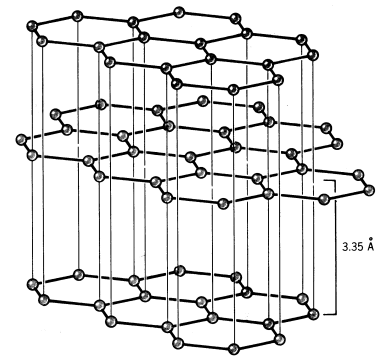


Figure 3.3: Graphite.

experiment it was believed that only carbon could form geometrically closed structures because the strain involved for other elements or compounds was thought not to allow stable closed structures to exist. The only known exceptions were the layered minerals chrysotile (asbestos) and imogolite which occur as open, cylindrical structures similar to the concentric tubes of graphite and which are the subject of two parts of this study.

3.2 Nanowires and nanotubes

3.2.1 Carbon nanotubes

Because their discovery triggered intense research activity in the field of nanoscience, we will shortly describe the physical and chemical properties of carbon nanotubes. This will allow us to better understand mineral nanotubes.

Synthesis methods and growth mechanisms of carbon nanotubes

The arc evaporation technique is the original method used by Krätschmer and Huffman to produce C60. S. Iijima used this method to synthesize the first recognized carbon nanotubes (both multi- and single walled carbon nanotubes) [3]. Many other synthesis techniques leading to the formation of carbon nanotubes have been developed since [6]. The Chemical Vapor Deposition method (CVD-method) uses hydrocarbon decomposition (acetylene, benzene, pentane, carbon monoxide, etc.) on different metals such as Co and Fe at temperatures between 500°C and 1200°C in a reaction furnace (often consisting of a quartz tube inserted in an electrical furnace) [6]. The CVD gas-phase technique does not use any substrate; the catalysts are vaporized in the CVD reactor in the form of organometallic molecules. Plasma assisted chemical vapor deposition (PACVD) is a third type of CVD. Here carbon is deposited over a metallic substrate through a plasma mixture of CH₄ and H₂. Another method called laser-ablation (see fig. 3.4) produces carbon nanotubes by directing a laser

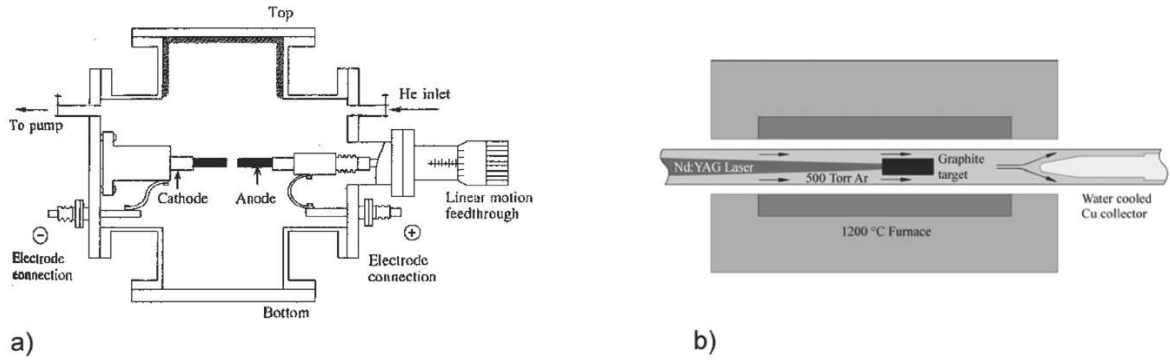


Figure 3.4: a) Arc discharge method b) Laser ablation method (after P.J.F. Harris [2]).

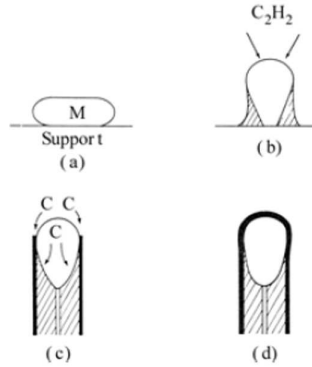


Figure 3.5: Possible carbon nanotube growth (after P.J.F. Harris [2]).

beam onto a graphite target placed in an electrical furnace (heated to 1200°C) under argon flux. The argon flux (at a pressure about 500 Torr) transports the carbon nanotubes on a water-cooled Cu collector placed at the other end of the furnace.

The growth mechanism of carbon nanotubes clearly depends on the presence of catalysts e.g. Fe, Co (CVD) or not (laser ablation, arc evaporation technique). A model where a metal particle is used as catalyst for carbon fiber growth has been proposed already in 1972 by Harris and co-workers [2]. Here, the carbon which is part the hydrocarbon molecule used for the synthesis (e.g. acetylene) is dissolved in the metal catalyst (e.g. Ni) releasing hydrogen atoms in the reacting chamber. Supersaturation on the contact between substrate and catalysis particle leads to carbon precipitation at the surface (see fig. 3.5). Under certain conditions the precipitate form cylindrical sheets [2].

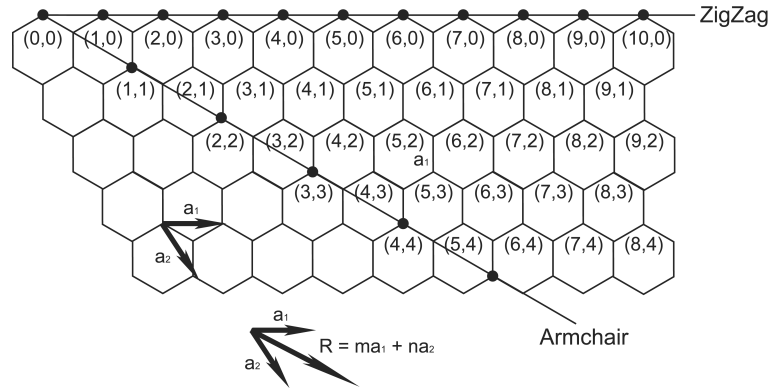


Figure 3.6: Scheme that shows the folding procedure to create carbon nanotubes according to the notation of Dresselhaus (modified after P.J.F. Harris [2]).

3.2.2 Structure of carbon nanotubes

The cylindrical portion of the tube consists of a single graphene sheet, rolled to form a cylinder. An important parameter, the helicity, can be described by the "helical vector" $[R = ma_1 + na_2]$, where m and n form a pair of integers and a_1 a_2 are the primitive lattice vectors of the hexagonal lattice. The vector indicates the direction in which the graphene sheet is rolled, and the end points of the vector indicate where the sheet connects after one full rotation. An armchair nanotube is defined by a $(m, n = m)$ R vector and a zigzag nanotube is defined by a $(m, 0)$ R vector see (fig. 3.6).

Two categories of carbon nanotubes are distinguished based on the number of graphene sheets. The first category called "multiwalled carbon nanotube" (MWCNT) is made of concentric cylinders placed around a central hollow. The second called "single walled carbon nanotube" (SWCNT) consists of one graphene sheet.

3.2.3 Physical properties of carbon nanotubes

Carbon nanotubes show high material properties such as electrical and thermal conductivity, strength, stiffness, and toughness. The well-known position of the C atoms in the structure of carbon nanotubes permits precise theoretical modeling of their physical properties [7]. The physical properties of the nanotubes depend on the structure (diameter, helicity, multi-walled, single-walled). Their electronic conductivity, for example, depends sensitively on tube diameter and helicity, only slight differences in these parameters cause a shift from a metallic to a semiconducting state. Armchair nanotubes are metallic. Zigzag and helical nanotubes are metallic or semiconducting [2].

The electronic structure of carbon nanotubes has been studied by Wildöer et al. [8] and Odom et al. [9] by scanning tunneling microscopy (STM) on individual single-walled nanotubes. The bias voltage is applied to the sample. Current-voltage curves obtained by tunneling microscopy, show a low conductance at low bias followed by several kinks at larger bias voltages (see fig. 3.7). The derivatives curves dI/dV allows a better interpretation of current variation as function of bias

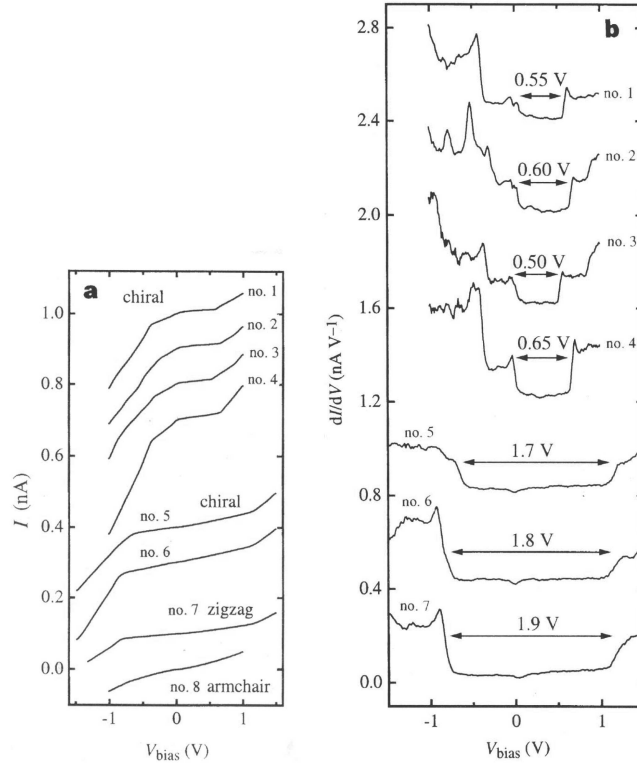


Figure 3.7: a) Current-voltage curves. b) dI/dV curves (after Wildöer et al. [8]).

voltage and are proportional to the density of states (DOS) of the tube examined. dI/dV curves show two categories of gap values (between 0.5-0.6 eV and between 1.7-2.0 eV) (see fig. 3.7). The first category of tubes is identified as semiconducting, the second category of tubes is identified as conducting. The STM spectra show densities of states with similar singularities to those obtained by band calculations [10].

The energy gap E_{gap} of semi-conducting (zigzag, helical) nanotubes is a function of the tube's diameter (see fig. 3.8) and can be modeled by the following function describing the semiconducting properties of carbon nanotubes [8]:

$$G(E) = \frac{2y_0a_{cc}}{d} \quad (3.1)$$

Where y_0 (2.7 eV) is the C-C tight bounding overlap energy ($y_0 = 2.5$ eV for a single graphene sheet), a_{cc} the nearest neighbor C-C distance (0.142 nm), and d the tube diameter. With tube diameters ranging from a minimal value of 1.0 nm and a maximal value of 2.5 nm, it follows that the energy gap E_{gap} ranges from 0.3 eV to 0.8 eV.

The studies on the electrical properties of carbon nanotubes showed that within the graphene layers, electron mobility is high, but perpendicular to the planes relatively low depending on the degree of crystalline order. Moreover, the conductance of a nanotube is quantized and a carbon nanotube acts as a ballistic conductor [11]. Carbon nanotubes also show a constant resistivity and a tolerance

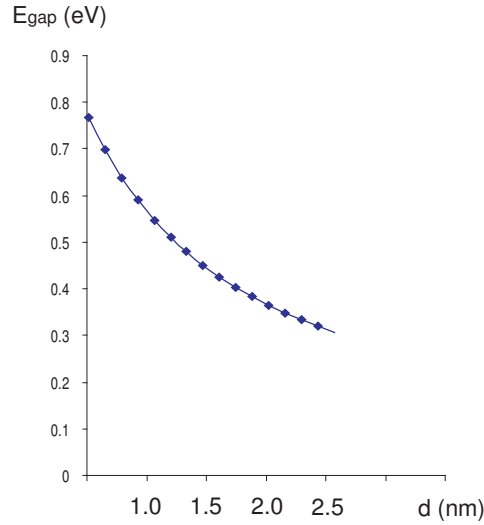


Figure 3.8: Energy gap (E_{gap}) versus diameter d computed for a semiconducting chiral nanotube.

for very high current density. Stephan Frank et al. [12] contacted carbon nanotubes with a mercury surface, the experiment revealed that the nanotubes behaved as a ballistic conductor with quantum behavior. The conductance increases by increments of 1 G_0 ($G_0 = \frac{2e^2}{h} \approx (12.9k\Omega)^{-1}$) [13]. The values of G_0 could also take some non-integer value such as 0.5 G_0 . This has been explained later by Sanvito et al. [13] because of the blocking of some conductance channels by inter-wall reactions (see fig. 3.9).

3.2.4 Applications of carbon nanotubes

The fields of application of carbon nanotubes range from field emission [14] [15], molecular electronics [16] [17] [18], catalysts supports, hydrogen storage [19], conductive plastics, structural composites [20], thermal materials [21]. Most of them have not yet been turned into commercial products.

3.2.5 WS_2 and MoS_2 nanotubes

After the overview of carbon nanotubes structure and properties, we will now examine other 1-D nanowires and nanotubes. As stated above, nanotubes of WS_2 have been first produced and characterized by Tenne et al. [5]. They produced WS_2 nanotubes by annealing tungsten films on quartz substrates at 1000°C in H_2S under a reducing atmosphere. WS_2 nanotubes consist of a repeating motif of S-W-S layers with covalent tetrahedral W-S bonds and weak van der Waals bonds holding the sheets together. MoS_2 nanotubes which are similar to WS_2 nanotubes were synthesized by Feldman et al. in 1995 [22]. To produce MoS_2 nanotubes Feldman et al. reacted the gases MoO_3 and H_2S in an argon atmosphere. This technique has been improved by Nath et al. by using the direct decomposition of $(NH_4)_2MoS_4$ heated in a stream of H_2 at 1200-1300°C [23]. The tubes obtained by this method have a typical outer diameter of 30-45 nm and an inner diameter of 7-8 nm. They produced WS_2 through a similar procedure involving the decomposition

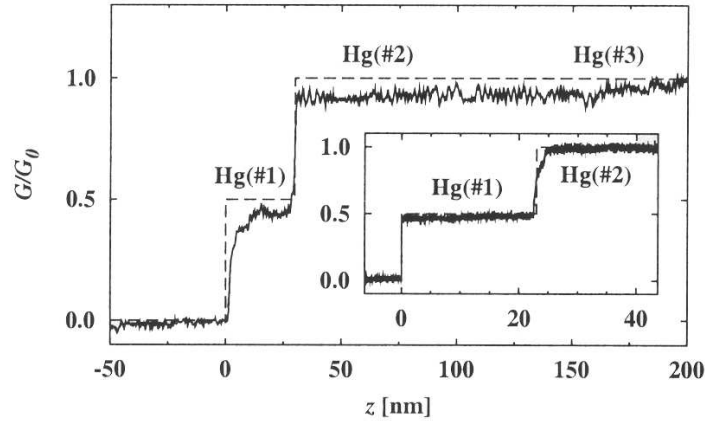


Figure 3.9: Ballistic conductance G of multiwall carbon nanotubes as function of immersion depth z in mercury (after Sanvito et al. [13]).

of $(\text{NH}_4)_2\text{WS}_4$ in presence of H_2 at temperatures between 1200°C and 1300°C . The tubes obtained through this method have an outer diameter of 25 nm.

3.2.6 BN nanotubes

BN nanotubes were synthesized by Chopra et al. using a plasma discharge apparatus similar to that used for the production of carbon fullerenes [24]. Here the anode is made using a pressed rod of hexagonal BN inserted into a hollow tungsten electrode. Controlling the arc conditions is difficult and other methods have been developed to get better BN yields. For example, BN nanotubes have been produced by the arc-melting method from boron and metal powder compacts in a nitrogen/argon gas atmosphere [25]. Ultra-high-repetition rate laser ablation has also been used apparently leading to a lower yields of BN nanotubes [26] (see fig. 3.10).

3.2.7 Se nanorods

Selenium, an important elemental semiconductor has useful properties in many applications. Among others selenium is known as photoconductor with a special sensitivity covering almost the entire visible range [27]. This makes selenium useful in the production of photocells. In 2001, Mayers et al. [28] synthesized Se/Te nanorods in an aqueous medium through the in situ reduction of selenious acid and orthotelluric acid with excess hydrazine:



The structure is the same as for the pure endmembers and the Se and Te atoms are distributed along the chains orientated parallel to the c -axis (see fig. 3.11). The reduction of selenious acid (H_2SeO_3) using the protein cytochrome c_3 also appeared to be a suitable route to produce monoclinic selenium nanowires with a polycrystalline structure [29]. The reduction of selenious acid with excess hydrazine by the solution refluxing approach allowed the production of trigonal selenium nanowires

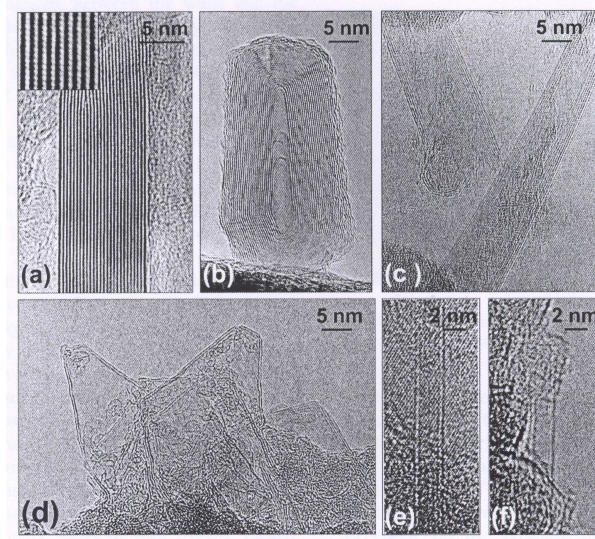


Figure 3.10: Laser ablated BN nanostructures. a) nanorods, b) nested nanoparticle, c) multiwalled nanotubes, d) 'nanohorns', e) double-layered nanotube and f) single-layered nanotube (after D. Goldberg et al. [26]).

[30]. Production of selenium nanorods was reported using the laser ablation technique by Jiang and co-workers [31]. Many 1-D nanostructures have been synthesized such as Ag_2Se nanowires, CdSe nanotubes, Se@CdSe nanocables, and Pt nanotubes by templating against Se nanowires [32].

3.2.8 Te nanotubes

Tellurium is an important semiconducting material (similar to selenium). This element can also react with many other substances to form a range of technologically important materials such as Bi_2Te_3 , CdTe and ZnTe . Due to the lack of a centrosymmetry, the trigonal phase of tellurium (as well as for selenium) exhibits piezoelectricity stronger than that of quartz or CdS [28]. In 1972 Furuta et al. produced tellurium whiskers by sublimation of metallic tellurium on the surface of a platinum substrate (see fig. 3.12) [33]. In 2002, Mayers et al. reported the first synthesis of trigonal tellurium nanotubes (*t*-Te nanotubes) using the polyol process developed by Fievet et al (see fig. 3.13) for generating colloidal particles of metals [34]. The procedure used a pure ethylene glycol (the polyol which served as solvent and reducing agent) refluxed at temperatures above 100°C to which orthotelluric acid (H_6TeO_6) was added. Nuclei formed during the reducing phase have a strong tendency to grow along the *c*-axis.

Single crystalline tellurium nanotubes have also been synthesized through the so-called 'solvothelmal process' involving a porous silica (MCM-41) used as growth assistant [35]. In the solvothelmal process, the solvent plays an important role in the nucleation of nanocrystalline. A mixture of tellurium powder, KOH and MCM-41 is put into a teflon-lined autoclave which is filled with the solvent (N,N dimethylformamide) and maintained at 180°C for 24 hours. Tellurium nanotubes are the subject of chapters 6 and 7.

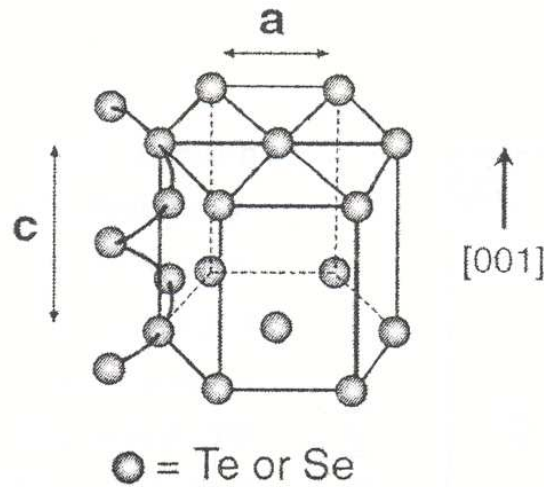


Figure 3.11: The hexagonal lattice of $\text{Se}_{0.5}\text{Te}_{0.5}$ trigonal alloy nanotubes. Se and Te atoms are distributed along a spiral chain (screw axis) parallel to the c-axis (after B. Mayers et al. [28]).

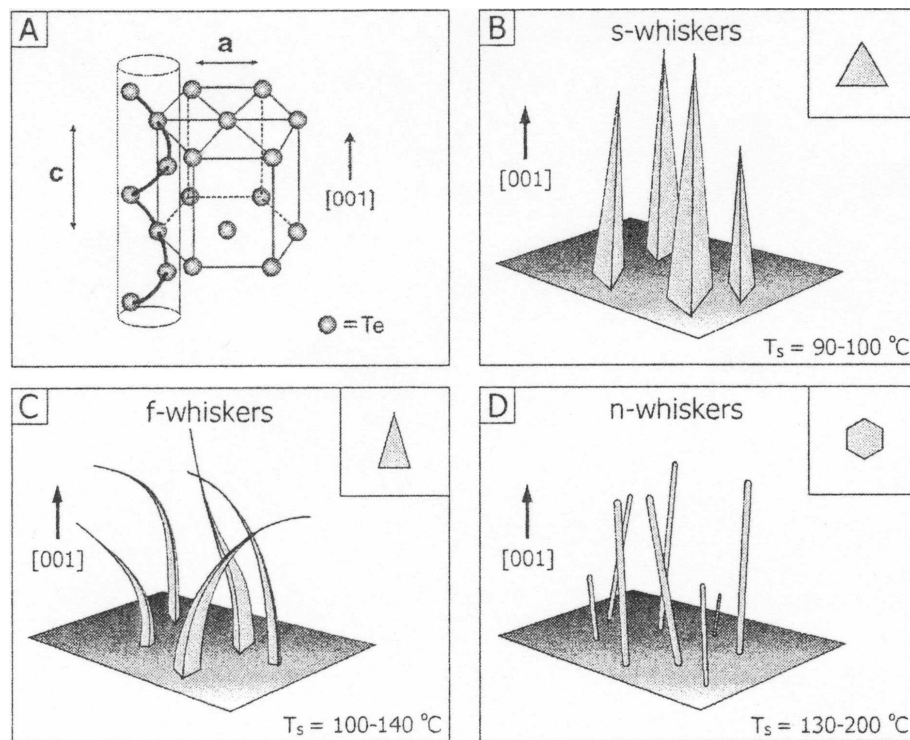


Figure 3.12: a) The basic building-block of trigonal tellurium nanotubes is an helical chain of covalently bound tellurium atoms. These chains are connected among each other by van der Waals forces. Such a structure tends to grow along the [001] direction. Many different morphologies are produced from vapor phase depending on the temperature b) triangular whiskers c) filamentary whiskers and d) needle-like whiskers (after N. Furuta et al. [33] and B. Mayers et al. [36]).

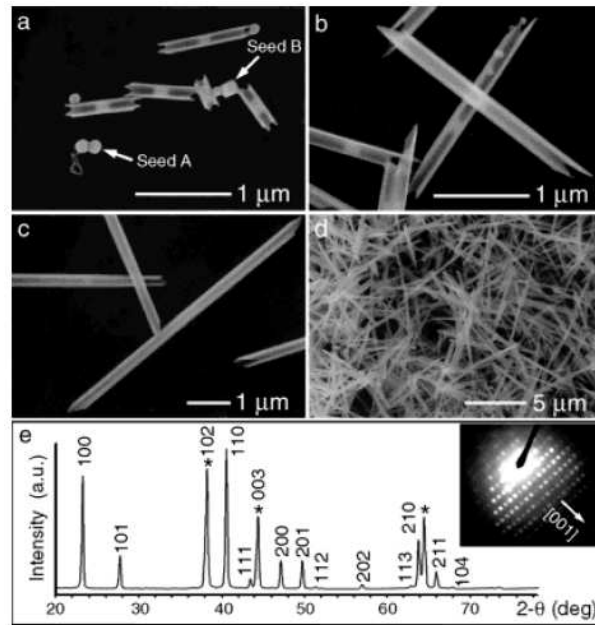


Figure 3.13: Tellurium nanotubes synthesized through the polyol process. a), b), c) and d) SEM pictures of tellurium nanotubes. e) XRD pattern of tellurium nanotubes (electron microdiffraction in inset) (after B. Mayers et al. [37]).

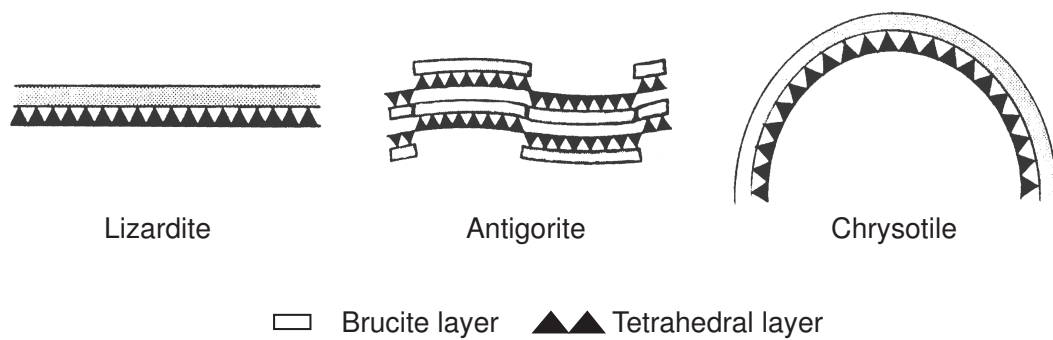


Figure 3.14: Three members of the serpentine mineral group: Antigorite, the wavy form. Lizardite, the platy form and chrysotile, the tubular form (after J.D. Dana [38]).

3.2.9 Chrysotile nanotubes

Chrysotile, with formula $(\text{Mg}_3\text{Si}_2\text{O}_5(\text{OH})_4)$, is a mineral of the serpentine group (phyllosilicate) which has the morphology of nanotube with an inner diameter of about 5 nm. Two other minerals belong to the serpentine group: antigorite and lizardite (see fig. 3.14). Antigorite has a wavy structure and forms a polysomatic series between lizardite and talc. The known members have stoichiometries which are Mg-deficient relative to chrysotile and are, therefore, not true polymorphs of chrysotile. Lizardite is a true polymorph of chrysotile but with flat layers. Chrysotile can be found in metamorphosed and hydrothermally-altered ultra-basic rocks. Bates et al. postulated in 1950 that the tubes are formed as the result of the bending of the silicate-magnesium hydroxide layers in order to retrieve the strain induced by differences in dimensions between the tetrahedral sheet and the octahedral sheet, which are present in the layers [39]. Chrysotile nanotubes are the subject of chapters 4 and 5.

3.2.10 Imogolite nanotubes

Imogolite, with formula $(\text{OH})_3\text{Al}_2\text{O}_3\text{Si}(\text{OH})$ is a nanotubular hydrated aluminum silicate discovered in Japan, Kyushu Island (1962) in soils (imogolayer) derived from volcanic ashes [40]. Imogolite has a cylindrical point group C_{2nh} . Imogolite can also be synthesized in laboratory using mild chemistry. The first synthesis of imogolite (1977) was performed heating weakly acidic dilute solution of hydroxy aluminum orthosilicate [41]. The tubular structure of the mineral was resolved by Cradwick et al. [42]. Imogolite nanotubes are the subject of chapters 8 and 9.

3.3 Goals of the present work

The initial goals of the present work were to investigate 1) the structure 2) the thermal stability and 3) potential applications of **chrysotile and imogolite mineral nanotubes**. The preparation of porous and high aspect ratio nanotubes and wires without the necessity for costly and complex processing is still a major challenge [43]. In this context mineral nanotubes may be good candidates for 1) nanowires manufacturing using a template methode (see fig. 3.15 for Alumine templates) 2) catalyst support 3) gas storage 4) ion-channel devices 5) PVA films manufacturing. The key advantage of such materials is clearly their low cost. On the other hand, a disadvantage is the difficulty to get organized arrays (bundles) of such natural (or produced through mild chemistry) products.

During templating experiment with physical vapor deposition against chrysotile nanotubes in order to produce metallic nanowires, we discovered accidentally that tellurium nanotubes could also be produced through Physical Vapor Deposition (PVD), which was not reported in the literature. Therefore, we decided to investigate the formation of tellurium nanotubes through PVD in more details extending the initial theme to a new kind of nanotubes. These results have been reported in chapters 6 and 7.

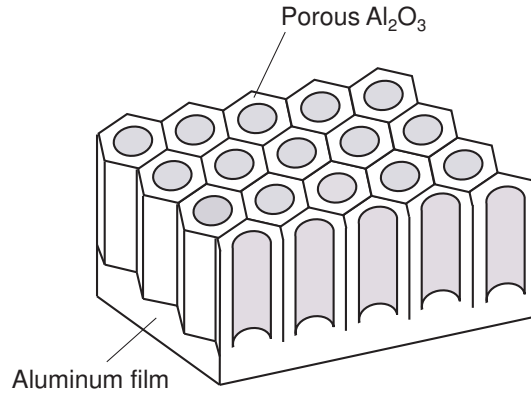


Figure 3.15: Scheme of the template method used to produce nanowires. For example, an hexagonal alumine (Al_2O_3) template lattice can be used. Nanowires are injected under pressure or deposited in the alumine channels (modified after W.I. Park et al. [44]).

3.4 Experimental Methods

3.4.1 Johannes type piston-cylinder pressure apparatus

Injection experiments with Pb, Sn, Al and Cu into chrysotile templates were performed with a non end-loaded piston-cylinder apparatus. Temperature and pressure were calibrated against the melting point of the LiCl albite-jadeite-quartz equilibrium (600°C, 16.4 kbar, [45]) and the fayalite-quartz-orthoferrosilite equilibrium at 1000°C and 14.1 kbar [46]. Pressure was measured with a load cell and was kept constant during the experiments to within ± 50 bars of the nominal value which is accurate to within 0.3 kbar. Temperatures were measured using sheathed alumel - chrome (type K) thermocouples and the temperature stability was better than $\pm 2^\circ\text{C}$. NaCl assemblies with 19 mm OD and 10 mm OD cylindrical graphite heaters were used as pressure medium for all experiments. Heating rate was about $30^\circ\text{C}/\text{min}$ and dwell time was 15 min. At the end of the experiments, the furnace was shut down leading to a near-isobaric quench with rates $> 200^\circ\text{C}/\text{second}$. Information on capsule type and sizes can be found in chapter 5.

3.4.2 Mercury porosimetry

Injection experiments with Hg into chrysotile templates, were performed with a Micromeritics model Autopore II 9220 Hg-porosimeter (West-Lafayette, IN, USA) (see chapter 4). The maximal pressure of 414 MPA (4,14 Kbar) produced by the apparatus should, according to the Young-Laplace equation, allow to fill pores with a radius as small as 1 nm. The samples (chrysotile nanotubes) were placed in a cup, evacuated for 30 min and mercury was slowly added at room temperature and finally the liquid pressure was raised up to 4 Kbar. Mercury porosimetry was used to fill chrysotile nanotubes with Hg but not to study the distribution of the pores sizes. The amount of nanotubes (20 mmg) was too small compared to the volume of the sample holder (3.12 mL) and the cumulative intrusion curve (mL/g) for nanometric pores too flat for a proper pore distribution study at the nanometric scale (see fig. 3.16).

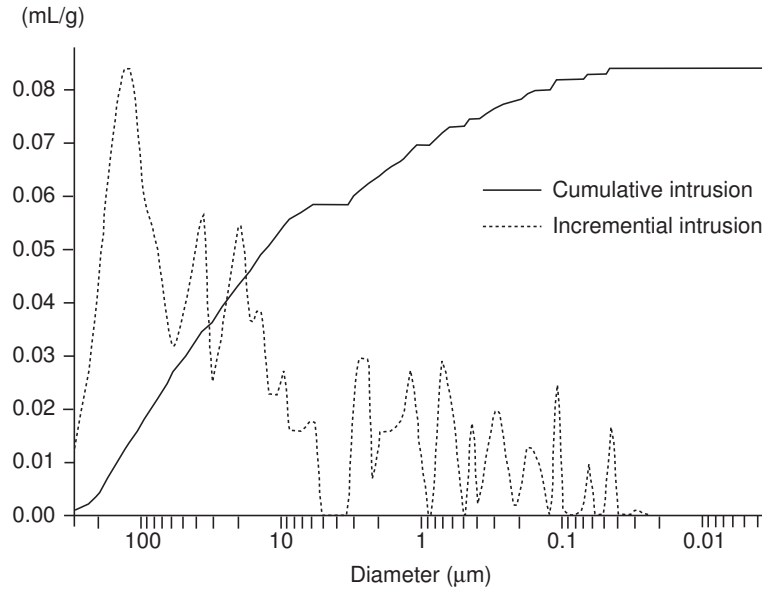


Figure 3.16: Mercury porosimetry. Cumulative intrusion and incremental intrusion curves. In this case, the volume intruded at the nanometric scale is extremely small.

3.4.3 Magnetic Induction Furnace

For physical vapor deposition (PVD) experiments (see section 3.3), a magnetic induction furnace was used. The power supply of the furnace could be raised up to 24 KW and the frequency up to 200 KHz. Before PVD was performed, the quartz tube in which the experiment was done was evacuated by a turbo pump to 2×10^{-7} mbar (see fig. 3.17). Argon was then flushed in the quartz tube until the pressure of 1 mabr was reached. Finally a graphite rod, used as sample holder (on which was deposited 0.05 g of the material to be vaporized) was heated though magnetic induction. The temperature of the graphite rod was controlled through a laser pyrometer. The produced vapor was deposited on (111) silicon wafers or polycrystalline aluminum plates. Pressures between 1013 mbar and 1×10^{-2} mbar were controlled by a Pirani pressure gauge. Pressures between 1×10^{-2} mbar and 1×10^{-6} mbar were controlled by a Penning pressure gauge (relative error for pressure measurement is about 20%).

3.5 Analysis methods

3.5.1 Transmission Electron Microscopy

Two transmission electron microscopes (TEM) were used during this work. The first one was a Philips CM10 operating at 100 kV for rapid control and the second one a Philips CM200 equipped with an EDAX dispersive spectrometer operating at 200 kV for high resolution and analytical work. The specimens were, in both cases, placed on 300 mesh Cu Lacey-Kohlefilm of 3.05 mm diameter (from Plano GmbH). The 100 kV (CM10) TEM was used for a rapid control of the experimental

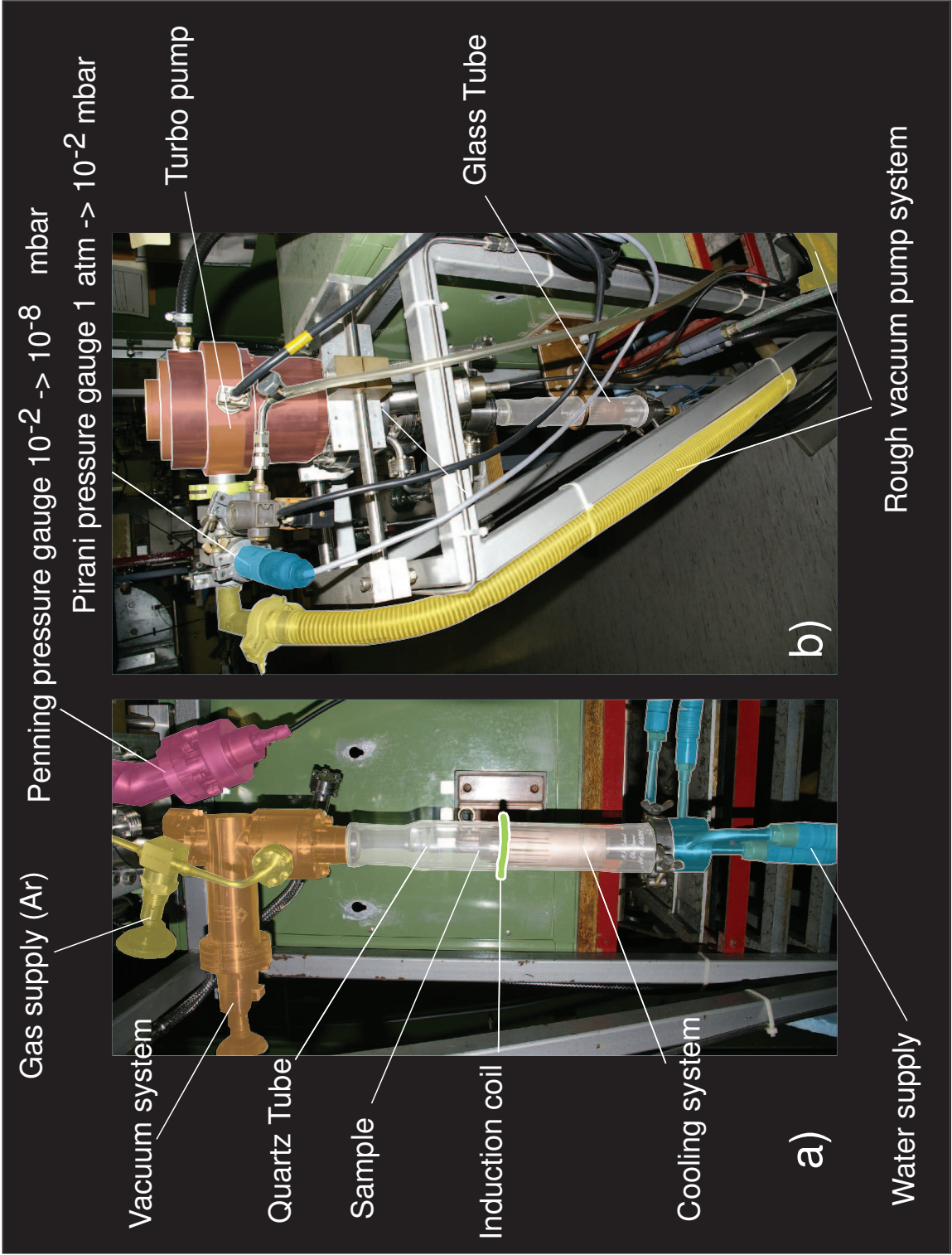


Figure 3.17: a) Frontal view of the magnetic induction furnace used for PVD with glass tube, vacuum system, cooling system. b) Lateral view with molecular pump.

results and the 200 kV (CM200) TEM for analysis requiring diffraction patterns, selected area electron diffraction (SAED) and energy dispersive spectra (EDS) analyses. The use of the higher voltage microscope helped also to reduce beam damage. There are two damage mechanisms 1) radiolysis damage and 2) knock-on damage. The former being reduced at higher beam energies. The specimen heating is high for ceramics and insulators and lower for metalloids and metals [47]. Beam heating can be reduced by using the highest available voltage. If the material is thinner than the mean free path for inelastic interaction, the damage is also reduced.

3.5.2 Scanning Electron Microscopy

The scanning electron microscope (SEM) used was a Philips FEI XL30 SIRIUS FEG. The specimens were fixed with conducting carbon cement (Leit-C by Göcke, BAL-TEC distribution) on aluminum sample holders and dried on air for 24 hours to guarantee an optimal contact between the sample and the sample holder. The SEM can be run under search mode (high resolution mode HR) or ultra-high resolution mode (UHR) [48].

3.5.3 X-ray diffraction

X-Ray diffraction was performed using a Philips PW 1800 X-Ray diffractometer operating at a current of 40 mA and a voltage of 40 kV, equipped with a fine-focused $\text{CuK}\alpha$ tube, $\lambda = 1.541828$ Å. Scanning steps were $0.02\ 2\theta$ and scanning rate was 1 step/s.

3.5.4 High temperature X-Ray diffraction

High temperature X-Ray diffraction was performed with a high temperature X-ray camera (model HTK 10, Anton PAAR) controlled by a temperature control unit (TCM 2000, Anton PAAR) mounted on a Philips PW 1830 diffractometer. Scanning steps were $0.02\ 2\theta$ and scanning rate was 1 step/s.

3.5.5 IR-spectrometry

IR-spectrometry was performed with a LECO infrared (IR) spectrometer, model RC-412 (St. Louis, MO, USA) allowing the monitoring of the water release as function of temperature. 0.2 g of the sample was placed on a sample holder which was inserted in a quartz combustion tube [49]. The sample was then heated up to 1200°C at a typical rate of $20^\circ\text{C}/\text{min}$, the final temperature was hold for several time periods (ranging from 1 min to 40 min) until the sample completely degased. The detector of the spectrometer is tuned to the principal absorption bands of water and CO_2 . The absorption is continuously monitored. Integrated over time the measured absorption can be used to calculate the amount of water or CO_2 released by the sample. In our case, the IR absorption curve allowed us to determine both structural (crystalline) water and adsorbed water of the sample depending on the degasing temperature (relative error for H_2O is 12 % and detection limit 0.1 wt%).

The experiments can be performed in a dynamically way, i.e. with a constant temperature gradient or in a static way i.e. at constant temperature.

Chapter 4

Chrysotile nanotubes

4.1 Introduction

Chrysotile is a natural mineral ($\text{Mg}_3\text{Si}_2\text{O}_5(\text{OH})_4$) with a nanotubular morphology and which belongs to the serpentine group (together with lizardite, antigorite and polygonal serpentine). In this chapter we will focus on the crystallographic structure of chrysotile nanotubes, their thermal stability and a potential application of chrysotile as template for the manufacturing of metallic nanowires. This latter aspect is described in more details in Chapter 5.

4.2 Crystallographic Structure

The general building blocks of the serpentine group minerals are tetrahedrally (T) and octahedrally coordinated (O) cation layers. In the case of the serpentine group the O layers have a structure close to that of brucite $\text{Mg}(\text{OH})_3$ and the T layers consist of Si atoms surrounded by 4 oxygen atoms, one oxygen atom per tetrahedron being attached to the octahedral layer. The sheets formed by O

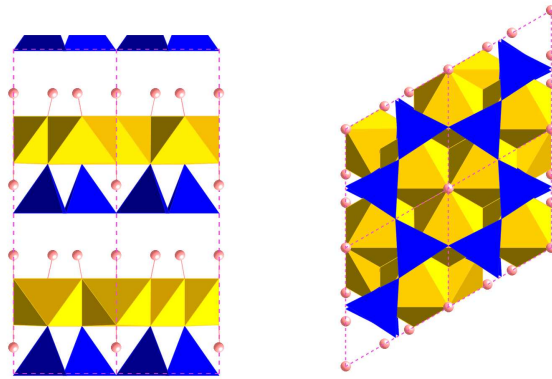


Figure 4.1: Left) Trigonal unit cell of lizardite seen along the $[010]$ axis. Right) seen along $[001]$.

and T layers are held together by Van der Waals bonds.

A lateral misfit between T and O layers has been postulated to explain the bending of the lizardite building layers of chrysotile [50] [51]. As a result of this bending, chrysotile minerals tend to form cylinders. In chrysotile, the T layer is the inner shelf and the Mg-O layer is stacked along the [001] direction (see fig. 4.1). The chrysotile crystallographic structure is monoclinic or orthorhombic. Two polytypes of chrysotile can be distinguished based on the orientation of the tube axis 1) normal chrysotile with the tube axis along the [100] direction and 2) parachrysotile with the tube axis along the [010] direction (see fig. 4.2).

Disregarding the curvature of the layers, monoclinic and orthorhombic chrysotile unit cells can be related to trigonal lizardite unit cells (a true polymorph of chrysotile, see fig. 4.1) [52] which allow the calculation of the crystallographic parameters of chrysotile (see fig. 4.2). The calculated values fit with the TEM observations of Yada and XRD determinations [53] [54]. Fig. 4.2 depicts important crystallographic features derived from the formalism developed here and compares these later with the measured crystallographic parameters.

Based on the above hypothesis and the good agreement with experimental results, "**normal**" **chrysotile** (clinochrysotile and orthochrysotile) can be modeled as formed by the rototranslation of a trigonal lizardite unit cell ($a = 5.3$, $c = 7.2$ [52]). For normal chrysotile, the rotation axis is parallel to the $[-110]$ axis of the trigonal unit cell and parallel to the [100] axis of the monoclinic chrysotile unit cell (see fig. 4.2). The translation is along the [010] direction of the trigonal unit cell. In order to get an inner tube radius of 2.5 nm (radius mostly observed for chrysotile), each cell is rotated relative to its neighbors by 17° around the tube axis. We obtain 21 lizardite unit cells for the first inner shell. The rototranslation of a single lizardite unit cell gives rise to a helix rolled around the tube axis.

The **parachrysotile** type has the fiber axis parallel to [010] axis [53] of the chrysotile orthorhombic unit cell. In a first approach, it can be modeled by a rotation of a lizardite unit cell around the trigonal [110] axis (corresponding to the [010] orthorhombic axis) and a translation along the trigonal [100] direction (rototranslation). In this case, each cell is rotated relative to its neighbors by 12° around the tube axis in order to get an inner tube radius of 2.5 nm. We obtain 30 lizardite unit cells wrapped around the tube axis for the first inner shell. The rototranslation also gives rise to a helicoidal structure rolled around the tube axis (see fig. 4.3). This type of chrysotile is only rarely encountered.

The (020) planes in HRTEM pictures will have different orientations relative to the tube axis in the different polytypes 1) parallel (normal chrysotile) 2) perpendicular (parachrysotile) and 3) oblique. The tilt angle of the (020) fringes ranges from 2 to 10° [53].

The rigid-body model and formalism proposed above is in good agreement with the general crystallographic features of chrysotile (see fig. 4.3) and is very similar to the formalism developed for carbon nanotube (see fig. 4.4). It however does not take into account the structural mismatch between T and O layers which is known to be the origin of layer curvature [55]. In fact, the chrysotile structure can not simply be represented by the rototranslation of a unit cell of the platy form of serpentine (lizardite), because it does not take into account the curvature of the unit cell with respect to the conventional crystal structures [56]. Therefore, a more precise description has been developed using cylindrical lattices (refer to the article of Devouard [50]).

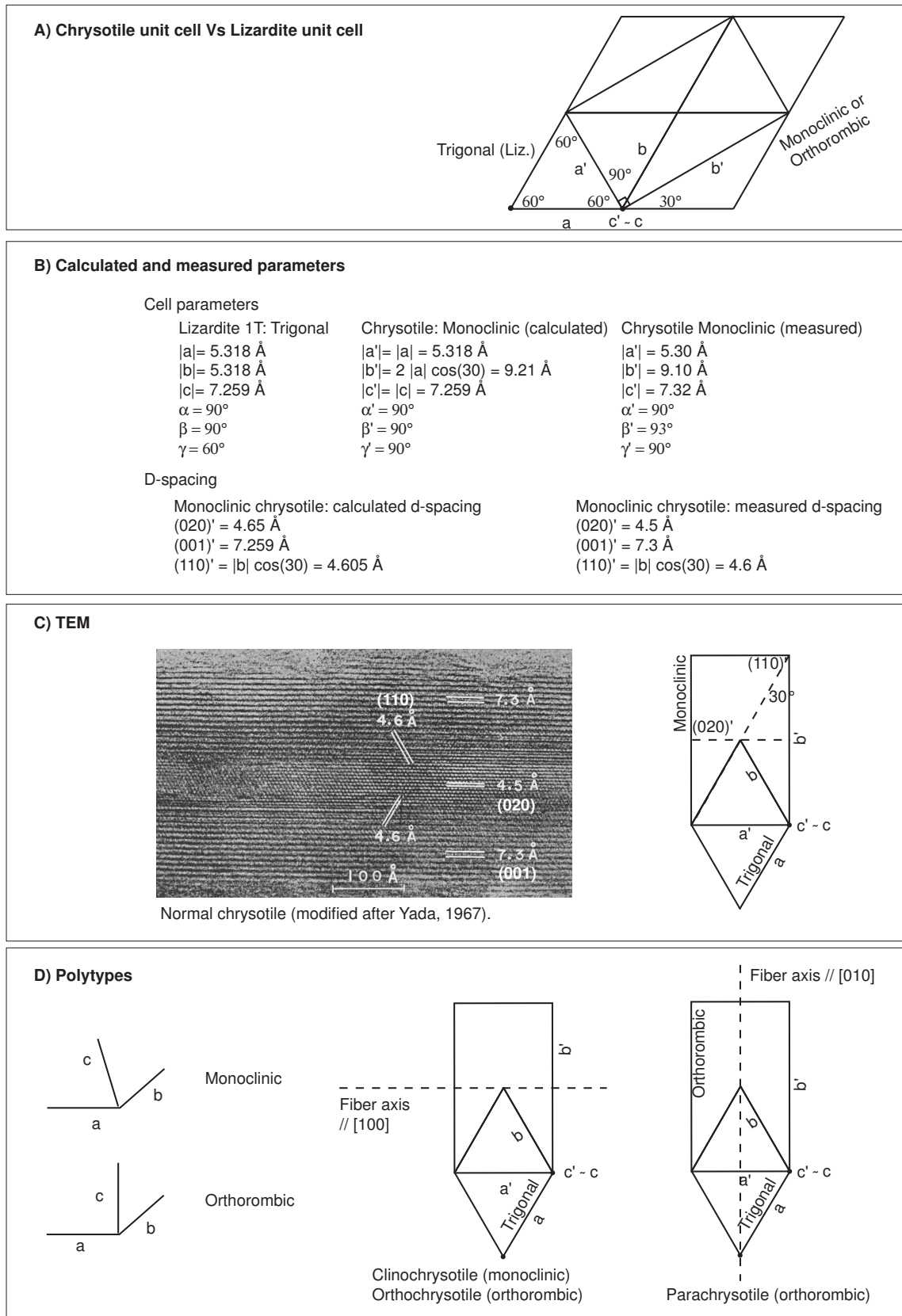


Figure 4.2: A) Relationship between the unit cells of trigonal lizardite, monoclinic and orthorhombic chrysotile. B) Comparison of calculated crystallographic parameters (from the above model) with measured parameters. C) Comparison with TEM picture. D) Definition of the two chrysotile polytypes.

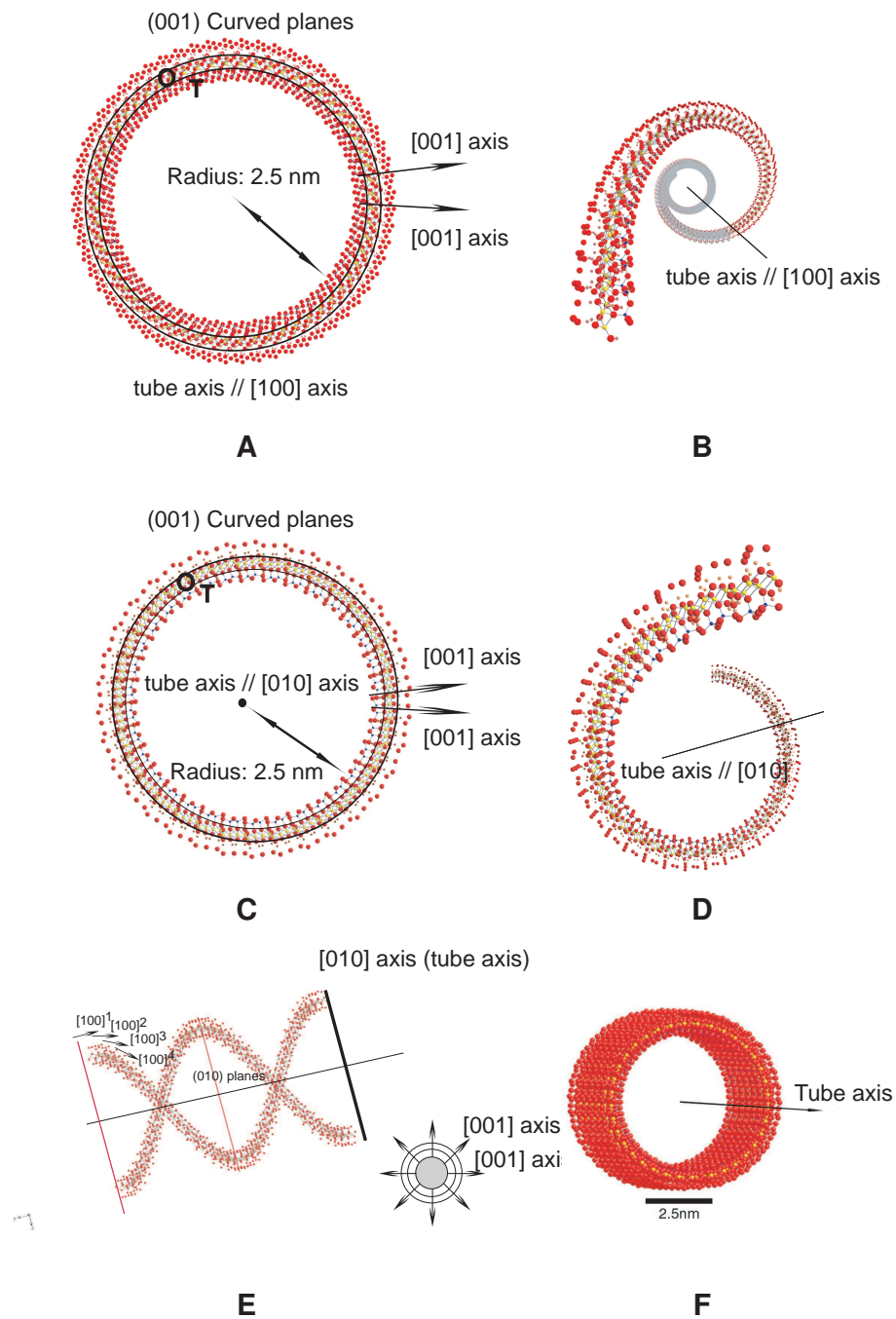


Figure 4.3: A) View parallel to the tube axis of a normal chrysotile polymorph. B) Perspective view of a single unit cell after applying the rototranslation operation. C and D) Computed simplified crystallographic structure of a parachrysotile polymorph. E) In parachrysotile the tube axis is parallel to the [010] direction. Two unit cells situated at opposite ends of the tube have been propagated by rototranslation, giving rise to a "double-chain" helicoidal structure. F) Computed crystallographic structure of a chrysotile nanotube (in this case parachrysotile).

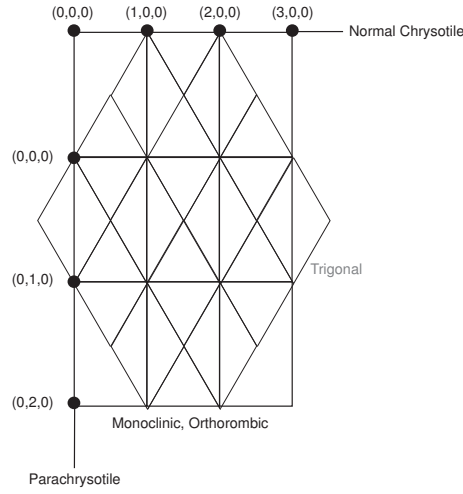


Figure 4.4: Left) Scheme that shows the folding procedure to create chrysotile nanotubes. This procedure is similar to the one used to create carbon nanotubes.

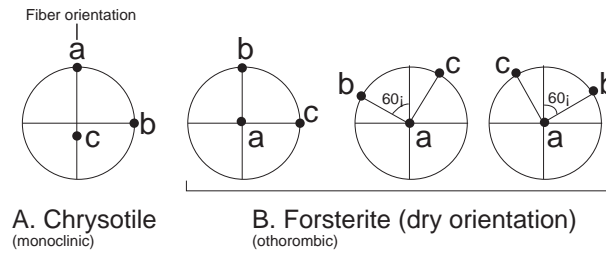


Figure 4.5: Topotactic relationship between normal chrysotile and forsterite formed by heating chrysotile in air and dry conditions (after M.C. Ball and H.F.W.Taylor [59]).

4.3 Thermal stability

The study of the thermal stability of chrysotile, will help us to constrain the temperature conditions for injection experiments in chrysotile nanotubes and to avoid a premature collapse of the template. When a fiber of chrysotile is heated in air the first products are water and a amorphous phase, which with time transform to forsterite (Mg_2SiO_4) [57] [58]. The forsterite has a topotactic relationship to the primary chrysotile, indicating that short range order survives the amorphous phase. Three crystallographic orientations of the new formed forsterite relative to the parent chrysotile have been observed (see fig. 4.5). In the presence of brucite, forsterite is also the breakdown product of chrysotile under hydrothermal conditions [59].

Different mechanisms have been proposed for this dehydroxylation reaction. It was first interpreted in terms of an **homogeneous process** by Brindley and Zussman who wrote the overall reaction as [58]:



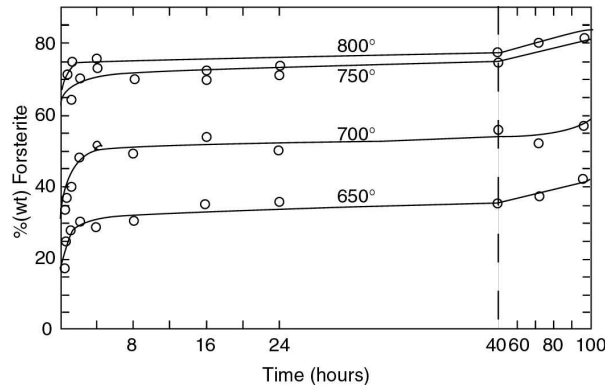
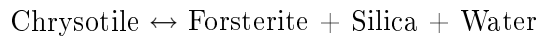
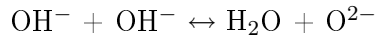


Figure 4.6: Weight percent of forsterite formed from powdered serpentine (modified after G.W. Brindley and R. Hayami [63]).



In this process, the dehydroxylation is supposed to occur uniformly throughout the crystal. The water is the result of the following net reaction:



The reaction proceeds most likely in two steps, i.e. a first hydroxyl group deprotonates and the resulting proton reacts with a second hydroxyl group to form water. Although this process may explain the topotactic relationship between chrysotile and forsterite, a homogeneous reaction with several reaction products is unlikely [60]. Moreover, this process does not take into account the observed amorphous phase observed before the formation of forsterite.

Ball and Taylor [61] and independently Brindley [62] suggested a heterogeneous reaction mechanism. These heterogeneous processes are maintained by appropriate diffusion of cations towards and away from a reaction front, in other words from "donor regions" to "acceptor regions".

The individual reaction steps are:

1. Formation of a "chrysotile anhydride". This is a partly disordered material giving an essentially amorphous X-ray powder diagram.
2. Cation reorganization takes place. Mg and Si cations begin to diffuse in opposite directions forming Mg rich and Si rich regions.
3. Formation of forsterite. Mg-rich regions change to forsterite (Mg_2SiO_4), involving an ordering of cations and changes in the oxygen packing. Stages (2) and (3) may be largely concurrent.
4. Formation of enstatite. At higher temperature in dry heating, the Si-rich regions change to enstatite MgSiO_3 .

G.W. Brindley and R. Hayami [63] studied the forsterite formation for serpentine heated during 20

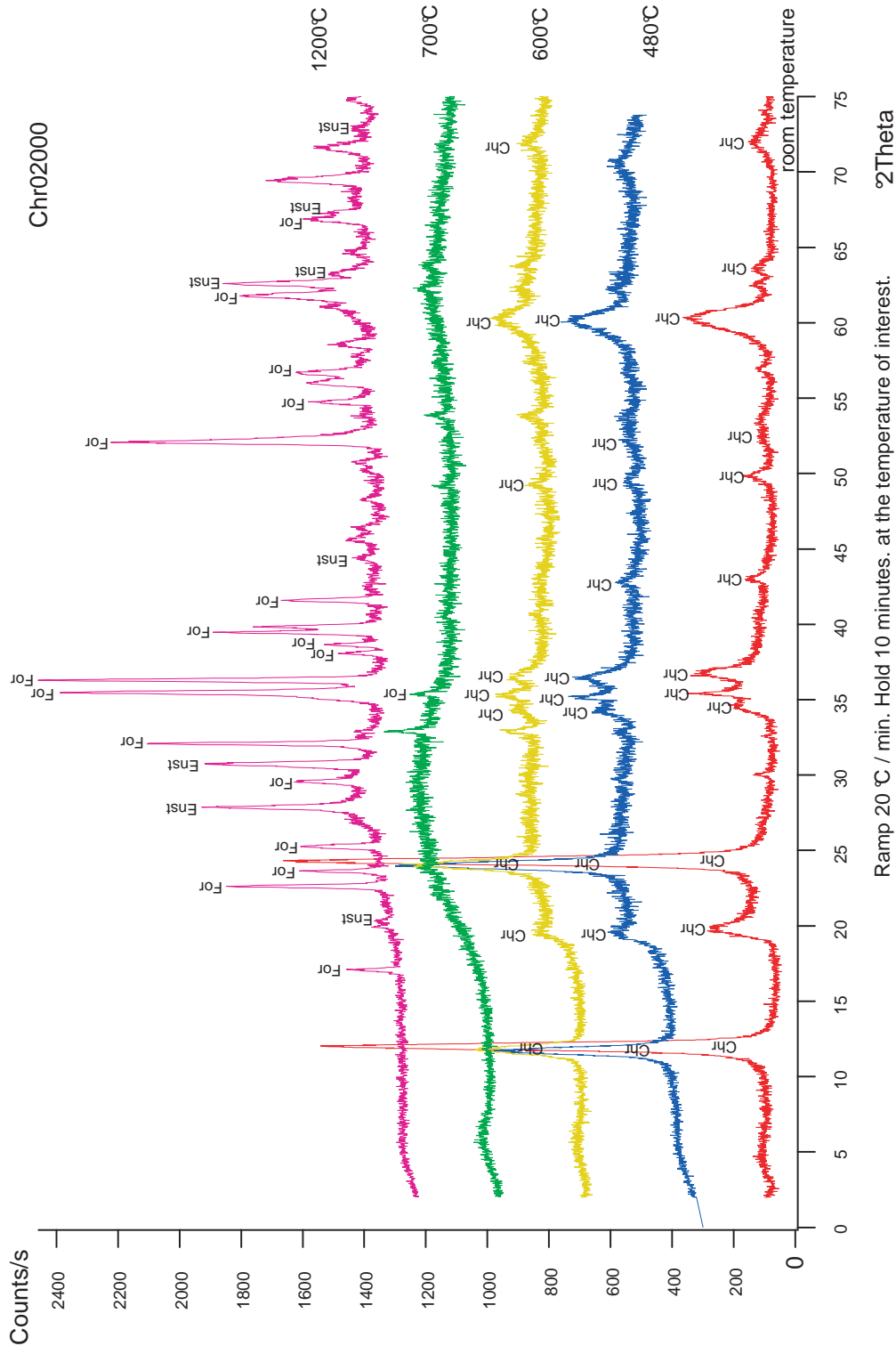


Figure 4.7: XRD analysis on chrysotile fibers. At 700°C chrysotile becomes amorphous. At 1200°C chrysotile is totally transformed to olivine and enstatite. Chr = chrysotile, For = forsterite, Enst = enstatite.

Table 4.1:

Sample	T	total weight loss	carbon loss	water loss
	°C	weight %	weight %	weight %
	TGA	TGA	IR	IR
Chr02000	450	7.63	1.49	6.14
Chr02000	500	8.76	1.26	7.50
Chr02000	550	15.07	1.36	13.71
Chr02000	600	15.37	1.59	13.78
Chr04000	450	6.39	0.91	5.48
Chr04000	500	9.18	0.91	8.27
Chr04000	550	15.30	1.26	14.04
Chr06000	450	7.94	0.32	7.62
Chr06000	500	12.09	0.32	11.77
Chr06000	550	16.13	0.53	15.6

hours at 570°C. From the weight loss compared with the maximal loss observed at higher temperatures, it was shown that the material was about 90% dehydroxylated by this treatment (see fig. 4.6). X-ray diffraction showed no residual reflections from non-reacted serpentine nor reflections of new-formed forsterite. Subsequent heat treatment were carried out in air for temperatures ranging from 650°C to 800°C for periods up to 100 hours. The results of the Brindley and Hayami experiments are shown in fig. 4.6. The amount of forsterite formed is expressed as a percentage of the final weight of the fired material. The maximum amount of forsterite is about 80% of the weight of the fully anhydrous material and is obtained after heating at 800°C for periods of 20 hours.

We studied the breakdown reaction of chrysotile at lower temperatures. In a series of heating experiments followed by XRD analysis of several chrysotile samples (see fig. 4.7 and appendix A), we confirmed 1) the formation of an amorphous material 2) the formation of forsterite and 3) the formation of enstatite. Chrysotile peaks disappear completely only for temperatures $> 650^\circ\text{C}$. The time at which forsterite appears decreases with increasing temperatures.

Table 4.1 shows thermo-gravimetric (TGA) analysis of three chrysotile samples annealed between 450°C and 600°C for 24 hours (heating rate was 20°C/min). IR data in table 4.1 were acquired for 10 min annealing time at the same temperature intervals. The data shows clearly that the dehydroxilation temperature is not the same throughout the nanotube wall. TEM observations of chrysotile annealed at lower temperature reveal that only the outer part of the tube wall is transformed. Heating to temperature over 550°C will dehydroxilate the entire tube. This dependence of the dehydroxilation temperature on radius is due to the continuous change of the structure with radius. After 24 hours at 600°C, the chrysotile sample Chr2000 lost a maximum amount of 15.37 weight %. Both TGA and IR data predict an amount of adsorbed water around 4-8 weight %. Figure 4.8 depicts the weight loss (as a percentage of the total) for three samples.

Temperature profiles of the dehydroxylation were obtained by dynamic IR-spectroscopy (see fig. 4.9 and appendix B). A first dewatering peak, visible on the left of fig. 4.9, is interpreted as the loss of physically adsorbed water from the chrysotile outer surface. A second peak is interpreted as desorption of the adsorbed water in the inner chrysotile tubes. None of these two peaks is followed by changes of the chrysotile structure (see fig. 4.7). The third peak is interpreted as dehydroxilation

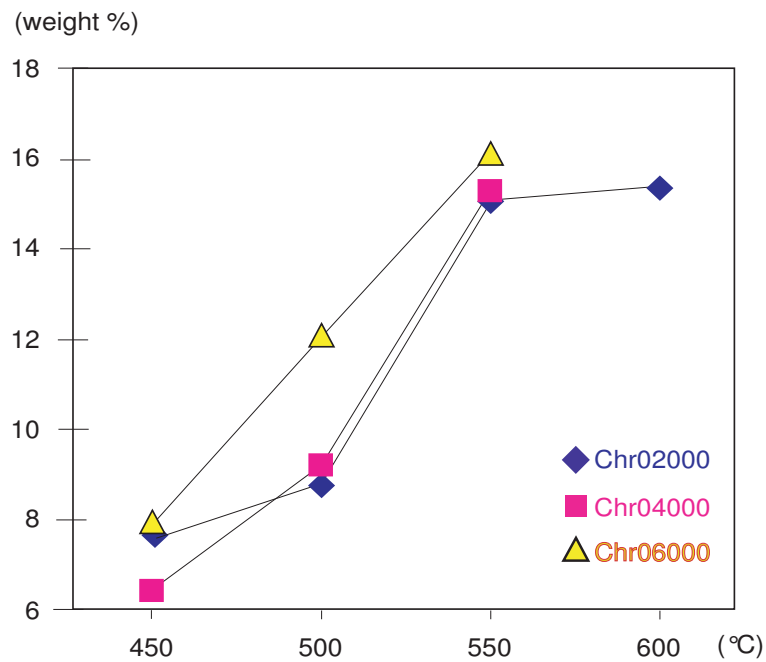


Figure 4.8: Maximum weight loss from thermogravimetric analysis (TGA) of three chrysotile samples annealed during 24 hours at constant temperature. Heating rate up to indicated temperature of 20°C/min.

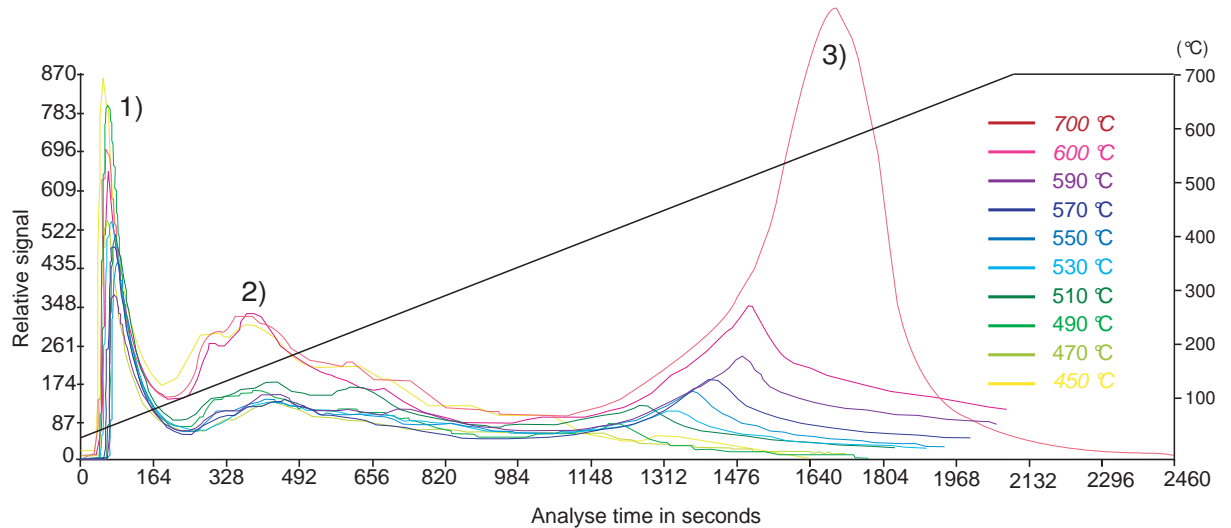


Figure 4.9: Dynamic IR-Analysis (Chr02000 chrysotile sample). The oblique black line in the middle of the graph represents the 20°C/min temperature ramp. Maintained at the indicated temperature during 10 min. The sample was maintained at the indicated temperature during 10 min.

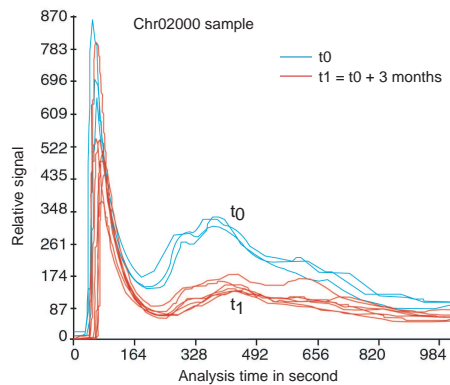


Figure 4.10: IR-Analyis: Chrysotile (Chr02000 sample). Ramp 20°C/min. Maintained at the indicated temperature during 10 min.

peak. First signs of dehydroxilation are seen at 490°C . The third peak reaches its maximum between 600°C and 700°C.

Figure 4.10 (detail of fig. 4.9) shows the IR-analysis of the same chrysotile sample once at time t_0 and after 3 months drying at 100°C (t_1). The two first dewatering peaks have been substantially lowered after 3 months drying. At higher temperature there is no more difference between the signal of the "wet" sample and the "dry" sample. This confirms the interpretation that the first two peaks represent the signal of adsorbed water and are not linked to dehydroxilation.

Figure 4.11 depicts the individual water loss profile for the chrysotile sample Chr02000 (see appendix A for more results) at 450, 600 and 700°C. The weight % of adsorbed water is about 4-7 % which confirms the above TGA analysis results. After annealing at 700°C for 10 min, the amount of structural water is 12.72 weight % which corresponds to the stoichiometric value of 12.99 weight % calculated from the formula $\text{Mg}_3\text{Si}_2\text{O}_5(\text{OH})_4$.

X-ray diffraction and TEM results suggest the following morphological and structural evolution of the tubes:

600°C: The chrysotile fibrils are still crystalline. Sporadically distorted areas can be seen. The degree of thermal reaction varies among the nanotubes during this early heating stage.

650°C: No change in the external morphology of the nanotubes can be detected, irregularly shape patch structures start to appear along the original nanotube length. This patches are crystalline, they present Bragg reflections in electron diffractograms. It was however impossible to index them. X-ray diffraction of the same material suggests that it is forsterite.

700°C: No change in the external morphology. Elongated patches cover much larger areas than before. Coalescence between fibril has started.

800°C: Individual fibers have collapse to single thicker fibers in which voids are present. Big patches are present; they are crystalline (forsterite).

900°C: Walls of original fibril unit have lost their straight profile and have a scalloped appearance.

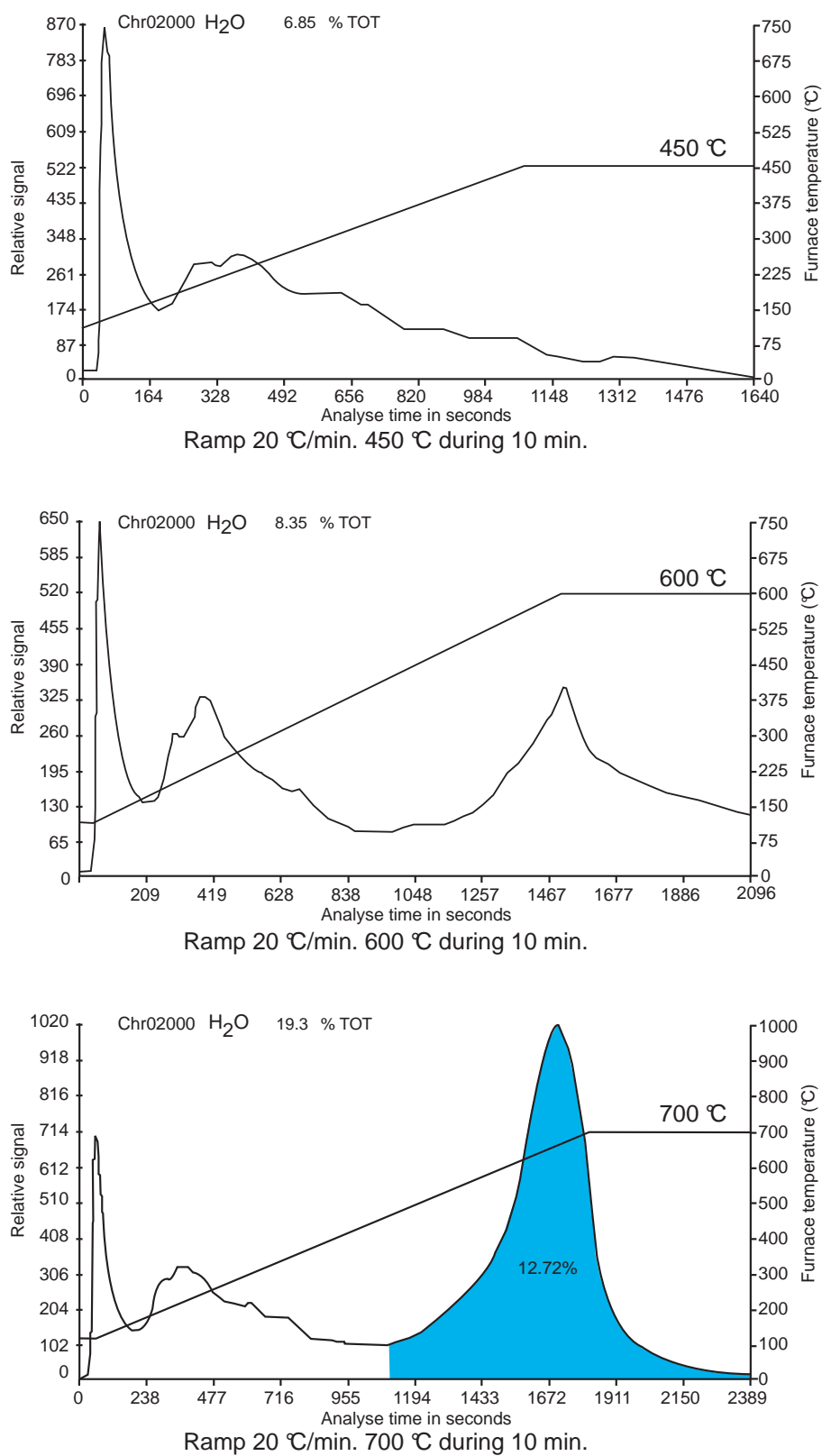


Figure 4.11: Dynamic IR absorption spectral analysis of the water loss of chrysotile sample Chr02000.

With the growth of forsterite grains, the patches have filled the original fibril.

1000°C-1300°C: The original fibril are completely changed into single twisted, ropelike fibers, consisting of a series of "knots" (no more canal) produced by 3D growth of the enstatite crystallites.

4.4 Pore structure

Analyzing the pore structure of chrysotile will allow us to better estimate the quantity of metal which has to be used for injection experiments. Chrysotile occurs as bundles, often concentrated in veins. The bundles are often hexagonally stacked which gives rise to a pore structure as depicted in fig. 4.12. According to the Pundsack nomenclature [64], two types of voids arise from such an hexagonal structure 1) type A voids (between tubes) and 2) type B voids (tube pores). The cross section A perpendicular to the fiber axis of such a unit cell is:

$$A = a^2/2 \tan(\pi/3)$$

A disk portion with inner pore is:

$$D = \pi r_{out}^2/6$$

The area of the type B pore is:

$$A_B = \pi r_{int}^2$$

The area of the type A pore is:

$$A_A = A - 6D - A_B$$

Considering a chrysotile nanotube with an outer radius of 15 nm and an inner radius of 2.5 nm, the type A voids represent 9.3 % of the volume and the type B voids represent 2.5 % of the volume of the entire stack. In this case, the total pore volume is 11.8 %. The void fraction of type A pores is dependent on the stacking geometry. The void fraction of type B voids is dependent on the tube inner radius. Calculations based on this simple model are in agreement with the experimental results obtained by Nauman et al. [65]. These results can be used in order to fill chrysotile nanotubes with metals, 12-15% volume of metal should be therefore sufficient.

4.5 Metal injection

The template method (top-down method) is one of the strategy used to produce nanowires [43]. The wire material is injected or deposited for example by electrodeposition into the prepatterned templates such as polymer channels, alumina membranes or zeolite channels. This method has been successfully used to manufacture ZnO nanowires [43]. ZnO was injected in an porous alumina (Al_2O_3) template [44]. Bi_2Te_3 nanowires with diameters of 200 nm and 40 nm have been produced by several template methods [66] [67] [68]. Bi_2Te_3 nanowires with diameters of 25, 50 and 75 nm have been produced by electrochemical deposition of a solution containing 0.075 M Bi and 0.1 M Te

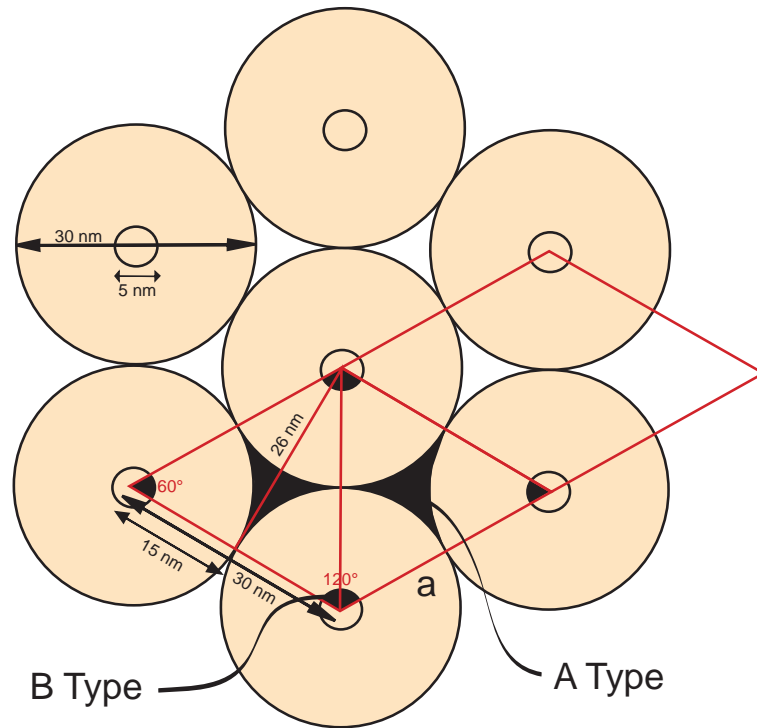


Figure 4.12: Pore structure (type A pore and type B pores) and unit cell.

in 1 M HNO₃ into porous alumina templates [69]. Chrysotile nanotubes have been used as templates for the manufacturing of Hg, Bi [70], Te [71] and Se [71] metallic nanowires. The injection under high pressure of molten metals using chrysotile as template requires a careful study of the stability of the mineral template for both temperature and pressure conditions. Chrysotile can be purchased at low costs; which makes them an attractive physical template.

For injection experiments, two physical properties of the wire material are of great importance 1) wetting behavior and 2) the melting temperature (and its variation with pressure). Wetting defines the degree by which a liquid covers a surface. In case of non-wetting the liquid deposited on the surface forms spherical droplets. Wetting fluids spread over the surface. The wetting behavior depends on surface tensions and the critical parameter is the contact angle, which is the angle between the solid and the liquid surface at the triple point i.e. where solid, liquid and gas meet. The surface tension is the excess free energy at equilibrium of a surface of phase A in contact with the phase B (considering isotropic surfaces). Three interfaces are distinguished 1) liquid-solid 2) liquid-vapor and 3) solid-vapor interfaces (see fig. 4.13). If the contact angle is lower than 90°, the liquid is described as 'wetting'. Angles between 90° and 180° are usually observed for liquids with higher surface tension than the underlying solid. The liquid is said to be 'non-wetting' (see fig. 4.13).

A droplet that is deposited on a solid surface will reach its final shape when the sum solid-vapor tension vector + the solid-liquid tension vector + the component of the liquid-vapor tension vector parallel to the solid (horizontal) surface equals 0.

Three physical parameters are important to calculate the pressure needed for injection experiments

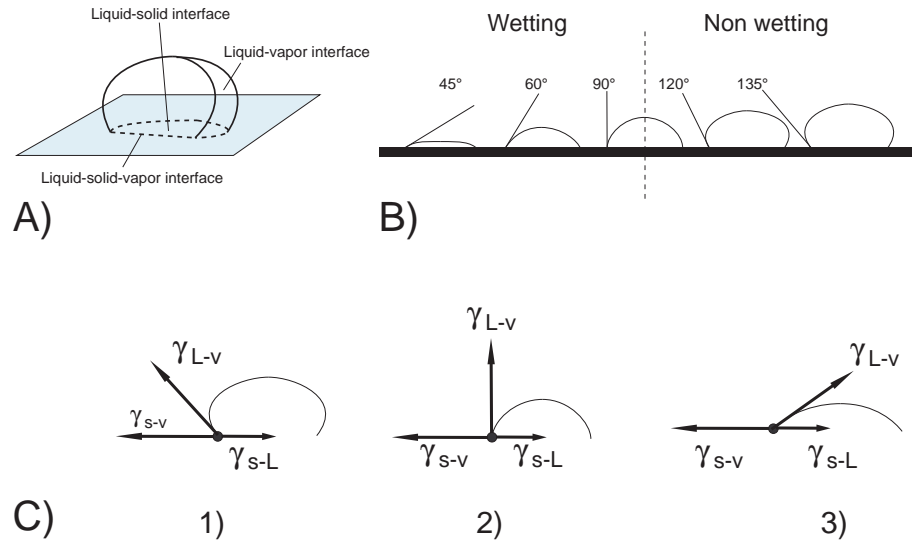


Figure 4.13: A) Cross-section of a drop of non-wetting liquid. B) Contact angle illustrated for wetting and non-wetting liquids. C) Time sequence of a droplet equilibrating on a solid surface. The contact angle is stable (3) when individual surface tension vector horizontal components are equilibrated.

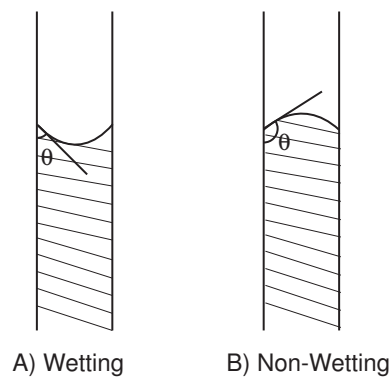


Figure 4.14: A) a wetting liquid in a capillary B) a non-wetting liquid in a capillary.

1) the liquid-vapor interfacial tension γ_{LV} , 2) the contact angle θ and 3) the geometry of the solid-liquid-vapor line [72]. Considering a non-wetting liquid injected in a capillary, the force tending to expel the liquid out of the capillary is related to the contact angle, the liquid-vapor surface tension and the radius of the capillary through:

$$F_{expel} = 2\pi r \gamma_{LV} \cos \theta \quad (4.1)$$

In order to maintain the non-wetting liquid in the capillary a opposite force is needed:

$$F_{opposite} = \pi r^2 P \quad (4.2)$$

At equilibrium:

$$-2\pi r \gamma_{LV} \cos \theta = \pi r^2 P \quad (4.3)$$

$$-D\pi \gamma_{LV} \cos \theta = \frac{D^2 \pi P}{4} \quad (4.4)$$

We can derive the pressure P needed to maintain the liquid in the capillary:

$$P = \frac{-4\gamma_{LV} \cos \theta}{D} \quad (4.5)$$

$$P = \frac{-2\gamma_{LV} \cos \theta}{r} \quad (4.6)$$

where $\cos \theta$ is:

$$\cos \theta = \frac{\gamma_{SV} - \gamma_{SL}}{\gamma_{LV}} \quad (4.7)$$

For a wetting liquid, the surface tension will lead to a convex curvature of the surface (see fig. 4.14). For non-wetting the surface tension will lead to a concave curvature of the surface. A non-wetting fluid already present in the capillary will be expelled.

4.5.1 Choosing the metals

For injection experiments of molten metals in chrysotile nanotubes, we assume the above set of equations valid for nanosized capillaries. In 1994, Dujardin et al. determined that the maximum γ_{LV} for a melt to fill carbon nanotubes through capillarity is 190 (mN/m) [73]. It means that no

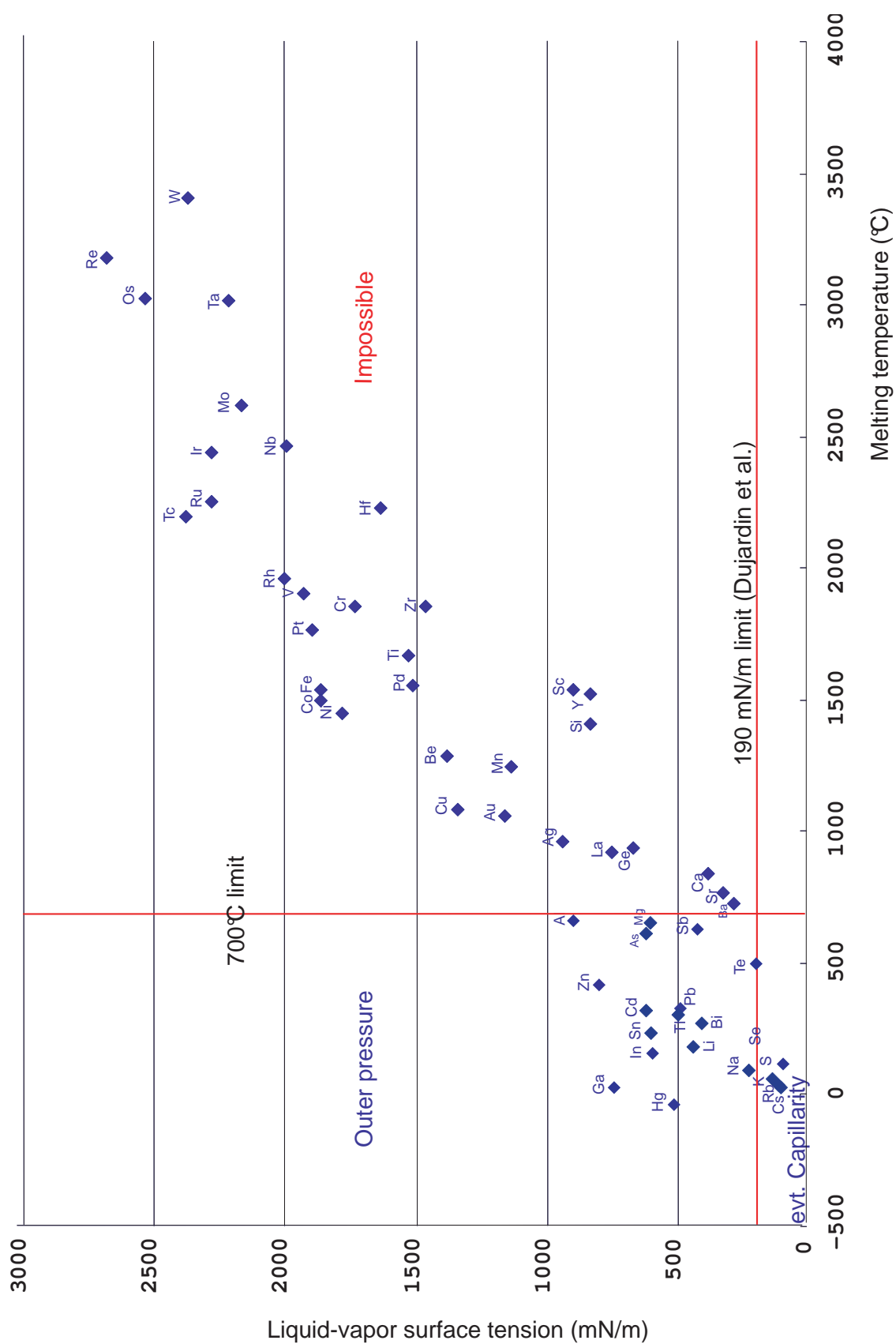


Figure 4.15: Metals are plotted against their melting temperature and their liquid-vapor surface tension. Metals with a melting temperature above 700°C cannot be considered for injection experiments. Metals with surface < 190 mN/m could probably be injected through capillarity.

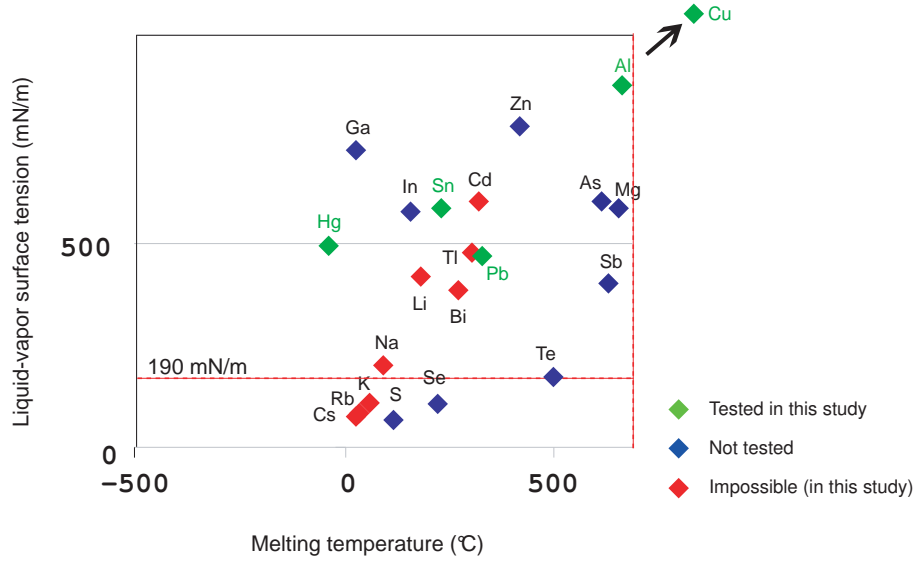


Figure 4.16: Metals that may be used for filling experiments are plotted against their melting temperature and their liquid-vapor surface tension. Green dots correspond to metals tested in this study. Red dots correspond to metals too dangerous for high-pressure experiments and blue dots metals were not considered.

external pressure is needed to inject a melt with γ_{LV} lower than this value.

We decided to limit the experiment to elemental phases. It is difficult to estimate if pressure is needed or not, because the surface energy of the cavity surface is not known. The structure is similar to bent 2:1 phyllosilicate surface such as talc. Talc has a surface energy around 200 mJ/m^2 i.e. 4 times larger than graphite [74]. If the γ_{SL} values for the system chrysotile cavity surface-metal melt are smaller than the corresponding value for carbon nanotubes inner surface-metal melt then the limiting value of γ_{LV} for which the liquid enters the tube by capillary action increases. For larger γ_{SL} values the limiting γ_{LV} value for the chrysotile nanotube system remains higher up to a difference $\gamma_{SL}^{\text{chrysotile}} - \gamma_{SL}^{CN} = 160 \text{ mJ/m}^2$. As the latter value is relatively large it can be expected overall, that for a non-wetting metal melt less pressure is needed to fill chrysotile tube compared to CN's. Figure 4.15 depicts which elements may be used to fill chrysotile nanotubes and if an external pressure is needed or not. Materials with melting temperatures above 700°C have to be excluded because of the thermal stability of chrysotile (see section 4.3). Materials with melting temperature under 700°C can be considered for capillary filling and/or injection experiments under pressure. Alkali metals have been excluded because of their dangerousness. Figure 4.16 is a detail of figure 4.15 and shows metals with melting points under 700°C that can therefore be considered for injection experiments under external pressure conditions.

Based on the above criterions, the following metals have been tested: **Hg, Pb, Sn, Al and Cu**. As expected, the filling experiments for Al and Cu were unsuccessful because of the thermal stability of chrysotile (see section 4.3). The results of successful filling experiments are presented in chapter 5. The pressures needed assuming a wetting angle of 180° to inject different molten materials are depicted in fig. 4.17. Calculations are based on equation 4.6 for a capillary with a radius of 2.5 nm . The calculated pressures obtained from a wetting angle of 180° are maximal pressures. For angle

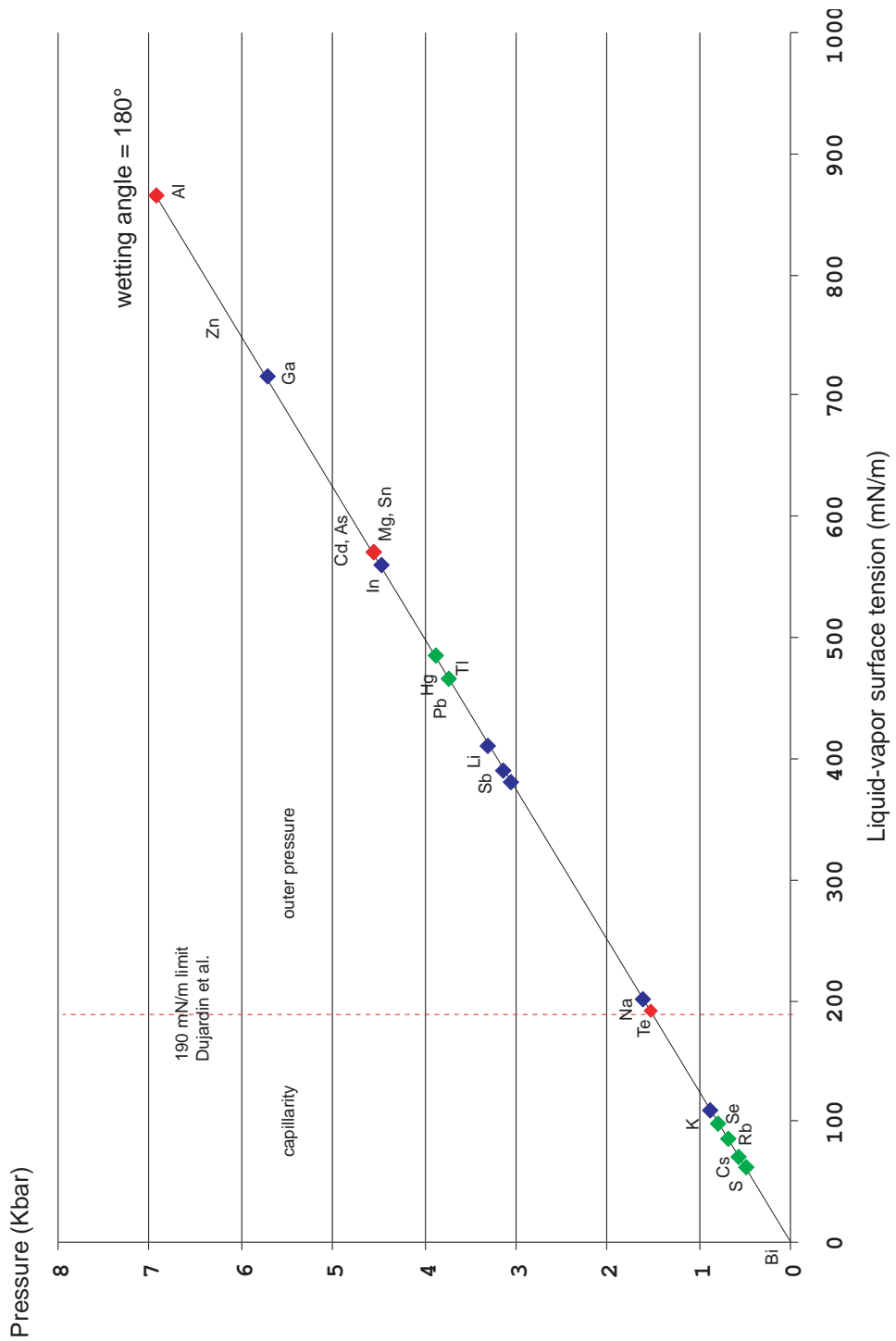


Figure 4.17: Pressure needed to injected molten elements in a capillary with 2.5 nm radius assuming a contact angle of 180°. S, Cs, Rb, Se, K and Te can eventually be filled through capillary action.

Table 4.2:

Metal	ρ_0 (g/cm ³)	K Bulk modulus (mbar)	$K' = \frac{dK}{dP}$	γ Slater Gruneisen parameter
Hg	13.53	0.25	8.70	4.18
Pb	11.30	0.46	7.94	3.80
Sn	7.26	0.58	4.40	2.03
Al	2.70	0.76	4.00	1.83
Cu	8.96	1.40	5.59	2.63

Metal	$\alpha_V(T)$ (10 ⁻⁶ K ⁻¹)	ρ_P (g/cm ³) at 1 bar and 25°C	ρ_P (g/cm ³) at 1 Kbar and 25 °C	ρ_{PT} (g/cm ³) at 1Kbar and 100°C
Hg	23.10	13.53	13.58	13.56
Pb	28.90	11.30	11.32	11.30
Sn	22.00	7.26	7.27	7.26
Al	23.10	2.70	2.70	2.69
Cu	16.50	8.96	8.97	8.95

less than 180°, the pressure may be lower. A maximum pressure of 10 Kbar was calculated for Cu. S, Cs, Rb, Se, K and Te can eventually be filled through capillary action.

The melting temperatures shown in fig. 4.15 are for ambient pressure. The melting temperature increases with increasing pressure. A simple model for the pressure dependency of the melting temperature has been developed by Saxena et al. [75]:

$$T_m = T_{mo} \exp(2\gamma_0(1 - \frac{\rho_0}{\rho}) + \frac{2}{3} \ln(\frac{\rho_0}{\rho_P})) \quad (4.8)$$

T_m and T_{mo} are the melting temperature at high pressure and at 1 atm, ρ and ρ_0 are the densities at pressure P and at 1 atm. γ is an input parameter called the Slater Gruneisen parameter which depends on the isothermal bulk modulus K ($\gamma = \frac{1}{2}(K - \frac{1}{3})$) [75]. The metal density as function of pressure and temperature can be derived from the Murnaghan state equation and assuming ($\gamma_0\rho_0 = \gamma\rho$) [76]:

$$\rho = \rho_o(1 + \frac{K'}{K}(P - P_o))^{\frac{1}{K'}}(1 - \alpha_{av}(T - T_o)) \quad (4.9)$$

K' is the pressure derivative of the bulk modulus $\frac{dK}{dP}$ and $\alpha_{av}(T)$ is the average value of the thermal expansion coefficient $\alpha_V(T)$. The parameters used for density calculations at pressures between 1 bar and 10 Kbar ([77] [78] [79] [80] [81]) are listed in table 4.2 and the the resulting T_m are depicted in fig. 4.18. The melting temperatures increase +- linearly with pressure. This effect has no consequences for Mg, Pb and Sn because the melting temperatures at injection pressure remain well below the breakdown temperature of chrysotile. For aluminum the situation is critical, because the melting temperature at injection pressure is very close to the breakdown temperature (see fig. 4.19).

Viscosity plays also a role in the filling of nanoscale templates with molten metals (see fig. 4.20).

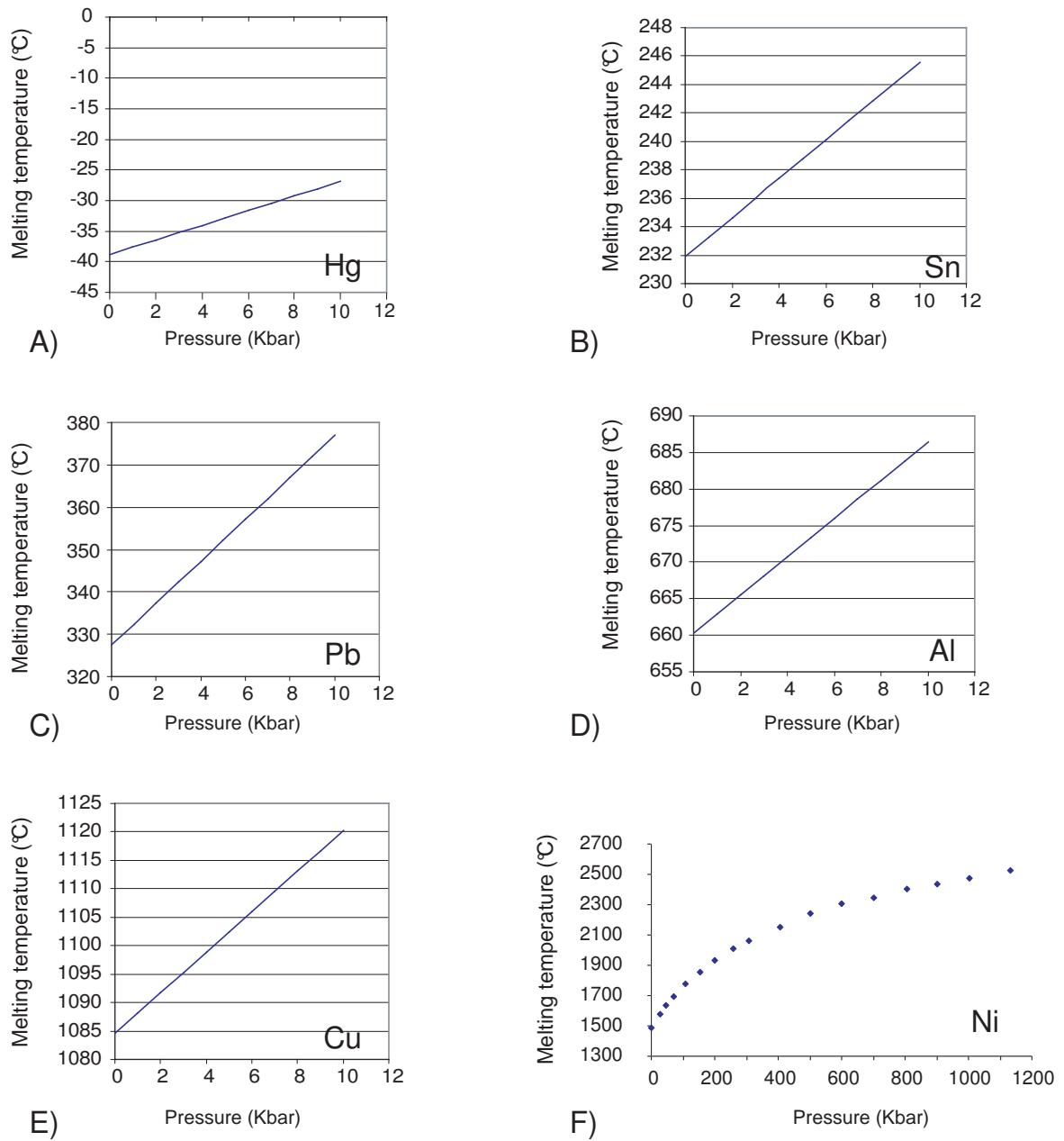


Figure 4.18: Computed variation of the melting temperature as function of pressure for A) Hg B) Sn C) Pb D) Al E) Cu and F) Ni. Ni has been plotted to observe the evolution of melting temperatures at pressures well above experimental conditions (max 10 Kbar).

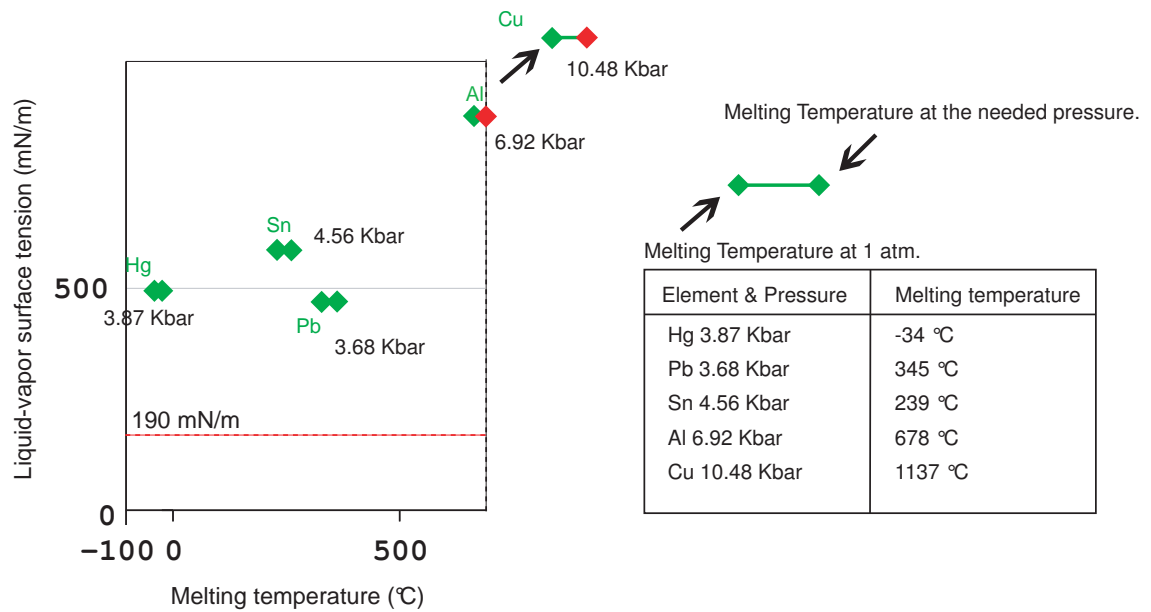


Figure 4.19: Melting temperature of metals plotted Vs liquid-vapor surface tension. The influence of applied pressure on the melting temperature is represented. Aluminum is critical element for injection experiments. Copper should not be successfully injected.

Therefore sufficiently long pressure experiments had to be performed to allow a good injection of the metals. High pressure experiments for Hg and for other metals injection are described in section 3.4.2 and results in chapter 5. High pressure experiments for other metals are described in section 3.4.1 and results in chapter 5.

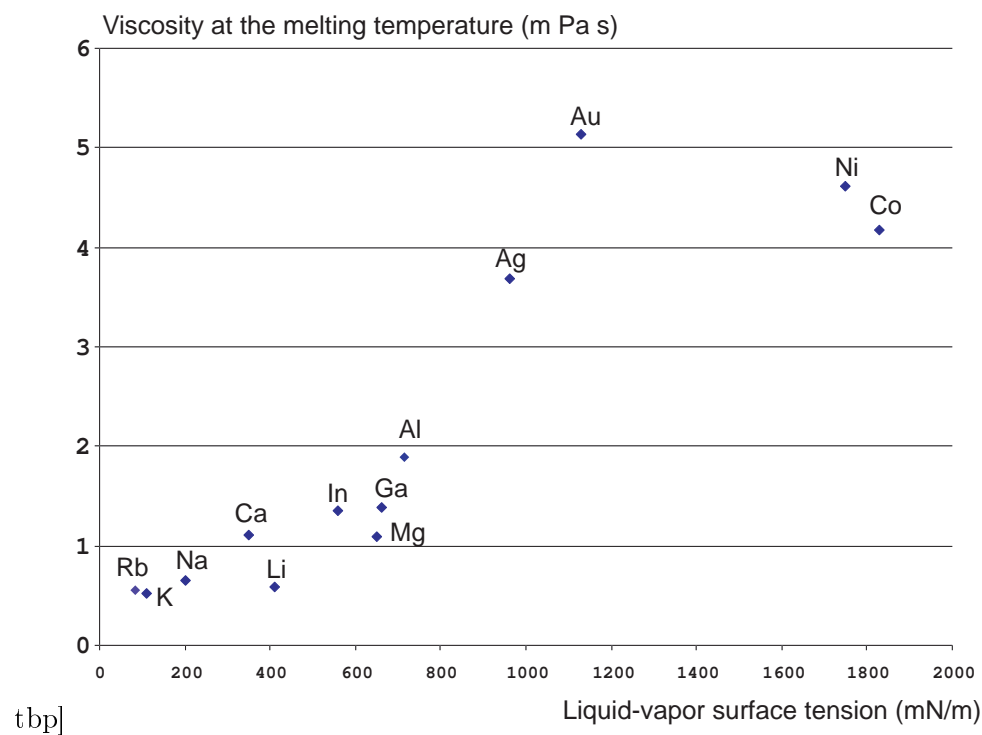


Figure 4.20: Viscosity versus surface tension for metals (After the Handbook of Chemistry and Physics, 1995-1996, 6-220 to 6-221).

Chapter 5

Filling of chrysotile nanotubes with metals

Article published in the **Journal of Material Research**

Vol.17, No. 5 p. 112 May 2002

C. Métraux, B. Grobéty, P. Ulmer

C. Métraux, B. Grobéty, University of Fribourg, Institute of Mineralogy and Petrography, 1700 Fribourg, Switzerland. P. Ulmer ETH Zürich, Institute of Mineralogy and Petrography, 8052 Zürich, Switzerland

Nanowires were produced by injection of molten Hg and Pb into chrysotile nanotubes. The breakdown of chrysotile and the surface tension of the molten metals are the limiting factors for the filling procedure. The thermal stability of chrysotile nanotubes has been investigated by IR-spectrometry, DTA-TGA, and XRD analyses. For short-term thermal annealing (30 minutes) the tube morphology remains stable up to 700°C. The high surface tension of both molten Pb and Hg ($\gamma_{LV} > 200$ mN/m) requires external pressure in order for the melts to penetrate into the tubes. Filling of the tubes was achieved under high pressure and high temperature conditions compatible with the stability range for chrysotile determined in the annealing experiments. TEM observations confirmed high filling yields for both metals. Almost all nanotubes have been partially filled with lead. The length of continuous wires ranged from tens to hundreds of nanometers. Additional experiments with tin were not successful.

5.1 I. INTRODUCTION

The potential of nano-sized, tube-shaped components range from the use as wires, wire-templates, microreactors, hydraulic tubes to gas storage devices among others. The most promising contender for such applications are synthetic carbon nanotubes. Other layered materials that are known to form nanotubes are boron nitride¹, molybdenum disulfide² and tungsten disulfide². A naturally occurring, nano-sized, tube-shaped phase is the silicate mineral chrysotile, $\text{Mg}_3\text{Si}_2\text{O}_5(\text{OH})_4$, which may represent an alternative to carbon nanotubes for certain applications such as manufacturing of nanowires. The structure of chrysotile³ consists of wrapped sheets composed of a layer of tetrahedrally coordinated silicon cations and a layer of octahedrally coordinated magnesium cations, which can be substituted by aluminum and iron. Aluminum can also be present in the tetrahedral sheet instead of silicon (Tschermak's substitution). Chrysotile is common in hydrothermally altered ultramafic rocks and easy to extract in large quantities. The tubes have an outer diameter ranging from 10 to 50 nm and an inner diameter between 1 and 10 nm. The tube walls are always multilayered.⁴ Like for carbon nanotubes, different wrapping schemes are known.⁵ The most frequent polytypes are normal chrysotile with a fiber axis perpendicular to the [010] direction and parachrysotile with a fiber axis in the [010] direction.⁵ Cylindrical, spiral and multilayer wrapping is found for both chrysotile polytypes.⁵ The chrysotile nanotubes differ from the carbon nanotubes in some important physical parameters e.g. they are non-conducting, they have lower mechanical strength, their length can reach the mm-range and they are always uncapped.⁶ Some potential applications of nanotubes such as the manufacturing of nanowires require access to the inner cavity.⁷ Carbon nanotubes have been filled by wet chemistry using capillary suction.^{8–12} Chrysotile nanotubes have been filled with metals melting at low temperature such as Hg,^{13–14} Bi,¹⁴ Te,¹⁵ Se¹⁵ and with semi-conductor materials using both high pressure techniques and CVD^{14–18}, but only few experimental details were given. The limited temperature stability of the chrysotile morphology and its possible influence on the filling process was not addressed. The structural breakdown of chrysotile e.g. the transformation of the walls has been addressed by many authors, but not in relationship with the filling of the nanotubes.^{19–22} The phase evolution during heating is well documented, but information on the morphological changes are scarce.²³ This paper presents not only the structural but also morphological evolution of chrysotile nanotubes during short term, high temperature annealing. This information was used to design the high temperature injection experiments with Pb and Sn. In the liquid state these metals have surface tensions, which do not allow filling by capillary suction. An outer pressure must, therefore, be applied to force the melts into the nanotubes.⁹ As pressurizing device an end-loaded piston cylinder apparatus was used for the first time. These experiments are the first attempts to fill chrysotile tubes close to the beginning of dehydration and the metals used have higher melting temperatures than all materials that were used in previous experiments.^{13–18}

5.2 II. EXPERIMENTAL

5.2.1 A. Starting materials

All experiments were performed with the same chrysotile specimen from an unspecified location in Pennsylvania (USA). High purity metal liquid and powders were used for the filling experiments: Hg (Micromeritics, USA), Pb (Riedel-de Haën, Germany), and Sn (Fluka, Switzerland).

5.2.2 B. Thermal analysis of chrysotile nanotubes

The water release of the chrysotile sample as function of heating temperature was monitored with a LECO IR-spectrometer, model RC-412. The IR absorption of the gas was measured continuously and quantitatively for absorption bands characteristic for H₂O and CO₂. The onset of dehydration was determined by heating the samples (0.2g) from 100°C to 700°C at a rate of 20°C min. To quantify the wt% of water lost by dehydroxylation at a fixed temperature, sample were first annealed at 450°C during 30 min to eliminate adsorbed water and then heated to the temperature of interest. The water release was monitored for 30 min. The in-situ IR analyses were complemented by DTA-TGA analysis. Measurements from room temperature to 1100°C were performed using a Mettler-Toledo model TGA/SDTA.851 at a heating rate of 10°C/min. XRD patterns were taken on sample powders using a PW1800 Philips system equipped with a Cu K X-ray tube, a graphite monochromator and a variable receiving slit. The data were collected in step scanning mode from 5° to 75° (2 θ), with a step size of 0.02° (2 θ) and a counting rate of 2 s/step.

5.2.3 C. Filling experiments with Hg

Chrysotile nanotubes were placed in a Micromeritics model Autopore II 9220 Hg-porosimeter. The sample holder containing the nanotubes was evacuated at 50 mHg then Hg was injected. The pressure necessary to fill capillaries by fluids is given by the Young-Laplace equation:

$$\Delta p = \frac{2\gamma \cos \theta}{r} \quad (5.1)$$

where γ and θ are the liquid-vapor surface tension and the wetting angle of the liquid respectively, and r is the radius of the capillary. The minimum pressure to fill a nanocapillary with a diameter of 5 nm (typical inner diameter of chrysotile nanotubes) with Hg is 2.43 Kbar. This value is obtained for a constant contact angle of 130° and for a surface tension (against vacuum) of 473 mN/m at 25°C (γ_{LV} at the melting temperature of Hg: 484 mN/m, $-d\gamma^{LV}/dT$: 0.18 mN/mK).²⁴ The sign of the pressure derivative of the surface tension is very much dependent on the vapor phase with which the liquid is in contact.²⁵ For an inert gas $d\gamma^{LV}/dP$ is positive, but experiments have shown that with exception of helium most other gases adsorb onto the liquid surface and the pressure derivative becomes negative,²⁶ which is probably also the case for the gas (air, water vapor) surrounding chrysotile tubes in the container. The pressure of 4 Kbar used in the experiments should, therefore, be sufficient to fill all tubes down to the smallest diameters. The pressure was increased in variable steps. As soon as 4 Kbar was reached, the pressure was immediately released to atmospheric conditions. Finally, the chrysotile nanotubes were extracted from the sample holder, mechanically ground, placed in ethanol and ultrasonically dispersed.

5.2.4 D. Filling experiments with Pb and Sn

The metals lead and tin have melting temperatures, which, at ambient pressure, are below the breakdown temperature of the tube morphology of chrysotile. The surface tensions of the two metals

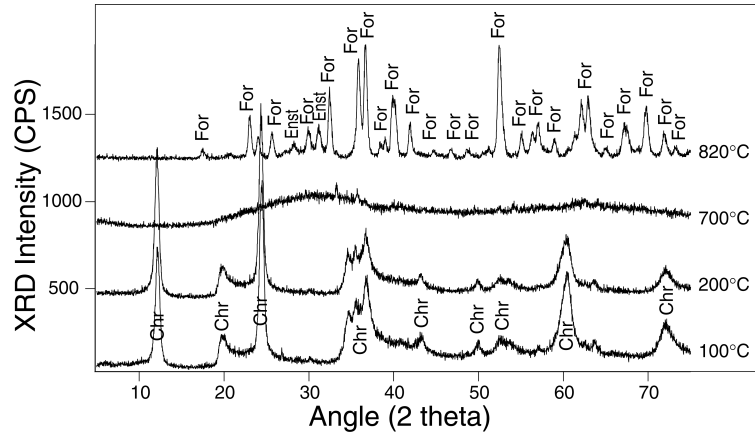


Figure 5.1: XRD patterns of chrysotile nanotubes after annealing for 10 min in dry air.

at melting temperature are similar to the surface tension of mercury e.g. 460 mN/m at 327.4°C for lead and 570 mN/m at 231.9°C for tin.²⁴ Assuming the worst case for the wetting angle, e.g. 180°, the minimum filling pressures at the melting temperature are 3.68 Kbar for Pb and 4.56 Kbar for Sn. The experiments were performed in a Johannes type piston-cylinder pressure apparatus at a pressure of 10 Kbar and a temperature of 440°C, well above the calculated minimum pressures and below the onset temperature of dehydroxilation of chrysotile (s. Results). The experimental temperatures above the melting point were chosen, because pressure is known to rise the melting temperature of metals.²⁷ The true minimum filling pressure is probably lower than the values indicated above, because the temperature dependence of the surface tension is negative for both metals (Pb: -0.11 mN/mK, Sn: -0.10 mN/mK)²⁴ and also the pressure derivatives of the surface tension are most likely negative.²⁶

The chrysotile nanotubes and pure metal powder (Pb, Sn) were mechanically ground together and put in a BN capsule, which was placed inside a Pt capsule (3 mm in diameter, 10 mm long). The material was first pressurized, then heated to 440°C and annealed during 15 min. The mixture was subsequently quenched to room temperature to freeze the metal within the nanotubes. The quenching is in the order of 200°C per second down to 200°C and then slower to room temperature. Finally pressure was lowered to atmospheric conditions. Nanotubes were extracted from the BN/Pt capsules, mechanically ground, placed in ethanol and ultrasonically dispersed.

5.2.5 E. Transmission Electron Microscopy

A drop of the ethanol dispersion with the run products was put on a holey carbon grid and dried in air. TEM studies were performed using a Philips CM10 and a Philips CM200 operated at 100 and 200 kV respectively. The mercury filled samples were analyzed at 100 kV, all other samples at 200 kV. The radiation damage in chrysotile is probably due to radiolytic processes. The loss of hydrogen through a knock-on process destabilizes the structure, which transforms to an amorphous phase. Heating of the sample has only a secondary influence. The increase in acceleration voltage reduces this effect and allowed HRTEM imaging of the lead and tin samples. Under illumination conditions necessary for high-resolution imaging, chrysotile survives for approximately 30 seconds.

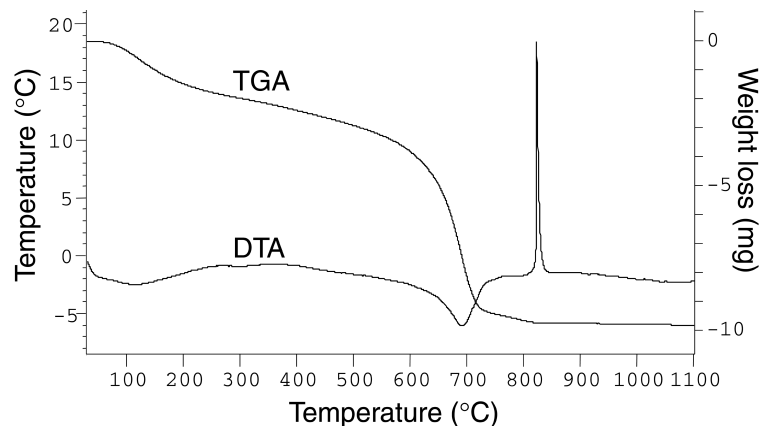


Figure 5.2: TG-DTA curves of chrysotile nanotubes.

5.3 III. RESULTS AND DISCUSSION

5.3.1 A. Thermal properties of chrysotile nanotubes

XRD patterns (Fig. 5.1) of the Pennsylvanian sample are compatible with the normal chrysotile polytype. Two transformations can be distinguished in DTA runs up to 1100°C of these nanotubes (Fig. 5.2). A broad endothermic peak, centered at a temperature of 700°C, is attributed to the departure of structural water leading to an amorphization of the material. The amorphous nature of the initial breakdown product is confirmed by the XRD pattern of a sample quenched from the same temperature (s. Fig. 5.1). The second, sharp exothermic DTA peak at about 820°C is attributed to the crystallization of the Mg-silicate phases forsterite Mg_2SiO_4 and enstatite MgSiO_3 as inferred from XRD patterns of quenched samples (s. Fig. 5.1). The total weight loss measured by TGA is 15.2 wt%, which is about 2.5 wt% above the water quantity expected from the hydroxyl concentration in stoichiometric chrysotile.

The continuous in-situ IR scans on as received chrysotile show three peaks. The first two peaks at about 100°C and 200°C of the dehydroxilation curve (Fig. 5.3) are attributed to water desorbed from the surface of the chrysotile nanotubes and/or released from the interior of the tubes, since no structural changes were detected by XRD analysis on fibers treated at the same temperatures (s. Fig. 5.1). The onset of the third, broad dehydroxilation peak is around 470°C. This peak is linked to a loss of crystallinity indicated by a net decrease of the maximum intensity and a broadening of XRD peaks (Fig. 5.4).

Samples of chrysotile first annealed at 450°C for 30 min to eliminate adsorbed water and then heated at the temperature of interest and annealed for an additional 30 min show that for temperatures < 650°C dewatering is not going to completion. The total amount of water, lost during these additional 30 min of thermal treatment, increases with annealing temperature (Fig. 5.5). The water loss after 30 min at 550°C corresponds only to 33 % of the stoichiometric hydroxyl content, whereas at 600°C it corresponds to 79%.

The XRD patterns (s. Fig. 5.1) of samples annealed at 700°C are characteristic for amorphous

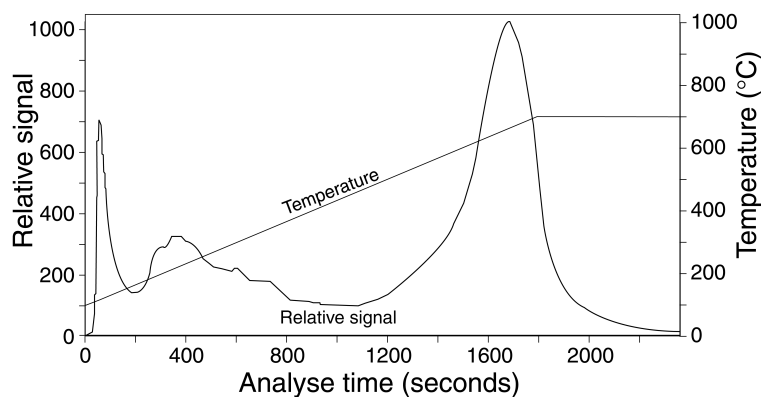


Figure 5.3: Water release of chrysotile nanotubes as function of temperature measured through continuous in-situ IR of the released gases.

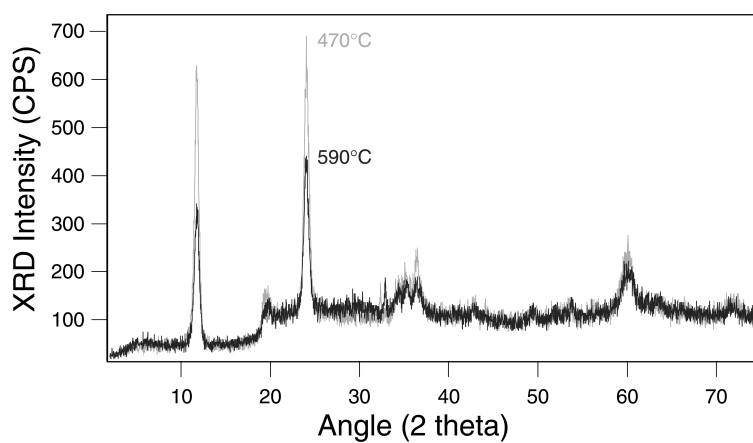


Figure 5.4: XRD patterns of chrysotile nanotubes after annealing for 10 min at 470 and 590°C in dry air.

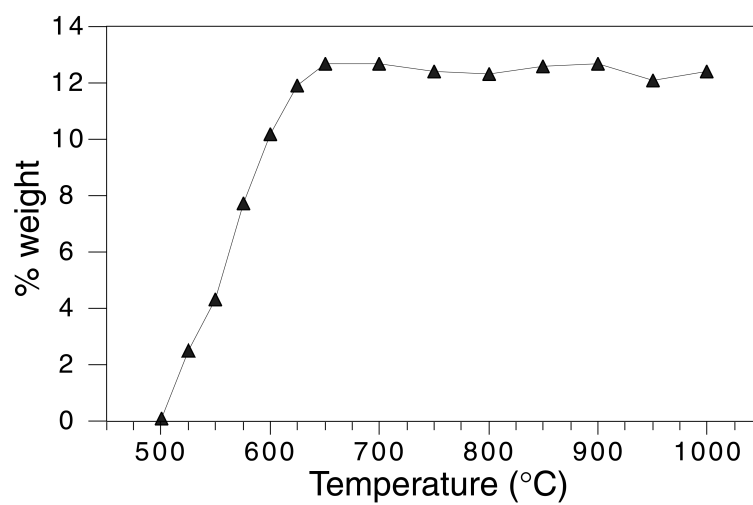


Figure 5.5: Amount of water released as function of the annealing temperature.

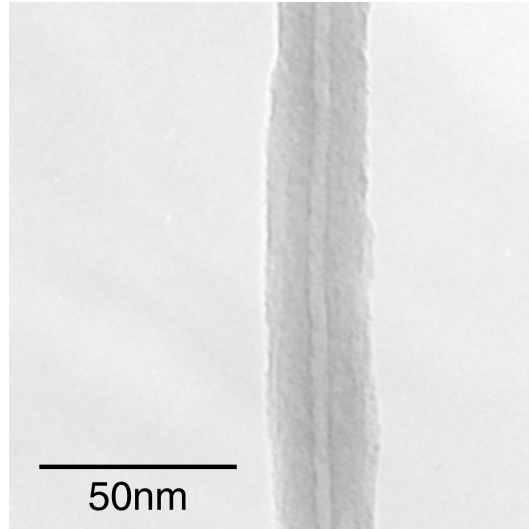


Figure 5.6: BF TEM image of an amorphous nanotube after annealing at 700°C.

material, but Bright Field (BF) TEM pictures (Fig. 5.6) show that the tubular morphology persisted despite the amorphization of the walls. This temperature is ca. 200°C higher than the breakdown temperature of chrysotile to forsterite + water in long term, ambient pressure experiments (= 1 day).²⁰ In experiments run at 750°C during 30 min the tubes are collapsed. For short term experiments (< 30 min) a temperature of 700°C is, therefore, the maximum temperature for which filling is possible. The experimental conditions used for the lead and tin filling experiments e.g. 440°C, 10 Kbar at a heating rate of 50 °C/min guarantee the persistence of the tube morphology through the entire experiment duration. The amorphous Si-Mg-oxide nanotubes are more stable than the crystallized tubes under the electron beam irradiation. The absence of hydrogen in the amorphous walls lowers considerably the probability of knock-on radiolytic processes.

5.3.2 B. Filling experiments with Hg

TEM observations (Fig. 5.7) show that the chrysotile nanotubes are partially filled with liquid mercury. The contrast difference between empty and metal filled parts is noticeable. The average diameter of the Hg-nanowires is 5 nm. Liquid mercury is moving rapidly under the electron beam making it difficult to estimate filling efficiency and to measure the length of individual Hg-nanowires. The maximum Hg-filled length observed was about 350 nm. Hg is present in the inner tubes of almost all fibers with a length > 1 μ m, whereas most of the short fibers were empty. This experiment confirmed that the majority of the chrysotile tubes is unclogged and allow the penetration of suitable liquids.

5.3.3 C. Filling experiments with Pb and Sn

The duration and temperature of the experiments were chosen based on the results obtained in the previous dewatering experiments. Nanotubes pressurized at 10 Kbar and heated at 440°C still

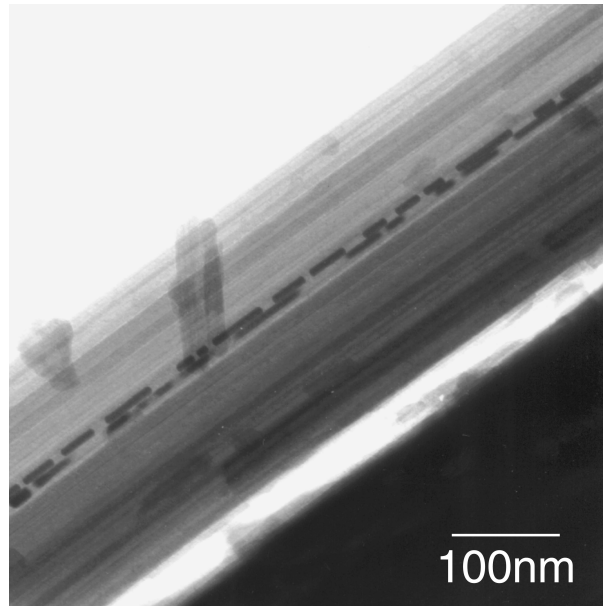


Figure 5.7: BF image of a bundle of chrysotile nanotubes. Two nanotubes are partially filled with mercury nanowires 5 nm in diameter.

show crystalline walls (Fig. 5.8). In the experiment with Pb all chrysotile nanotubes contain lead. The yield for individual tubes is variable and ranges from 10% to 70% (Fig. 9). No discrepancies in the degree of filling are noticed between long and short fibers. Many chrysotile fiber surfaces are covered with lead droplets. The wetting angle is clearly $> 90^\circ$. The quenching of the experimental charge seems to effectively freeze the molten lead inside the tubes. Under electron beam irradiation, however, the metal starts to migrate along the tube as can be seen in two images taken in interval of 10 seconds [Fig. 5.10(a) and Fig. 5.10(b)].

The lowering of the melting temperature for nano-sized particles relative to the corresponding bulk material²⁴ and the heating of the metal through the electron beam are likely, but not the only explanations for this behavior. The particles attached to the outside wall of the fiber have similar or even smaller diameters, but they remain solid and do not move, also after intense electron irradiation (s. left arrow in Fig. 5.10(a) and Fig. 5.10(b)). A possible explanation for this different behavior is the fact that the lead in the interior of the tube was protected from contact with the atmosphere. The lead particles outside the tubes in contrast, could easily be oxidized during sample handling. The melting temperature of the different lead oxides is approximately twice that of metallic lead. An alternative cause could be the influence of hydrogen atoms knocked-on from the tube walls by impinging electrons. Hydrogen, which may concentrate in the interior of the tube, is known to soften metal-metal bonds and to lower the melting temperature of metal clusters.²⁸ Moreover, lead hydride is known to be a very unstable compound. Continuous filling from one extremity to the other for several tubes was noticed, but fast migration and segregation of Pb nanowires along the nanocapillaries impeded imaging of such nanowires.

Although the physico-chemical parameters of tin are not very different from lead, the interior of the chrysotile tubes extracted from the charge are all empty. Only few nanotubes seem to contain tin close to the tube end. Solid tin droplets cover the outer surfaces of fibers found close to bulk tin

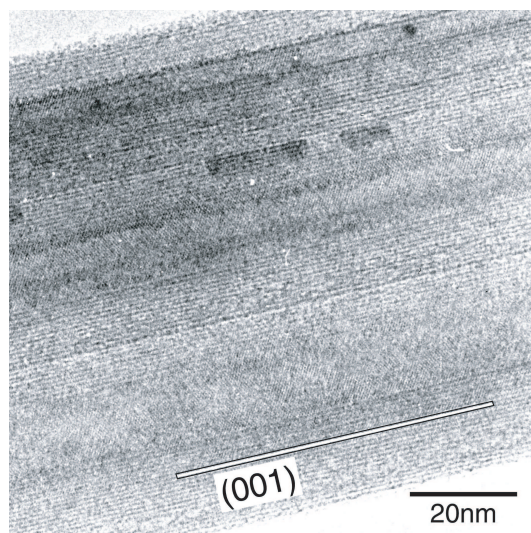


Figure 5.8: HRTEM image of a bundle of chrysotile nanotubes which were heated at 440°C and pressurized at 10 Kbar. The 7.3 Å(001) fringes in the tube wall are visible.

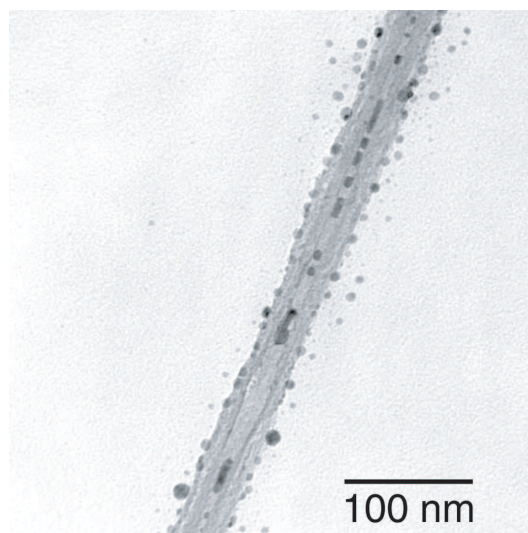


Figure 5.9: BF image of an isolated chrysotile nanotube with a tube diameter of 5 nm partially filled with lead.

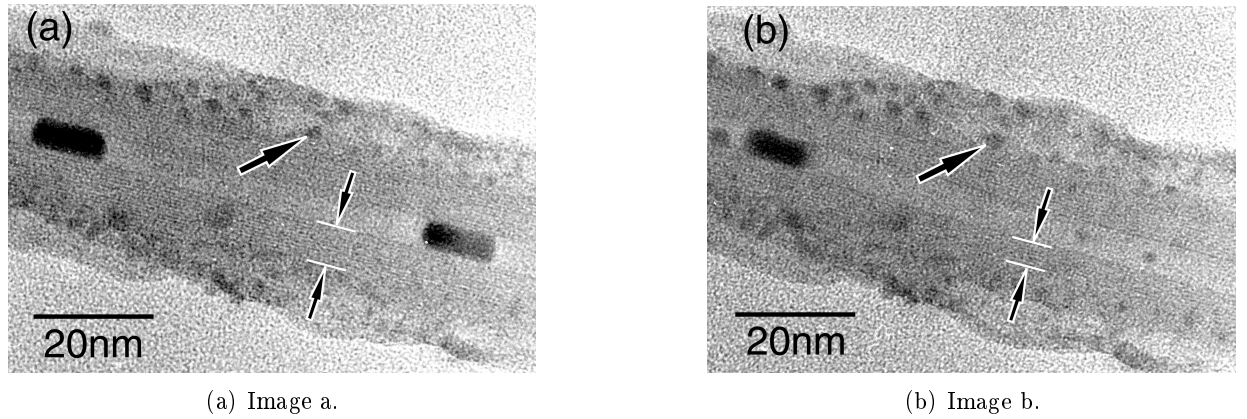


Figure 5.10: TEM images recorded at an interval of 10 seconds. The electron beam induces migration of lead nanowires. Solid Pb droplets are attached to the tube and remain immobile (see left arrow). Amorphization progress caused by electron irradiation is visible as disappearance of lattice fringes (see right arrows).

fragments (Fig. 5.11), a sign that tin was in the molten state and in contact with the fibers during the experiment. In contrast to lead, tin is stable under the electron beam. The droplet shape and the contact angle, which is always $< 90^\circ$, represent, therefore, the values frozen in at 10 Kbar and 440°C. A possible reason for the discrepancy in the filling behavior between Pb and Sn may be a difference in the viscosity of the melts at the experimental conditions.

5.4 IV. CONCLUSIONS

The high pressure and high temperature technique is a suitable method to fill nanotubes with high surface tension metals. 100% of the nanotubes have been partially filled with lead. Based on the survival of the chrysotile morphology up to 700°C, experiments with metals and alloys with higher melting temperature than Pb and Sn e.g. Al and Cu-Sn alloys are currently undertaken. In these experiments the filling process will be influenced by the simultaneous dehydroxylation of the tube walls.

Pressures used in this study were systematically higher than theoretically calculated ones. The lowering of the specific hydrostatic external pressure needed to introduce a metal in chrysotile nanotubes is a goal allowing the use of larger high-pressure containers. The same technique may also be used to fill multiwalled carbon nanotubes (MWCNTs) and single-walled carbon nanotubes (SWCNTs), which have a wider morphological stability range than chrysotile. Removing the phyllosilicate layers of chrysotile nanotubes may be an interesting way to produce metal nanowires of well-defined radius and length. Acidic treatment of the metal filled chrysotile nanotubes is a possible route to reach this goal.

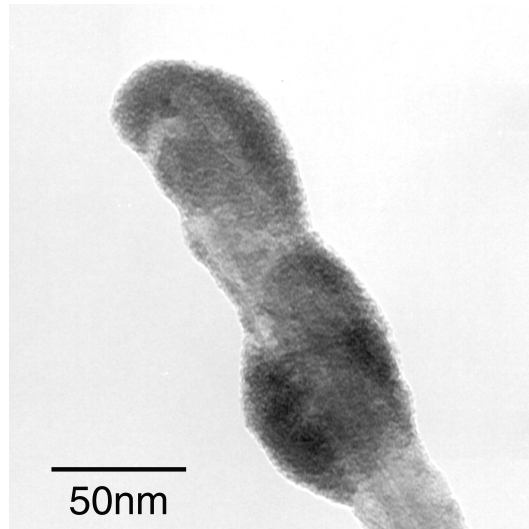


Figure 5.11: BF image of solid Sn droplets wetting a chrysotile nanotube.

5.5 ACKNOWLEDGMENTS

We thank A. Häfner at the ETH Zürich for technical support on the piston-cylinder apparatus and M. Dadras at the Swiss Center for Electronics and Microtechnology (CSEM) for assistance with TEM investigations and useful discussions.

5.6 REFERENCES

1. N.G. Chopra, H. Luyken, V.H. Crespi, K. Cherrey, A. Zettl, and M.L. Cohen, *Science* 269, 966 (1995).
2. M. Nath, A. Govindaraj, and C.N.R. Rao, *Adv. Mater.* 13, 283 (2001).
3. E.J.W. Whittaker, *Acta Cryst.* 9, 855 (1956).
4. K. Yada, *Acta Cryst.* 27, 659 (1971).
5. K. Yada, *Acta Cryst.* 23, 704 (1967).
6. P.J.F. Harris, *Carbon Nanotubes and Related Structures, New Materials for the Twenty-first Century* (Cambridge University Press, Cambridge, 1999).
7. Z.L. Zhang, B. Li, Z.J. Shi, Z.N. Gu, Z.Q. Xue, and L.M. Peng, *J. Mater. Res.* 15, 2658 (2000).
8. P.M. Ajayan, and S. Iijima, *Nature* 361, 333 (1993).
9. E. Dujardin, T.W. Ebbesen, H. Hiura, and K. Tanigaki, *Science* 265, 1850(1994).

10. S.C. Tsang, Y.K. Chen, P.J.F. Harris, and M.L.H. Green, *Nature* 372, 159(1994).
11. J. Sloan, D.M. Wright, H.G. Woo, S. Bailey, G. Brown, A.P.E. York, K.S. Coleman, J.L. Hutchison, and M.L.H. Green, *J. Chem. Soc., Chem. Commun.* 699-700, 699 (1999).
12. M. Terrones, N. Grobert, W.K. Hsu, Y.Q. Zhu, W.B. Hu, H. Terrones, J.P. Hare, H.W. Kraut, and D.R.M. Walton, *Mater. Res. Bull.* 24, 43 (1999).
13. V.N. Bogomolov, and Y.A. Kumzerov, *JETP Lett.* 21, 198 (1975).
14. M.S. Ivanova, Y.A. Kumzerov, V.V. Poborchii, Y.V. Ulashkevich, and V.V. Zhuravlev, *Micro-porous Materials* 4, 319 (1995).
15. S.G. Romanov, and C.M. Sotomayor Torres, in *Nanoscale Science and Technology*, edited by N. Garcia (Kluwer Academic Publishers, Dordrecht, 1998). pp. 255-270.
16. V.V. Poborchii, M.S. Ivanova, and I.A. Salmantina, *Superlattices Microstruct.* 16, 133 (1994).
17. S.G. Romanov, C.M. Sotomayor Torres, H.M. Yates, M.E. Pemble, V. Butko, and V. Tretijakov, *J. Appl. Phys.* 82, 380 (1997).
18. E.A. Zhukov, H.M. Yates, M.E. Pemble, C.M. Sotomayor Torres, and S.G. Romanov, *Superlattices Microstruct.* 27, 571 (2000).
19. G.W. Brindley, and J. Zussman, *Amer. Min.* 42, 461 (1957).
20. M.C. Ball, and H.F.W. Taylor, *Min. Mag.* 33, 467 (1963).
21. G.W. Brindley, and R. Hayami, *Clays and Clay Minerals* 34, 35 (1964).
22. G.W. Brindley, and R. Hayami, *Min. Mag.* 35, 189 (1965).
23. H. De Souza Santos, and K. Yada, *Clays and Clay Minerals* 27, 161 (1979).
24. J.M. Howe, *Interfaces in Materials* (Wiley, New York, 1997).
25. I. Vavrch, *J. Colloid Interface Sci.* 169, 249 (1995).
26. G.J. Hills, and H.J. Høiland, *J. Colloid Interface Sci.* 99, 463 (1984).
27. Z. Wang, P. Lazor, and S.K. Saxena, *Physica B: Condensed Matter* 293, 408 (2001).
28. H. Grönbeck, D. Tomanek, S.G. Kim, A. Rosen: *Z. Phys. D* 40, 469 (1997).

Chapter 6

Tellurium nanotubes

6.1 Introduction

Tellurium (also see section 3.2.8) is a narrow bandgap semiconductor which exhibits a combination of useful properties such as photoconductivity and catalytic activity. Because of its non-centrosymmetry, the trigonal phase of tellurium presents a strong piezoelectric effect [82]. Tellurium has been chosen for PVD templating experiments with chrysotile because of the above cited properties and because it can be directly evaporated from a solid powder or rod and does not need to be melted (such as Al), avoiding any type of uncontrolled interactions between the melted material and the crucible. Tellurium has also been chosen for templating experiments because Furuta et al. (1972) reported the formation of tellurium whiskers on the surface of platinum substrate [33]. They produced spine-, filament- and needle-like whiskers parallel to the [0001] axis of hexagonal lattice in a temperature range of the substrate (T_s) of 90°C to 110°C, 100°C to 140°C and 130°C to 200°C, respectively (see fig. 3.12). At $T_s > 130^\circ\text{C}$, blade-shaped crystals with a growth direction parallel to the c-axis were observed [36]. In this study, high enough evaporation rates were reached at 150°C, 175°C and 200°C well under the melting point of tellurium (449.51°C).

The templating experiments with chrysotile failed but instead the formation of platelets was observed (see fig. 6.3) which (after many trial-and-errors experiments using other templates) could be turned into nanotubes. Tellurium nanotubes were obtained on (111) silicon wafer surfaces and Tellurium nano-rods were obtained on polycrystalline aluminum surfaces (see chapter 7 and fig. 6.3).

6.2 Physical vapor deposition principles

The physical vapor deposition method used in the context of nanowires manufacturing consists in growing a nanowires on a target surface through a three step process consisting in 1) vaporization of the desired solid (or liquid) material 2) transport of the vapor across a low pressure region and 3) condensation of the vapor on a cold target. The substrate structure and desposition conditions

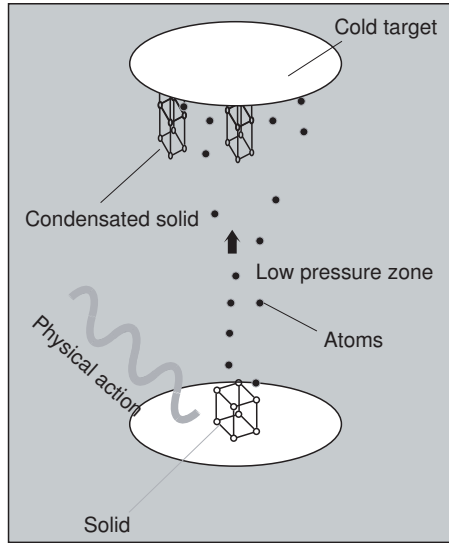


Figure 6.1: Scheme of the physical vapor deposition method. 1) The material to be deposited is vaporized, 2) it is transported across a low pressure region and 3) deposited on a substrate where it finally condensates.

may lead to columnar or whisker like growth (see fig. 6.1).

Every non-vapor phase (liquid or solid) is in equilibrium with its corresponding vapor. The vapor-pressure (VP) is dependent on the temperature of the non-vapor phase. In general, materials with low boiling points will have a higher VP at a given temperature than materials with high boiling points. It has been shown that a partial pressure of 10^{-2} mbar above the solid-gas or liquid-gas interface is needed to achieve good evaporation rates [83]. Therefore Al has to be evaporated in the liquid phase whereas Se, Fe and Te can be evaporated through sublimation (see fig. 6.2). The non-linear evolution of the vapor-pressure with temperature is given by the Claudius-Clapeyron relation. The vapor pressure evolution as function of temperature for different element is depicted in figure 6.2. The physical vapor deposition (PVD) method in ultra high vacuum (UHV) uses the above described phenomenon for deposition of elements or compounds on a cold target where condensation takes place. The experimental setup used for tellurium nanotubes deposition is described in section 3.4.3.

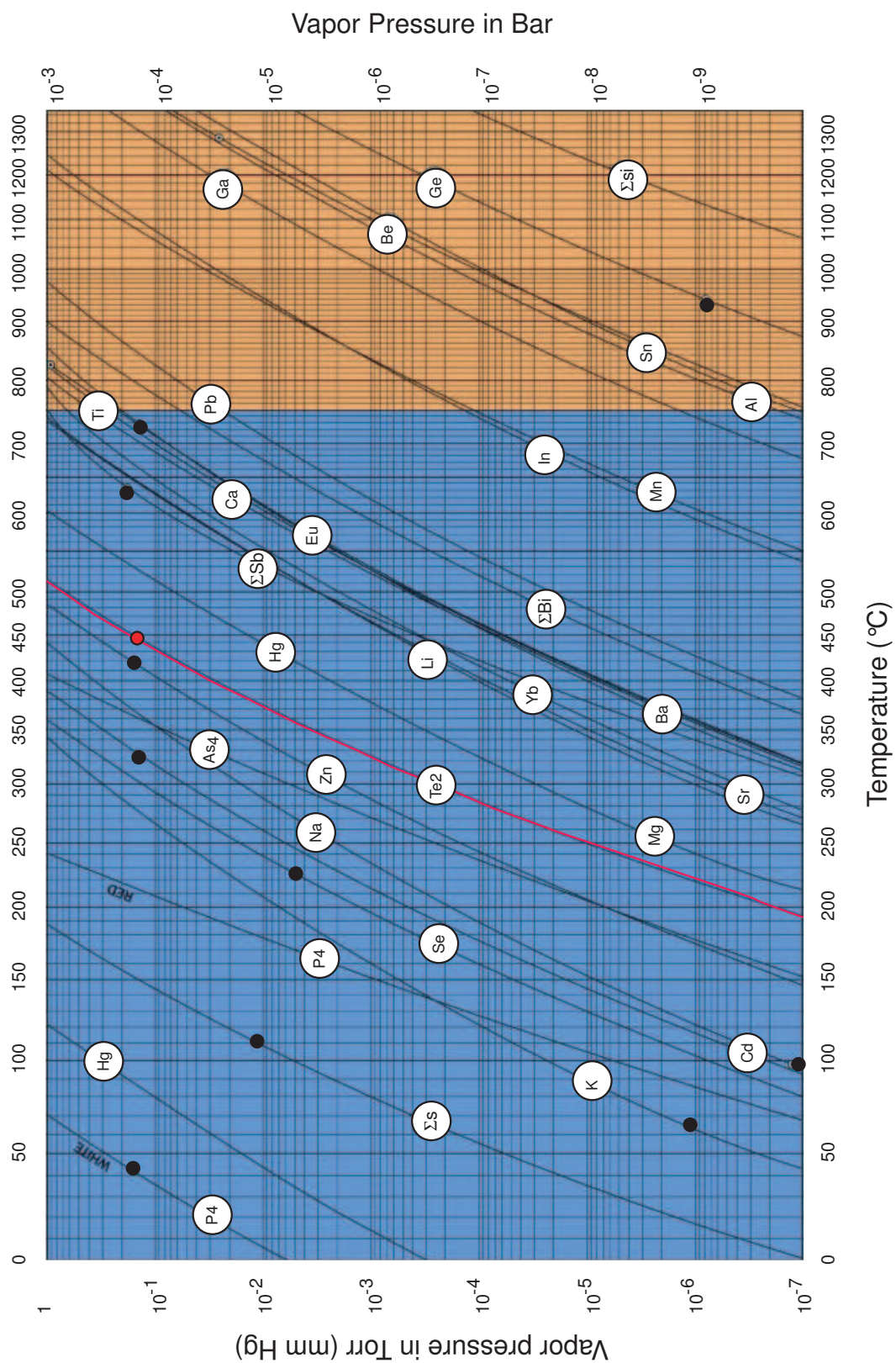


Figure 6.2: Vapor pressure of selected elements in Bar vs. temperature in °C. The melting point of the respective element is marked by a black dot. The curve is in red (Data modified after [84]).

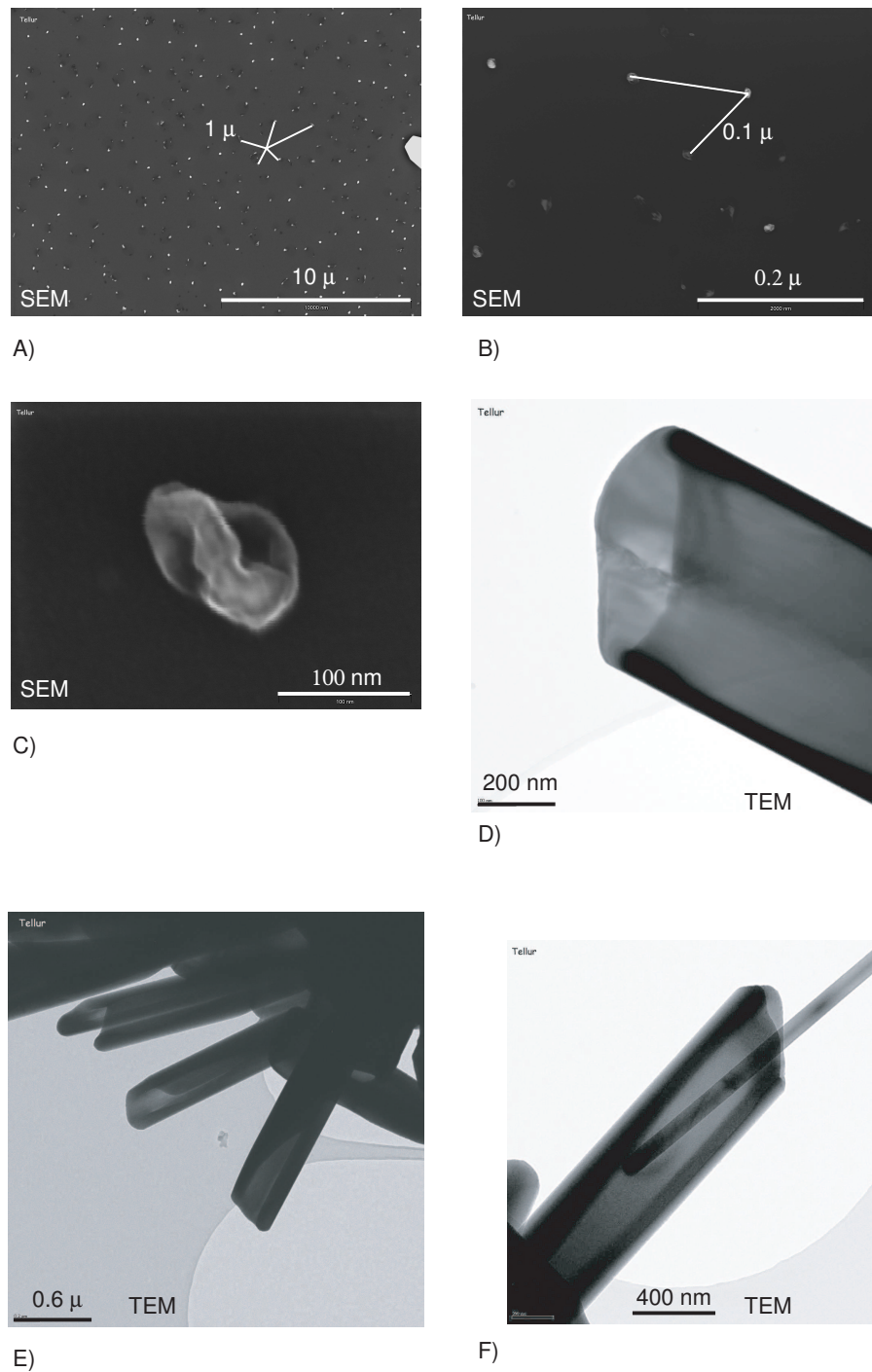


Figure 6.3: A) Te seeds on silicon wafer substrate with apparently 1 μ spacing B) Te seeds at higher magnification, the mean spacing is about 0.1 μ C) Detail on a Te seed D) Te tubes observed with TEM E) Te tubes F) Te tubes.

Chapter 7

Tellurium nanotubes and -rods synthesized by Physical Vapor Deposition

Article published in the **Journal of Material Research**

Vol.19, No. 7 p. 2159 Jul 2004

C. Métraux and B. Grobéty

University of Fribourg, Dep. of Geosciences, Mineralogy Group, 1700 Fribourg, Switzerland

7.1 Abstract

Tellurium nanotubes and -rods were synthesized by physical vapor deposition (PVD) in an induction furnace for reaction times between 25 and 35 min. The growth morphologies depended on the reaction times and the atmosphere in the induction furnace. Nanotubes grew only under argon atmosphere (1 mbar). Under vacuum, tellurium blades and nanorods were observed. Of particular interest are the dense carpets of nanorods observed on polycrystalline aluminum. PVD experiences in a conventional high vacuum coating system did not lead to the formation of nanotubes nor nanorods. The interesting electrical properties of tellurium and tellurium compounds combined with the observed growth morphologies are promising for the fabrication of nanoscale functional devices.

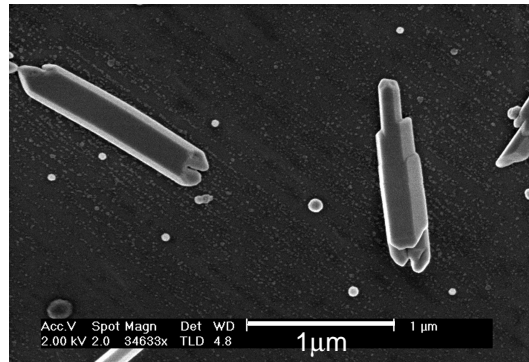


Figure 7.1: Tellurium nanotubes and particles grown under Ar atmosphere (1 mbar) on a (111) silicon wafer in the induction furnace: 25 min of reaction time.

7.2 I. INTRODUCTION

The discovery of carbon nanotubes in 1991¹ has initiated an intensive search for other materials that may form hollow 1D nanostructures. These materials have promising application as nanoelectronic, optoelectronic, electromechanical and electromechanical devices among others.² The search was concentrated on compounds with layered structures and successful synthesis of nanotubes were reported for materials such as boron nitride (BN)^{3–6} and tungsten disulfide (WS₂).^{7,8} Other likely candidates which might crystallize in tube-like morphology are phases with one-dimensional structure elements. Since 2002 different groups were able to synthesize tellurium nanotubes through wet chemical routes.^{9–12} Tellurium is an element with a structure consisting of helical chains parallel to the c-axis. Mayers and Xia used a precipitation technique known as the "polyol process". Elemental tellurium nanotubes formed when ethylene glycol was added as reducing agent to an orthotelluric acid solution. A large number of euhedral seed crystals formed by homogeneous nucleation. Preferential growth at the seed edges led to the development of tubes growing along the [001] and [00-1] directions. The tubes had very well defined hollow interiors with the seed crystal as plug in the center. The crystal dimensions have been controlled by adjusting the concentrations of the reactants. Other compounds with rod- or tube like morphology synthesized by the same wet chemical route are (Se,Te)¹³ - solid solutions and Ag₂Se.¹⁴ In 2003, Wei et al. have used a solvothermal process with N,N-dimethylformamide (DMF) as solvent, KOH as reducing agent and porous silicon (MCM-41) as growth assistant to synthesize tellurium nanotubes.¹¹ In this case the crystallization of tellurium in the form of nanotubes is related to the nano-porous structure of MCM-41 used as template.

In 2003, Se nanorods have been produced on glass by laser ablation under controlled temperature by Jiang et al.¹⁵ In this study, we report the formation of tellurium nanotubes and nanorods through physical vapor deposition (PVD) in an induction furnace under controllable experimental conditions and in high yield.

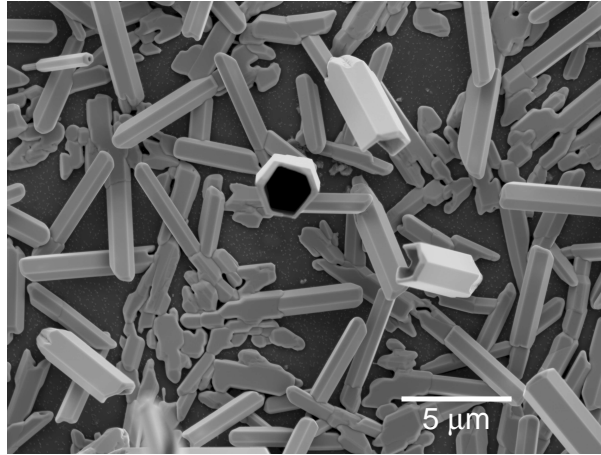


Figure 7.2: Tellurium nanotubes and particles grown under Ar atmosphere (1 mbar) on a (111) silicon wafer in the induction furnace: 30 min of reaction time.

7.3 II. EXPERIMENTAL

7.3.1 A. PVD in an induction furnace

Physical Vapor Deposition (PVD) was performed in a quartz tube (30 cm length, 4 cm in diameter) which was vertically inserted into an induction coil. The elemental tellurium powder (0.05 g) was placed at the bottom of the quartz tube, on a graphite rod. Heating of the tellurium source took place through magnetic induction of the graphite rod. The deposition targets e.g. silicon wafers and aluminum rods were placed at a distance of 2 cm above the tellurium source. The silicon wafers were monocrystalline slabs cut parallel to (111). The aluminum rods were polycrystalline. The tellurium powder (Fluka, Switzerland) was of analytical grade and used without further purification.

The first series of experiments made in the induction furnace were conducted under argon atmosphere (1 mbar). Before the argon was injected, the quartz tube was evacuated to 2×10^{-7} mbar by a turbo-molecular pump. The tube was sealed during the length of the deposition process. Three different reaction times were tested i.e. 25 min, 30 min and 35 min. These reaction times correspond to different final temperature of the tellurium source i.e. 150°C, 175°C and 200°C. The heating rate was of 5 °C/min. For the second series of experiments in the induction furnace, the tube was flushed with argon and evacuated to 2×10^{-7} mbar by a turbo-molecular pump. The vacuum was maintained during the entire deposition process by continuous pumping and no argon was injected. The temperature of the tellurium source was raised to 150°C (25 min of reaction time) at an heating rate of 5°C/min.

7.3.2 B. PVD in a high vacuum coating system

Another set of PVD experiments was performed in a high vacuum coating system equipped with a gas dosing valve to compare the products obtained for same reaction times through conventional evaporation and the products obtained through evaporation in presence of a changing magnetic field

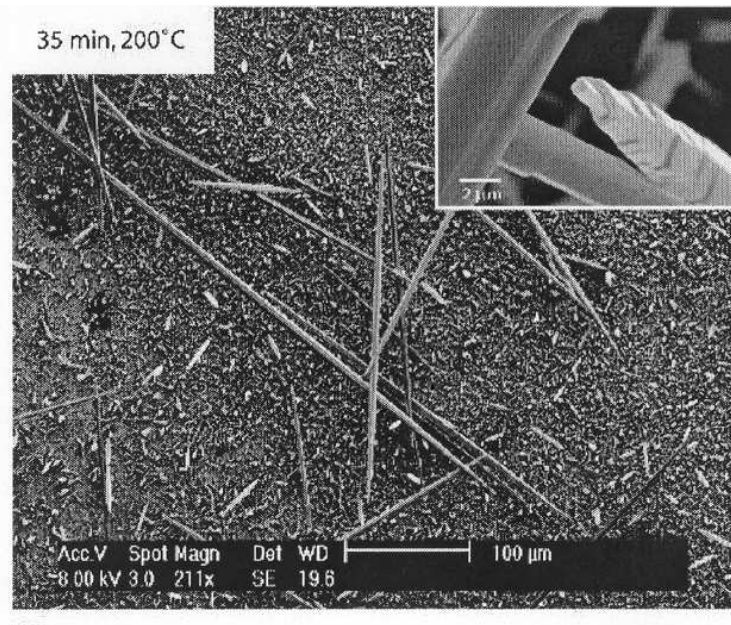


Figure 7.3: Tellurium nanotubes and particles grown under Ar atmosphere (1 mbar) on a (111) silicon wafer in the induction furnace: 35 min of reaction time.

as in the induction furnace. In this case, the tellurium powder (0.05 gr.) was placed in a Ta capsule (7 x 7 x 3 mm) and evaporated on (111) silicon wafers and polycrystalline aluminum rods fixed 2 cm from the tellurium source. A first series of experiments was performed under an Ar pressure of 1 mbar and a second series of experiments was performed under evacuated atmosphere (2×10^{-7} mbar).

7.3.3 C. Electron microscopy

The composition, morphology and size of the PVD products were analyzed with a scanning electron microscope (SEM, FEI XL30 Sirion FEG, Eindhoven, Netherlands) equipped with an energy dispersive spectrometer (EDS, EDAX) operated between 2 and 30 kV and with a transmission electron microscope (TEM, Philips CM200, Eindhoven, Netherlands) operated at 200 kV. Selected area diffraction (SAED) patterns were indexed using the software package EMS.¹⁶

7.4 III. RESULTS AND DISCUSSION

7.4.1 A. Induction furnace

Under argon atmosphere (1 mbar), after 25 min of reaction time (150°C of the tellurium source) and on silicon wafers, tellurium is deposited as rounded particles 50 to 100 nm in diameter, and as hexagonal, hollow crystals (Fig. 7.1). For higher final temperature (175°C) and for corresponding longer reaction time (30 min) the number of tellurium tubes increases (Fig. 7.2). During the 35 min

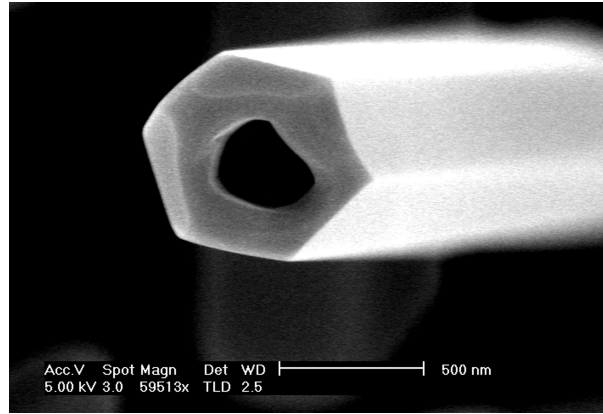


Figure 7.4: Hexagonal tellurium nanotube [detail from Fig. 7.3].

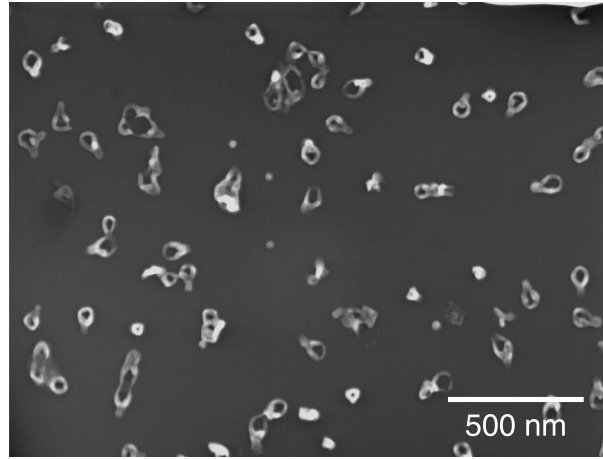


Figure 7.5: Homogeneously distributed tube-like nuclei on (111) silicon wafer grown in the induction furnace [detail from Fig. 7.3].

reaction time experiment millimetric tellurium rods were produced (Fig. 7.3). These millimetric needles occur together with nanoscopic crystals with a helicoidal geometry along the longitudinal axis (detail of Fig. 7.3). The inner diameter of the Te tubes varies from 50 nm to 2 micrometers (Fig. 7.4). The tellurium nanotubes have different inclinations relative to the silicon surface. Some crystal have their 110 surface parallel to the silicon (111), others have their c-axis perpendicular to the substrate. The angle between the tube axes of adjacent crystals is often close to a multiple of 30° . The areas of the wafers not taken by nanometer-sized and micrometer-sized crystals are homogeneously covered by hollow seeds 50 to 100 nm in diameter (Fig. 7.5). For the experiments made on aluminum rods as target and under the same experimental settings, exactly the same reaction products are obtained. Tellurium nanotubes also formed as hollow hexagonal crystals. No noticeable changes in the product yield have been observed between the products crystallized on both substrates.

Under vacuum (2×10^{-7} mbar) and for 25 min of reaction time, the quantity of deposited tellurium on the target in the same laps of time is much larger than under argon atmosphere. Tellurium crystallizes in form of elongated platelets sitting perpendicular to the substrate (Fig. 7.6). Adjacent

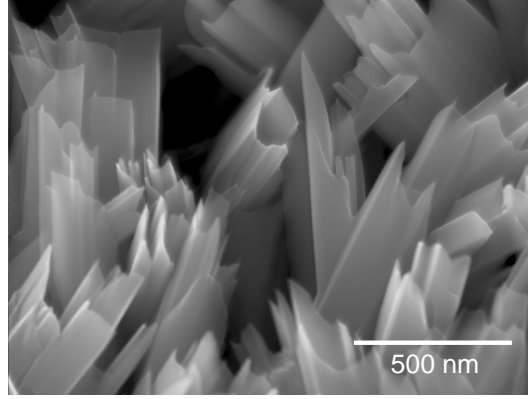


Figure 7.6: Tellurium products grown under vacuum (2×10^{-7} mbar) after 25 min of reaction time in the induction furnace. Platelets grown on a (111) silicon wafer.

platelets have often common edges and are at angle of 60° forming partially closed tubes. On the aluminum substrate a high density of tellurium rods with diameters between 50 and 100 nm have been formed. No tubes have been found. The rod axis is parallel to the c-axis of tellurium (Fig. 7.7).

The energy dispersive spectrometry (EDS) of the run products on silicon wafers revealed only tellurium peaks (Fig. 7.8). SAED patterns (Fig. 7.9) obtained from the different product morphologies could all be indexed for the hexagonal structure of tellurium ($a = 4.45 \text{ \AA}$, $c = 5.92 \text{ \AA}$, $P3_12$). SAED patterns were taken with the entire tube in the aperture. No multiple diffraction patterns were visible. The tube is most likely a hollow single crystal, although merohedral twinning cannot be excluded. Possible twin operations are a twofold axis parallel to c and a mirror plane parallel to (110) as known from α -quartz that has the same space group as tellurium.^{17,18} It is, however, almost impossible to do the necessary dark field imaging to test the presence of twinning because most electrons contributing to the diffraction pattern traverse more than one face of the hexagonal tube. If the hollow crystal would be the result of twinning, they would be diffracted by more than one twin member and possible structure factor differences of equivalent reflections are not usable anymore. The fact that nanotubes nucleate on seeds that are not hollow is more in favor of a single crystal than of a twinned crystal. The above twin symmetry operation would be reflected by a stacking fault along the twin boundary. No contrast compatible with such a stacking fault has been observed. The defect concentration, mainly dislocations, is very low. Bright field images reveal that there are also occasional plugs along the tube (Fig. 7.10). Tellurium micro- and nanotubes remained stable also after storage in air over periods of several months.

The formation of the tubes and rods can best be described by a nucleation and growth process. Two nucleation events can be distinguished on the silicon substrate. Initially, the evenly distributed hollow seeds ($15 \text{ seeds}/\mu\text{m}^2$) form through homogeneous nucleation. Their crystallographic orientation seems to be controlled. There is an obvious relationship between the unrelaxed (111) surface unit cell of silicon and the basal plane dimensions of the tellurium structure e.g. $2 a_{surf}^{Si(111)} = 3 a_{bulk}^{Te}$ with a mismatch of only 0.9%, leading to preferential nucleation of tellurium with (001) Te parallel to (111) Si (Fig. 7.11). The growth of the homogeneous nuclei seems to be blocked by the faster growth of non-epitaxial nuclei, which depletes the tellurium concentration close to

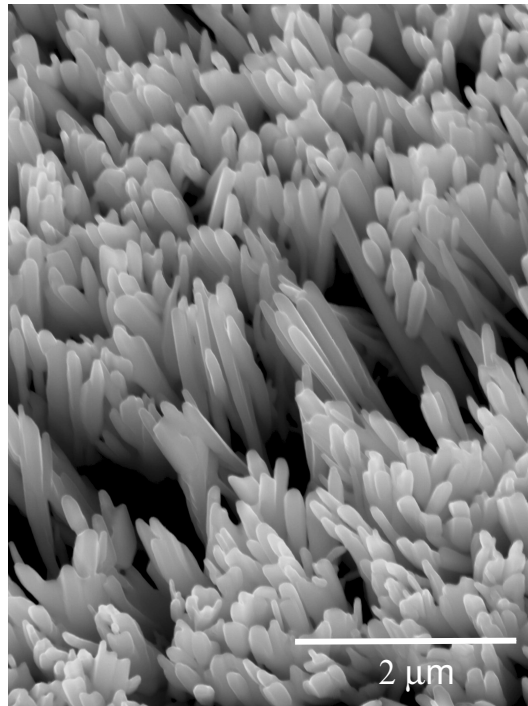


Figure 7.7: Tellurium products grown under vacuum (2×10^{-7} mbar) after 25 min of reaction time in the induction furnace. Nanorods grown on a aluminum foil.

the substrate. These nuclei are probably tellurium seeds that crystallized already before hitting the substrate. The model proposed for the appearance of well-shaped, hollow, hexagonal crystals in the wet chemical synthesis route might also serve as explanation for the PVD grown tellurium nanocrystals. Preferential attachment of solute atoms at the edges depletes the central portion of the 001 faces. Additional tellurium atoms will continue to attach at these energetically favorable edge sites leading to the observed hollow crystals. In the wet chemical synthesis, hollow crystals were only obtained by keeping the tellurium precursor (TeO_2) concentration low.⁹ This was achieved by adding orthotelluric acid instead of tellurium dioxide. The slow decomposition kinetics of the acid controlled the oxide concentration and consequently the elemental tellurium concentration. The dilution of the tellurium gas by the argon gas added to the PVD furnace atmosphere might have the same concentration controlling effect.

The oriented growth of the rods on the aluminum foil, however, seems not to be controlled by crystallography. Similar oriented growth of tubes was observed in the PVD synthesis of carbon nanotubes.¹⁶ These tubes were also grown on aluminum substrates, but with additional iron carbide nanocrystals as nucleation seeds. The oriented growth was explained by steric hydrance. The only direction of unimpeded growth is perpendicular to the substrate. In the case of tellurium, the rod shape crystal morphology may be explained by the fast growth parallel to the *c*-axis which is only possible without influence by neighboring crystals for seeds with the *c*-axis perpendicular to the substrate. Reasons for the high density of nucleation seeds with the *c*-axis perpendicular to the substrate are not clear yet.

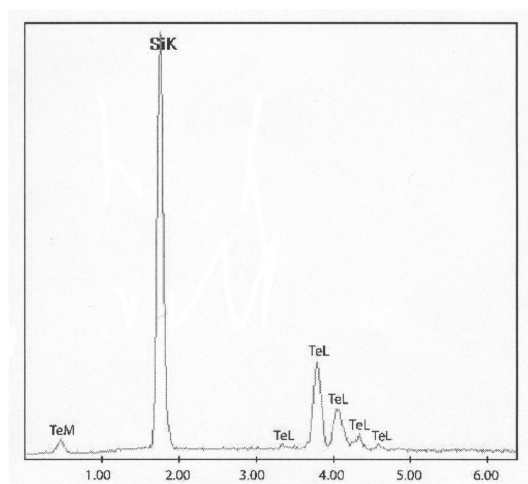


Figure 7.8: EDS spectra of a tellurium nanotube.

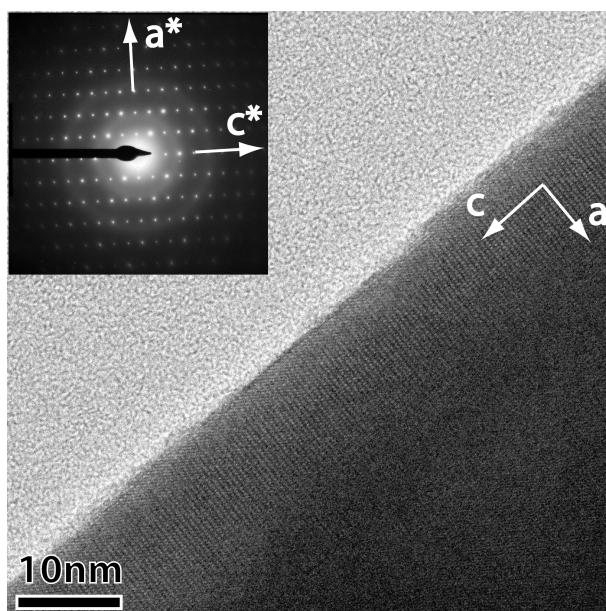


Figure 7.9: Microdiffraction on a tellurium tube deposited on a (111) silicon wafer.

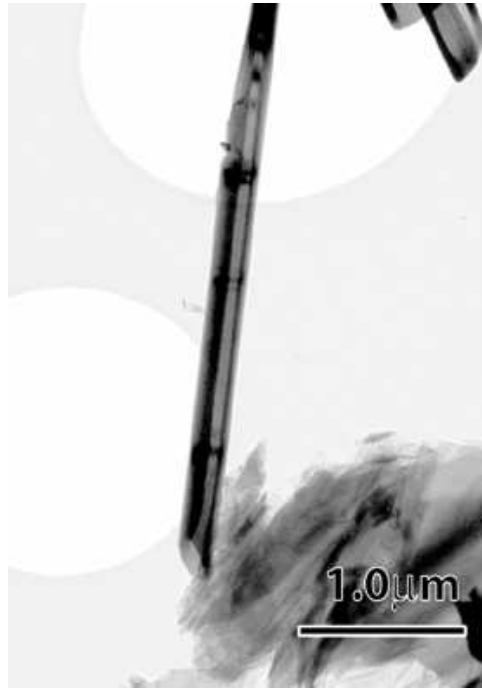


Figure 7.10: Bright-field image of tellurium tubes.

7.4.2 B. High vacuum coating system

When PVD was performed in the high vacuum coating system and therefore without the assisting magnetic field used for induction heating we did not observe the formation of tellurium tubes nor rods. This observation is valuable for both type of substrate, for experiments made under vacuum (2×10^{-7} mbar) as well as for experiments made after the evacuation of the reaction chamber to 2×10^{-7} mbar and subsequent injection of 1 mbar of Ar and for same reaction times. The products are strictly the same on both substrates. Under vacuum, the products were elemental tellurium platelets, comparable to the ones obtained in the induction furnace under vacuum and on (111) silicon wafer (s. Fig. 7.7). Under 1 mbar of Argon, the products were dendritic tellurium filaments. These results show the importance of the magnetic field as main controlling agent for the growth of tellurium nanotubes.

7.5 IV. CONCLUSIONS

Nanostructured tellurium products with different shapes have been produced through a simple physical vapor deposition process. By PVD, as described in this paper, the synthesis of tellurium nanotubes is achieved without any template or catalyst. This technique considerably simplifies the subsequent purification process needed with wet chemical synthesis. Moreover by wet chemical synthesis relative long reaction times are needed.¹¹

The tubular morphology of the run products is dependent on the presence of an assisting high

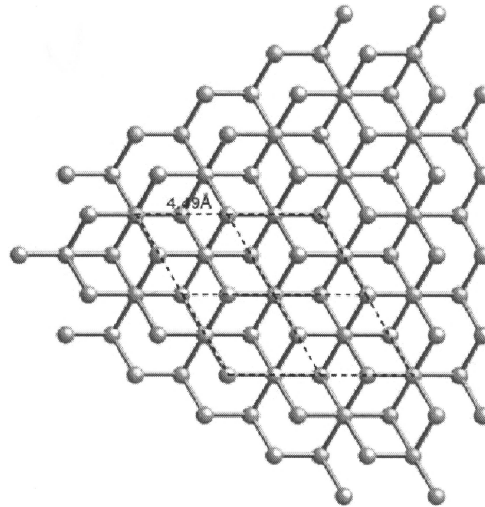


Figure 7.11: Unrelaxed (111) silicon surface layer (two atom thick) projected along [111]. The silicon atoms describing the indicated hexagonal array (stippled line) are not at the same level along [111].

frequency magnetic field and on the atmosphere of the reactor. By controlling the reaction time, the aspect ratio of the products can be controlled. PVD-synthesized tellurium crystals exhibit the same rod and tube shaped morphology as observed during wet chemical synthesis. However, PVD allows oriented growth.

Tellurium, selenium and alloys of the two elements are p-type semiconductors and show piezoelectricity. Their electric properties have unusual temperature dependencies. Selenium has a very high photoconductivity. Tellurium and selenium are, moreover, constituents of semiconductor materials such as CdSe, CdTe and ZnTe. These interesting electrical properties of tellurium and tellurium compounds combined with the observed growth morphologies are promising for the fabrication of nanoscale functional devices. The oriented growth of rods, for example, makes tellurium a candidate for electron emitter applications. Emission current measurements are currently undertaken.

7.6 ACKNOWLEDGMENTS

We Thank Dr. A. Zuettel at the University of Fribourg for useful discussions. We thank C. Neururer at the University of Fribourg for assistance with SEM investigations and technical support. We Thank Dr. M. Dadras at the Service for Microscopy and Nanoscopy at the University of Neuchâtel for useful discussions.

7.7 REFERENCES

1. S. Iijima, Nature 354, 56 (1991).

2. P.J.F. Harris, Carbon Nanotubes and Related Structures, New Materials for the Twenty-first Century (Cambridge University Press, Cambridge, United Kingdom, 1999).
3. P. Gleize, M.C. Schouler, P. Gadelle, and M. Calliet, J. Mater. Sci., 29, 1575 (1994).
4. N.G. Chopra, H. Luyken, V.H. Crespi, K. Cherrey, A. Zettl, and M.L. Cohen, Science 269, 966 (1995).
5. I. Narita, and T. Oku, Diamond and Related Materials 12, 1912 (2003).
6. D. Goldberg, A. Rode, Y. Bando, M. Mitome, E. Gamaly, and B. Luther-Davies, Diamond and Related Materials 12, 1226 (2003).
7. R. Tenne, L. Margulis, M. Genut, and G. Hodes, Nature 360, 444 (1992).
8. M. Nath, A. Govindaraj, and C.N.R. Rao, Adv. Mater. 13, 283 (2001).
9. B. Mayers and Y. Xia, Journal of materials chemistry 12, 1875 (2002).
10. B. Mayers and Y. Xia, Adv. Mater. 14, 279 (2002).
11. G. Wei, Y. Deng, Y.-H. Lin, and C.-W. Nan, Chem. Phys. Lett., 372, 590 (2003).
12. X.-Y. Liu, M.-S. Mo, X.-Y. Chen, and Y.-T. Qian, Inorg. Chem. Comm., In press.
13. B. Mayers, B. Gates, Y. Yin and Y. Xia, Adv. Mater. 13, 1380 (2001).
14. B. Gates, B. Mayers, Y. Wu, Y. Sun, B. Cattle, P. Yang and Y. Xia, Adv. Funct. Mater., 12, 679 (2002).
15. Z.-Y. Jiang, Z.-X. Xie, S.-Y. Xie, X.-H. Zhang, R.-B. Huang and L.-S. Zheng, Chem. Phys. Lett., 368, 425 (2002).
16. P. Stadelmann, Ultramicroscopy, 21, 131 (1987).
17. A.C. McLaren, P.P. Phakey, Phys. Stat. Sol. 13, 413 (1966).
18. A.C. McLaren, P.P. Phakey, Phys. Stat. Sol. 31, 723 (1969).
19. P. Mauron, C. Emmenegger, A. Zuettel, Carbon, 40, 1339 (2002).

Chapter 8

Imogolite nanotubes

8.1 Introduction

Imogolite is a naturally occurring hydrous aluminosilicate mineral of nanotubular morphology (see fig. 8.1) with formula $\text{Al}_2(\text{OH})_3\text{SiO}_3\text{OH}$. The ratio $\text{SiO}_2 / \text{Al}_2\text{O}_3$ is about unity [85]. Imogolite has been discovered by N. Yoshinaga and S. Aomine in 1962 [40] in clay fractions of the volcanic andosol "imogo" (Kyushu Island, Japan). The tubular morphology of the imogolite aluminosilicate was recognized by Russell et al. [86]. The diameter of imogolite nanotubes is approximately 2 nm, they have a constant diameter and are single-walled [2]. The substitution of germanium for silicon increases the imogolite diameter [87]. The structure of imogolite differs markedly from the structure of allophane and other poorly crystalline materials often of rounded nodular appearance [88]. The study of imogolite nanotubes presented here will specially focus on the tubular crystal structure and on the bundle arrangement of the nanotubes. The powder XRD patterns published so far on imogolite are quite different from each other [89], [90], [91] [92]. Therefore, the present attempt to understand the difference by calculating and verifying XRD-patterns for a series of model structures will help to interpret properly this variety of patterns.

8.2 Potential and known applications

Imogolite has been successfully used for the manufacturing of PVA films with improved mechanical and optical properties [93]. Imogolite has also been used as catalyst support [94]. After removal of adsorbed condensed water at 200°C (275°C for small pores) imogolite shows a potential for gas storage [95] [89]. Al-Ge imogolite nanotubes are candidates for use in ion-channel devices because of their hydrophilic interior, solid-state structure and short length [91].

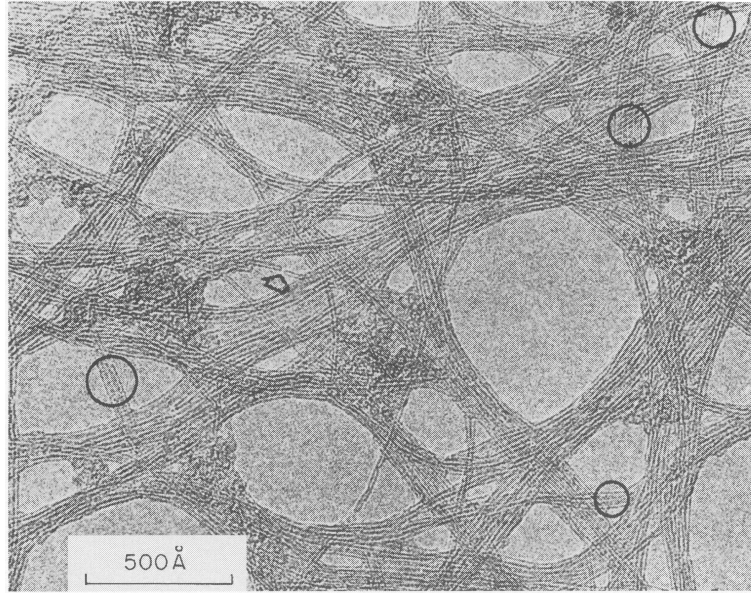


Figure 8.1: Imogolite aluminosilicate tubes (after [2]).

8.3 Synthesis

Imogolite was first synthesized by Farmer et al. using a millimolar solution of monosilicic acid (H_4SiO_4) and aluminum chloride (AlCl_3) adjusted to pH 5 with NaOH, thereafter acidified by adding HCl and finally refluxing between 96°C and 100°C [41] for several time periods. Wada et al. used tetraethyl orthosilicate ($\text{Si}(\text{OC}_2\text{H}_5)_4$) instead of H_4SiO_4 [96]. C. Koenderink et al. [90] used aluminum-sec-butoxide (ASB) instead of AlCl_3 and tetraethyl orthosilicate (TEOS) for the synthesis of sol-gel imogolite.

In this study, we used a imogolite sample (IMOAM sample) synthesized by S. Mukherjee and S. Nair (Georgia Institute of Technology) using aluminum chloride (AlCl_3) and tetraethyl orthosilicate $\text{Si}(\text{O}(\text{C}_2\text{H}_5))_4$. AlCl_3 was mixed with an aqueous solution of $\text{Si}(\text{O}(\text{C}_2\text{H}_5))_4$ (TEOS). The final concentration of the solution was 5 mmol/L with respect to Al and 2.77 mmol/L for Si resulting in a Al/Si ratio of 1.8. The solution was stirred 1 min (AlCl_3 is hydrolyzed) and TEOS was added dropwise. The final solution was stirred at room temperature for 45 min (TEOS is hydrolyzed). Then, NaOH 0.1 N was added under vigorous stirring at a rate of 0.3 ml/min using a push syringe to reach pH5. This corresponds to about 30 to 40 ml of NaOH (the total titration time was about 2h00). During titration, it is very important to avoid the condensation of the precursors. Once pH 5 was reached 1 mmol of HCl 2N and 2 mmol of acetic acid 10% were immediately added. The solution must still be clear and pH should be around 4.5. The solution was then refluxed for 120 hours at 95°C (cleanliness of the reflux apparatus is of importance). The formation of imogolite nanotubes has been reported after 10 hours. The refluxed solution was basified with NH_3 until pH reaches 8 in a vessel under vigorous stirring. The solution was then centrifuged at 3000 rpm for 20 min a gel was deposited at the bottom. The supernatant was discarded. Few drops of HCl 12N were added to the remaining gel in order to fluidify it. As soon as the gel was mobile it was transferred into a dialyze membrane where it was left two days in order to remove NaCl formed during the process. Finally the sample

was freeze dried in order to get a solid imogolite sample (white powder). Low ion concentration (millimolar solutions) seems a condition for high imogolite yields. The NaOH concentration and titration rate seems of no importance, but a Al/Si ratio > 1.8 improves the formation of Bohemite ($\text{AlO} \bullet \text{OH}$) which is not desired (S. Mukherjee personal communication).

8.4 Formation

When imogolite is synthesized using ASB and TEOS, the growth of the Al-O-Al network (gibbsite like sheet) probably proceeds via several steps: hydrolysis, olation (preferential elimination of water) and oxolation (preferential elimination of alcohol) (see fig. 8.2).

A mechanism which involves the formation of imogolite from intermediate "proto-imogolite" sheet particles similar to gibbsite layers ($\text{Al}(\text{OH})_3$) has been proposed by several authors [97] [90]. This "proto-imogolite" could eventually develop curvature due to the binding of attaching silicate groups. The curvature is thought to result from the difference in bond length of the Al-O and Si-O bonds (0.19 nm and 0.16 nm, respectively) and the tetravalent silicon atoms pull the oxygen atoms of the aluminum hydroxide layer into a curved cylinder. Despite many investigations, the "proto-imogolite" existence is still controversial [91].

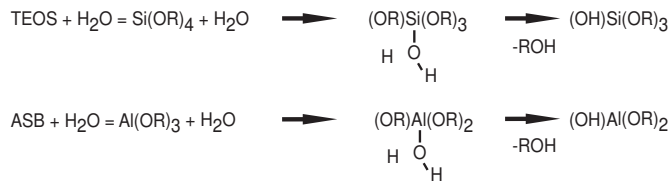
Two types of reaction controls on the formation of nanostructures through mild chemistry have been proposed [91] 1) kinetic control (with intermediate products) 2) Thermodynamic control (without intermediate products). S. Mukherjee et al. found evidences for a thermodynamic control of the imogolite formation. They based their conclusion on the fact that the length of imogolite nanotubes remains stable through the synthesis process. Fig. 8.3 depicts a general view of a possible synthesis way.

8.5 Crystal structure of the tube

Unlike chrysotile which is a multiwalled nanotube consisting of cylindrical TO-layers, imogolite is a single-walled nanotube similar to single-walled carbon nanotubes [42]. For the XRD calculations and structure refinement presented in chapter 9, a crystallographic rigid-body model of an imogolite tube has been computed allowing batch calculations for single imogolite tubes and bundles with various geometries. The crystallographic model for a single tube is based on the fractional cylindrical atomic coordinates proposed by Cradwick et al. [42] (see table 8.1). The code allows the stacking of the single tubes to bundles with variable geometry. The tunable parameters of the crystallographic model are summarized in table 8.2, the most relevant ones being the number of unit cells around the tube axis and the parameters describing the bundle "unit cell" (= supercell). Different crystallographic models for both the single tube (variable size) and tube bundles (geometry) are presented in chapter 9. The Si-O bonds length have been computed in order to better constrain the validity of the model. Models producing Si-O bonds bigger than 1.8 Å have been discarded.

Fig. 8.4 depicts imogolite nanotubes computed for two different sizes ($n = 10$ and 12). The radius of the nanotubes is function of the number n of rotational unit cells around the tube axis (see table

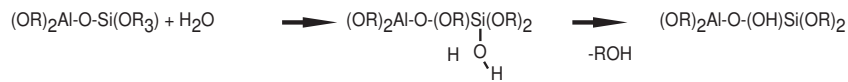
1) **Hydrolysis:** The products are instable hydroxyalkoxides



2) **Olation:** The hydrolysis products react together: Polycondensation.



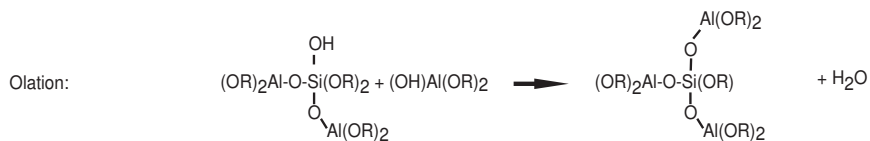
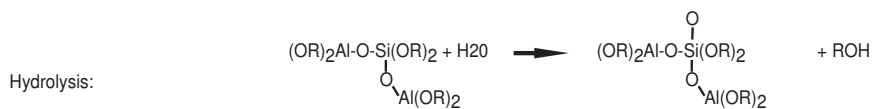
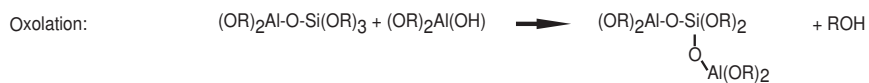
The product of olation may be submitted to hydrolysis



3) **Oxolation:** An hydrolysis products reacts with a row product: Polycondensation.



Proposed steps for imogolite synthesis



In imogolite, the oxygen is triply bridging:

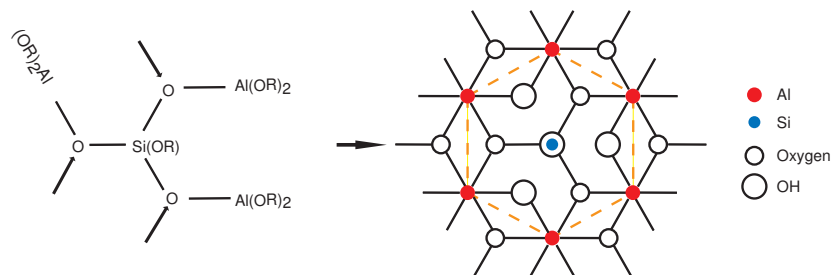


Figure 8.2: Hydrolysis, olation and oxolation processes. Proposed steps for imogolite formation.

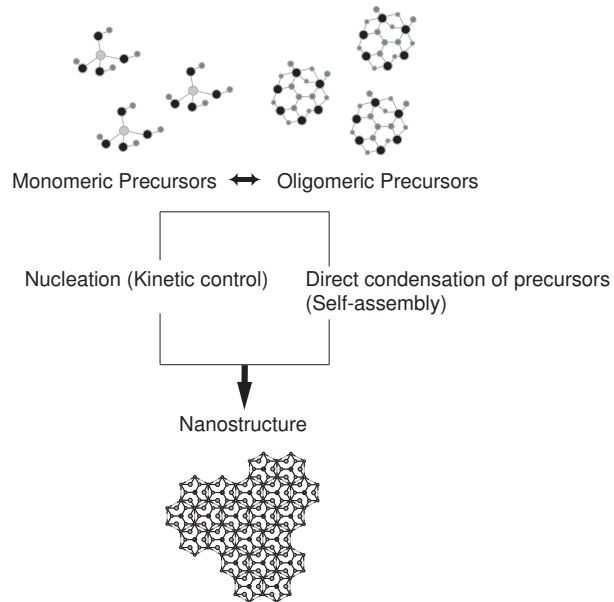


Figure 8.3: Monomeric precursors form oligomeric precursors which can lead to the formation of a nanostructure through 1) inorganic polymerization or 2) by self-assembly (modified after S. Mukherjee et al. [91]).

Table 8.1: Atomic cylindrical coordinates of tubes with C_{2nh} symmetry

Atom	C_{20h}			C_{24h}		
	r Å	ψ (degree)	c Å	r Å	ψ (degree)	c Å
OH(Si)	4.78	-1.94	0	5.74	-1.62	0
Si	6.40	-1.94	0	7.36	-1.62	0
O ₁	6.97	11.98	0	7.93	9.99	0
O ₂	6.97	-6.01	1.4	7.93	-5.00	1.40
Al	8.05	0.00	2.7	9.01	0.00	2.70
(OH) ₁	9.13	-13.73	0	10.09	-11.44	0
(OH) ₂	9.13	7.08	1.67	10.09	5.92	1.67

Table 8.2:
Parameters used in the structural model

Par.	Description	Unit/type	Range	Comment
n	number of unit cell around the tube axis	integer	10-24	n influences the imogolite unit cell dimensions [a=f(n),b=2 π n] but not c
f(n)	relation giving the radial position of an atom as function of n	-	-	$r(\text{atom}) = C * n$ where $C1 = \frac{r(c20h)_{\text{atom}}2\pi}{10}$ or $r(n)_{\text{atom}} = (n-10) * C + r(c20h)_{\text{atom}}$, where $C2 = \frac{r(c24h)_{\text{atom}} - r(c20h)_{\text{atom}}}{2}$
C2	coefficient in the second f(n) function	Å	-	-
a	a parameter of the bundle unit cell	Å	-	-
b	b parameter of the bundle unit cell	Å	-	-
c	c parameter of the bundle unit cell	Å	8.4-9.4	-
α	angle between b and c	degree	90	-
β	angle between a and c	degree	60-90	-
γ	angle between a and b	degree	90	-
h	are the hydrogen atoms modeled yes/no ?	boolean	y/n	hydrogen atoms were taken into account
RC	radial compression factor	dimensionless fraction	0-1	1 was used
LC	limit for connectivity matrix	Å	2-3	2.5 Å was used
TF	radial tube fraction simulated	dimensionless fraction	0-1	1 was used
L	length of the tube	Å	8.4-1680	-

8.2). The two functions used in this study for describing the variation of r relatively to n and are in table 8.2.

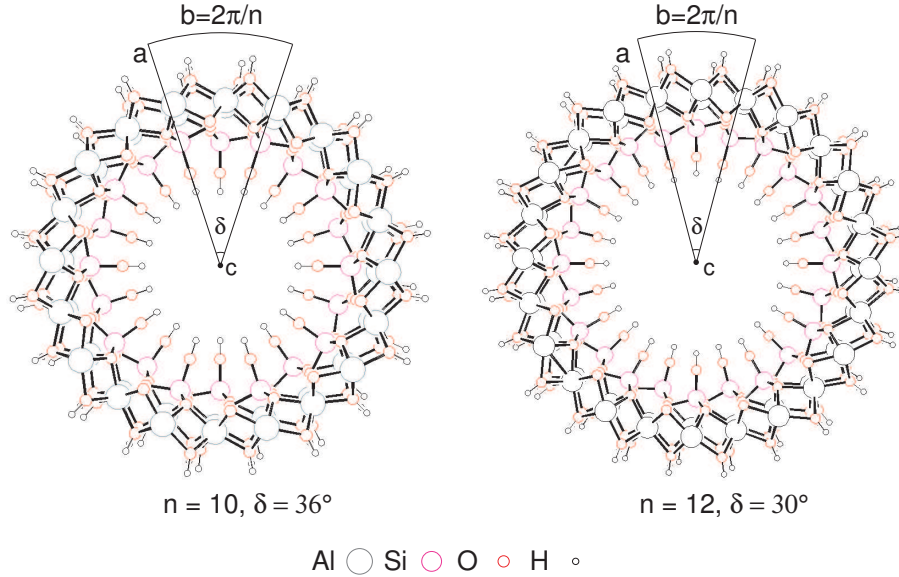


Figure 8.4: Imogolite tubes with various number of units cells around the tube axis can be modeled. Left, imogolite with 10 unit cells. Right, imogolite with 12 unit cells. The radius and δ of the imogolite is a function of n .

8.6 Geometry of bundles

In 1985, Van der Gaast et al. proposed a hexagonal dense packed model for bundles of synthetic imogolite nanotubes [98]. A monoclinic packing model has recently been proposed by Mukherjee et al. [91]. In chapter 9 we present XRD calculations on imogolite bundles where we successfully use a monoclinic packing model instead of a hexagonal one to fit measured XRD patterns. Fig. 8.5 depicts the different parameters used for bundle calculations ($[100]$, $[010]$, $[001]$, α , β and γ). The bundles modeled in this study can therefore adopt geometries ranging from monoclinic to hexagonal.

8.7 XRD calculations

The rigid-body structural model of imogolite bundles presented above was used to perform XRD calculations using the "Powdercell" software application [99]. The fit between calculated and measured patterns was evaluated using, in a first step, the weighted residual R_{wp} and the 'goodness-of-fit' $S = \frac{R_{wp}}{R_{exp}}$ where R_{exp} is the expected residuals [100]. In a second step, the models with the best fit parameters were evaluated visually. Based on measured imogolite nanotubes diameters (under TEM) it has been postulated by several authors [101], [102], [97] that synthetic imogolite has a higher number of unit cells ($n=14$) around the tube axis than its corresponding natural species ($n=12$). The results of simulated XRD patterns and their comparison to measured XRD patterns

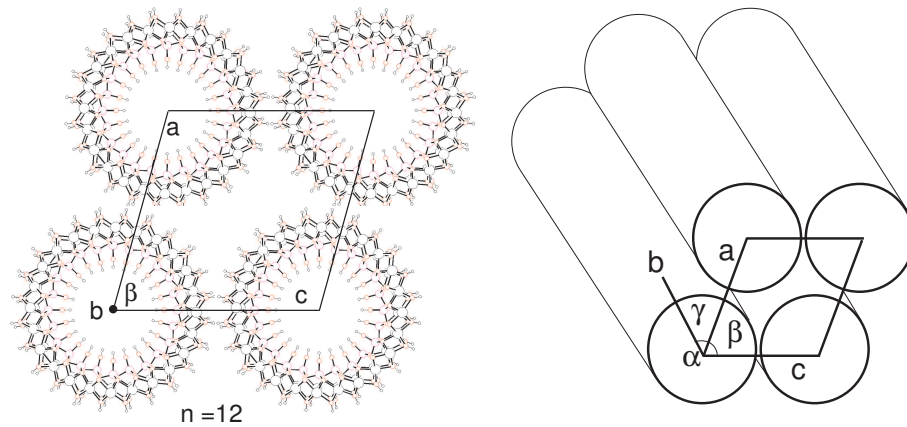


Figure 8.5: In this study, the bundle arrangement of imogolite nanotubes are described with 6 parameters namely a , b , c , α , β , γ . Left) view parallel to the tube axis. Right) oblique view.

are presented in chapter 9, where we confirm the monoclinic model and the suggested differences in n .

8.8 Thermal stability

The thermal stability of natural imogolite nanotubes has been studied by Wada et al. [85]. It was shown that the tubes are stable up to 250°C, which is the temperature where dehydroxylation takes place ([85]). The imogolite structure is destroyed between 350°C to 400°C. Weight lost analyses showed that 65 to 75 percent of the total structural OH groups are lost between 250°C and 500°C.

Chapter 9

Structural model and XRD calculations of imogolite aluminosilicate nanotubes

Article submitted to the *European Journal of Mineralogy*, February 2008

C. Métraux, B. Grobét

University of Fribourg, Dpt. of Geosciences, 1700 Fribourg, Switzerland

9.1 Abstract

XRD calculations have been performed using a crystallographic rigid-body model of imogolite nanotubes arranged in regular arrays (bundles) of different geometries. The calculated XRD patterns have been fitted to experimental data of natural and synthetic imogolite samples. Natural imogolite is shown to consist in Si-Al nanotubes with 12 unit cells around the tube axis and synthetic imogolite to consist in Si-Al nanotubes with 14 or 15 unit cells around the tube axis. The differences in XRD patterns published so far can be modelled by varying the subcell (tube) parameters and the supercell (bundles) parameters of the crystallographic rigid body model. The results of these XRD calculations and fitting experiments could be used for better interpretations and indexing of XRD patterns in future research on imogolite nanotubes.

9.2 Introduction

Imogolite is a naturally occurring hydrous aluminosilicate mineral discovered by Yoshinaga and Aomine (1962) in clay fractions of the volcanic andosol called "imogo" (Kyushu Island, Japan). The presence of imogolite has also been reported by Gense (1973) in andosols of the Réunion Island (France) and by Lulli et al. (1983) in andosols of Mount Vulture (Italy) among others. Imogolite should not be confused with allophane and other poorly crystalline aluminous materials (Wada, 1967, Henmi and Wada, 1976). The following factors controlling the formation of natural imogolite from volcanic rocks were given by Gense (1973): 1) good water drainage 2) good permeability of the bedrock 3) rainfall above 1700 mm/year and 4) a mean annual temperature under 17 °C. The fibrous morphology of natural imogolite and its gel-like aspect were described by Russell et al. (1969). The stoichiometric formula of imogolite is $\text{Al}_2(\text{OH})_3\text{SiO}_3\text{OH}$ (Wada and Yoshinaga, 1969). Wada (1969) proposed a structural model for imogolite based on "DNA-like" chain molecules elaborated by Vainshtein (1966) for biomolecules. The tubular morphology of imogolite was discovered later by Russel et al. (1969) and Wada et al. (1970) using electron microscopy and hence the chain model proposed by Wada (1969) had to be reviewed. The external diameter of the tube was found to be about 2.5 nm and the inner diameter less than 1 nm. The tube length varied from several hundred nanometers up to micrometers. Using electron diffraction data, Cradwick et al. (1972) proposed a structural model of imogolite based on a tubular gibbsite ($\text{Al}(\text{OH})_3$) sheet with isolated silicate anions (SiO_4)[−] attached to the interior of the rolled sheet. The orthosilicate anions occupy each vacant octahedral site (1/3) of the gibbsite layer. In this model, the bending of the gibbsite sheet is explained by a shortening of O-O distances around the vacant octahedral site caused by the misfit between the O-O distance of the silicate anions and the corresponding O-O distance of the gibbsite layer. The nanotubes stack in ordered arrays controlled by hydrogen bonds between the tubes (Tamura and Kawamura, 2002). Van der Gaast et al. (1985) first assumed a hexagonal packing of imogolite nanotubes based on grazing angle XRD patterns. Using the same technique, Mukherjee et al. (2005) proposed a monoclinic packing. Imogolite was first synthesized by Farmer et al. (1977) from a solution of monosilicic acid (H_4SiO_4) and aluminium chloride (AlCl_3). The stability, free energy and heat of formation of imogolite were studied by Farmer et al. (1979). Wada and Wada (1982) reported that the substitution of Si with Ge during the imogolite synthesis also produced imogolite type nanotubes. For this synthesis they used tetraethyl ortosilicate (TEOS) instead of monosilicic acid. In 1987, Wada reported the synthesis of imogolite at 25 °C through aging of a millimolar solution of monomeric silicic acid and polymeric hydroxylaluminium ions for 7 years. Koenderink et al. (1999) reported the synthesis of imogolite using a millimolar solution of TEOS and aluminium-sec-butoxide (ASB) instead of AlCl_3 . During the above described syntheses, the presence of a non-crystalline allophane called "proto-imogolite" as a precursor of the crystalline imogolite tubes have been postulated, a still controversial hypothesis (Mukherjee et al., 2005). Synthetic imogolite seems to have larger diameters than natural specimens or long-aged synthesized imogolite. Tamura and Kawamura (2002) calculated the stability of imogolites with different radii (given as $n = 10, 12, 14, 15, 16, 20, 24$, where n is the number of unit cells around the tube axis) and a hypothetical tubular gibbsite. The molecular dynamics simulation revealed that the minimum total energy is between tubes with $n = 14$ and $n = 16$ and that tubular gibbsite is not stable. They concluded that the orthosilicate anions stabilize the tubular structure.

The purpose of the present study is to determine if it is possible to explain the differences in the XRD patterns published so far by comparing them with calculated XRD patterns based on a rigid-body

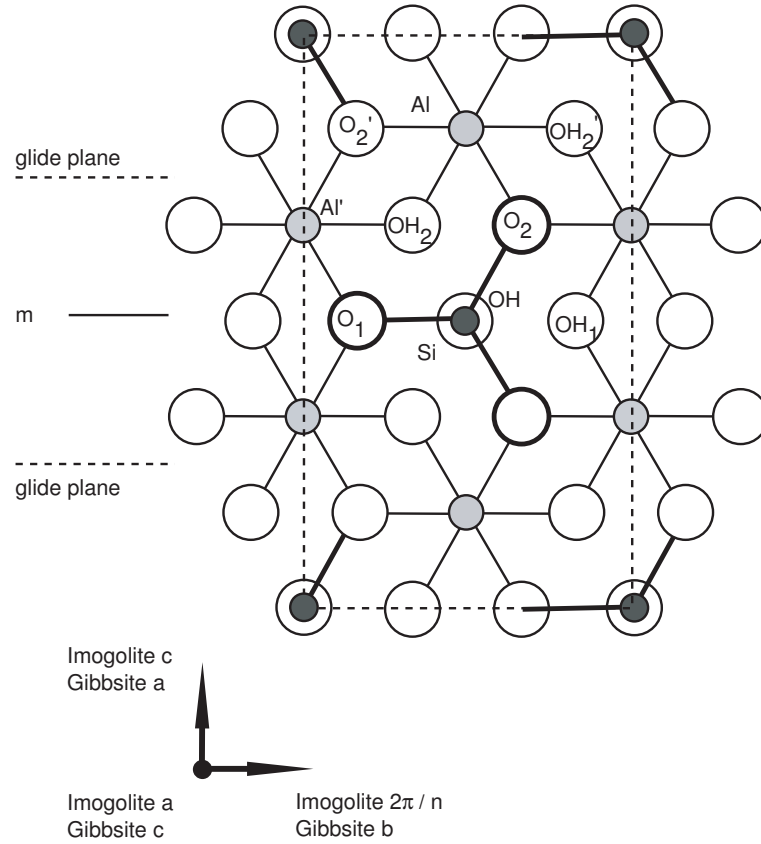


Figure 9.1: Structural model of imogolite (modified after Cradwick et al. (1972)). The imogolite a axis points downward and is parallel to the radius of the tube. The imogolite c axis is parallel the tube axis. The imogolite $2\pi/n$ axis is parallel to the gibbsite b axis. A mirror plane is present at $c/2$ and glide planes at $c/4$.

crystallographic model consisting of arrays of imogolite nanotubes. The pattern matching procedure consists of 1) creating a rigid structural model of an array of nanotubes 2) calculating XRD patterns for the different structural models and 3) comparing the calculated results with measured XRD patterns of natural and synthetic imogolite from the literature (Ohashi et al. 2004) and measured for the present work (IMOAM) and 4) refine the numerical model to fit the experimental data.

9.3 Structural Model

The structural model of imogolite nanotubes can be divided conceptually in 1) a *subcell* unit consisting of the tube itself and 2) in a *superunit* consisting of arrays of single nanotubes (bundles). Figure 9.1 depicts the structural model of a single imogolite nanotube proposed by Cradwick et al. (1972). The imogolite unit cell is constructed on the basis of a gibbsite unit cell with attached isolated orthosilicate groups rolled to form the tube. Isolated $\text{SiO}_3(\text{OH})$ groups located on the interior of the rolled gibbsite sheet share three oxygen atoms with three different AlO_6 octahedrons. The

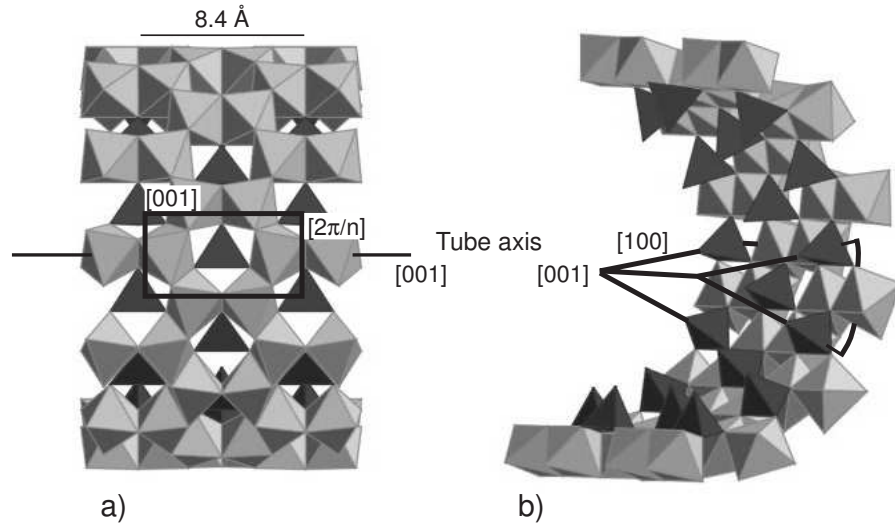


Figure 9.2: a, b, Calculated structural model of imogolite. Legend: dark tetrahedrons = orthosilicate anions; gray octahedrons = gibbsite layer; dark lines = crystallographic axis a , $2\pi/n$ and c ; bold outline = wedgelike cylindrical unit cell.

Si-OH bond points to the tube axis. Cradwick et al. (1972) presented the proposed structure in cylindrical coordinates (r, ψ, z) . The cylindrical point group is C_{2nh} . The tube axis is simultaneously a $2n$ fold screw axis with displacement of $c/2$ and a S_{2n} rotation-reflection axis, where n is the number of imogolite unit cells along the tube perimeter. The periodicity along the c axis is 8.4 \AA as inferred from TEM diffraction patterns showing regular rings at 8.4 \AA , 4.2 \AA and 2.1 \AA and indexed as (001) , (002) and (004) respectively. In order to test this structural model by confronting experimental XRD patterns with calculated XRD patterns, a new code was developed to calculate the fractional atoms coordinates of the imogolite tubes. Figure 9.2 depicts the imogolite structural model and illustrates the positions of the unit cell axes. The a -axis of the unit cell is attributed to the radius of the tube, the b -axis corresponds to the circumference and the c -axis to the tube axis. The positions of the atoms in the cylindrical unit cell (wedge like sector, see 9.2 b) are calculated taking into consideration the symmetry operations of the unit cell (i.e. a mirror plane at $c/2$). A ring with n imogolite unit cells is produced along the circumference of the tube applying the S_{2n} symmetry (see above). Finally, the resulting ring is stacked along the c direction to produce the nanotube. The dimensions of the final tube depends on 1) the number of imogolite unit cell n which will determine the radius and the circumference of the tube 2) the periodicity along the tube axis and 3) the number of units stacked along the tube axis.

The cylindrical coordinates for $n = 10$ given by Cradwick et al. (1972) served as basis for calculating coordinates for tubes with different n . The inner and outer radius of the tube depend on the number n of unit cells ($r_{int}, r_{out} = f(n)$). The cylindrical coordinates ψ are calculated using the relation $\psi_{(n')} = \psi_{(n=10)} * 10 / n'$. The rigid models have been implemented based on the cylindrical coordinates of $n = 10$ and $n = 12$ imogolites proposed by Cradwick et al. (1972). Radial coordinates r are constrained by the wall thickness which has to remain constant for all n 's. The dependence of the coordinate r on n assuming constant wall thickness can be expressed as: $r_{n'} \text{ atom} = (n' - 10) * k + r_{n=10} \text{ atom}$. The constant k was calculated based on the data published by Cradwick et al. (1972) and by Tamura and Kawamura (2002) which gave the inner and outer radii of imogolite with $n = 10$,

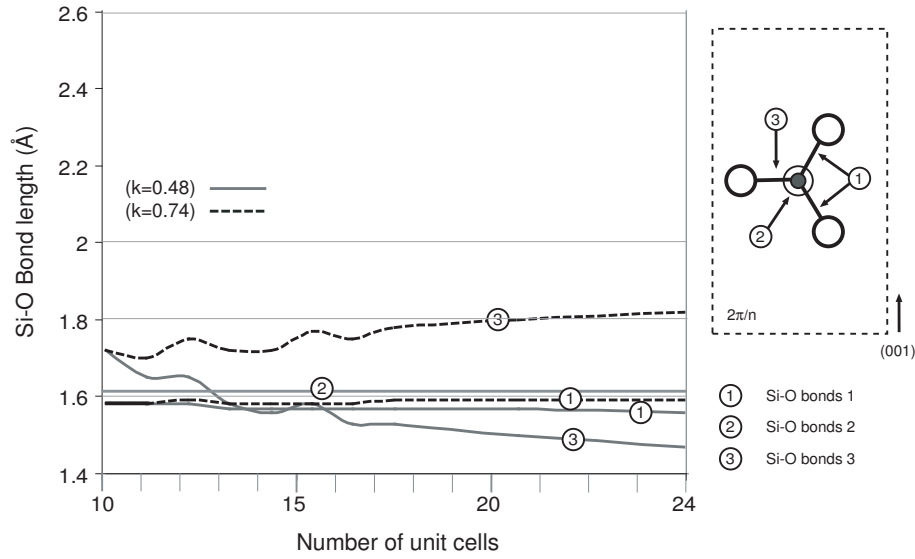


Figure 9.3: Si-O bonds length variations as function of the number n of imogolite unit cells around the tube axis. Three types of Si-O bonds are distinguished: 1) oblique to the tube axis 2) perpendicular to the tube axis 3) perpendicular to the tube axis and parallel to a .

Table 9.1: The inner and outer radii derived from molecular dynamics modelling (Tamura & Kawamura, 2002) and from the calculated rigid-body model used in this study.

	Tamura & Kawamura (2004)		$k = 0.48$		$k = 0.74$	
n	r_{ext}	r_{int}	r_{ext}	r_{int}	r_{ext}	r_{int}
10	9.5	5.1	9.1	4.8	9.1	4.8
12	10.9	6.5	10.1	5.7	10.7	6.3
14	12.5	8.1	11.0	7.0	12.1	7.8
15	13.3	8.9	11.6	7.5	12.9	8.8
16	14.3	9.9	12.0	7.7	13.6	9.2
20	16.9	12.5	14.0	9.6	16.5	12.7
24	20.3	16	15.9	11.5	19.5	15.3

12, 13, 14, 15, 16, 17, 20 and 24 based on their molecular dynamic simulations. Their simulations (2 imogolites with 6 rings along c , i.e. 4032 atoms) show that the width of the tube wall is constant with increasing n and that the radius increases linearly which corresponds to the behaviour of our model. The values of k derived from the Cradwick et al. (1972) data is 0.48 whereas the molecular dynamics data result in a value of 0.74. The variations of the Si-O bonds lengths as function of n with $k = 0.74$ and $k = 0.48$ are summarized in 9.3. The Si-OH bond (n^2 on Fig. 9.3) is constant with a value of 1.62 Å (Tamura et Kawamura, 2002), because it is independent of k . Using a value $k = 0.74$ has the consequence that the SiO_4 tetrahedra became larger with increasing n specially the Si-O₃ bond length increases to values > 1.74 Å already for values of $n = 10$. With a value of $k = 0.48$, the same bond, however, decreases with increasing n and there is a window for n -values between 11 and 16 for which all Si-O bonds have reasonable lengths. Inner and outer radii calculated from both structural models as well as the radii calculated by Tamura and Kawamura (2002) are summarized in Table 9.1.

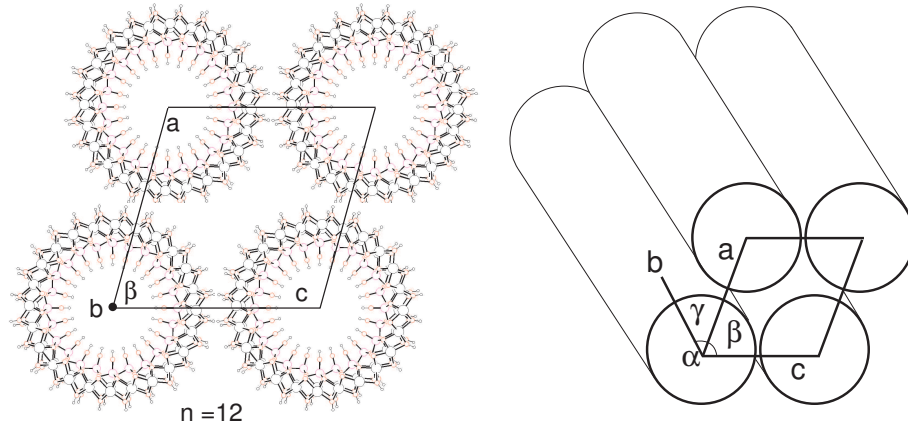


Figure 9.4: Single imogolite nanotubes are packed in bundles giving rise to a *supercell* geometry.

A *supercell* consisting of arrays of imogolite nanotubes has been constructed for XRD calculations. The stacking of single imogolite nanotubes into bundles is depicted in Fig 9.4. Bundles of nanotubes can be generated with different stacking geometries. All calculations were performed using hexagonal and monoclinic (P2/m or P1) symmetries, which have been proposed in the literature so far (Van der Gaast et al., 1985; Tamura and Kawamura., 2002; S. Mukherjee et al., 2004). The following transformation must be performed to map the tube unit cell (subcell) to the hexagonal and monoclinic systems of the supercell: $[100]_{sub} \rightarrow [100]_{sup}$, $[010]_{sub} \rightarrow [001]_{sup}$ and $[001]_{sub} \rightarrow [010]_{sup}$. In the remaining part of this study we will always refer structural parameters to the *supercell*.

9.4 Experimental

The solid synthetic imogolite sample (IMOAM) used in this study was synthesized with tetraethyl orthosilicate and $AlCl_3$ by S. Mukherjee at the Georgia Institute of Technology (for more details refer to Mukherjee et al., 2005). Two other XRD patterns used in this work were taken from the publication of Ohashi et al (2004). X-Ray diffraction on the IMOAM sample was performed using a Philips PW 1800 X-Ray diffractometer equipped with a fine-focused $CuK\alpha$ tube (40mA, 40kV). The patterns were recorded in step scan mode (0.01/step, 1s/step). Most of the previously published imogolite XRD patterns and the one measured for this study on sample IMOAM are summarized in 9.5. Although the patterns have some common features, there are significant differences to suggest the presence of different tube structures and/or stacking geometries. For the computation of XRD patterns, the PowderCell software package was used (Bundesamt für Materialforschung, Berlin). The peak model used in this study was a "pseudo-Voigt 2" function. The search for the optimum fit to the experimental data was done using a "semi-automatic" least square fitting procedure: 1) batch calculations of imogolite structures (600 structures were calculated) by systematically varying n , the lengths of the axes and the β angle of the superstructure 2) comparison of the calculated patterns with the experimental data using the fitting factor R_{wp} , R_{exp} and the 'goodness of fit' $S = R_{wp}/R_{exp}$, 3) elimination of the fits with $R_{wp}/R_{exp} > 2$ and 4) visual inspection of the best remaining fits. The peak width parameters U, V, W of the Caglioti relation in the pseudo-Voigt

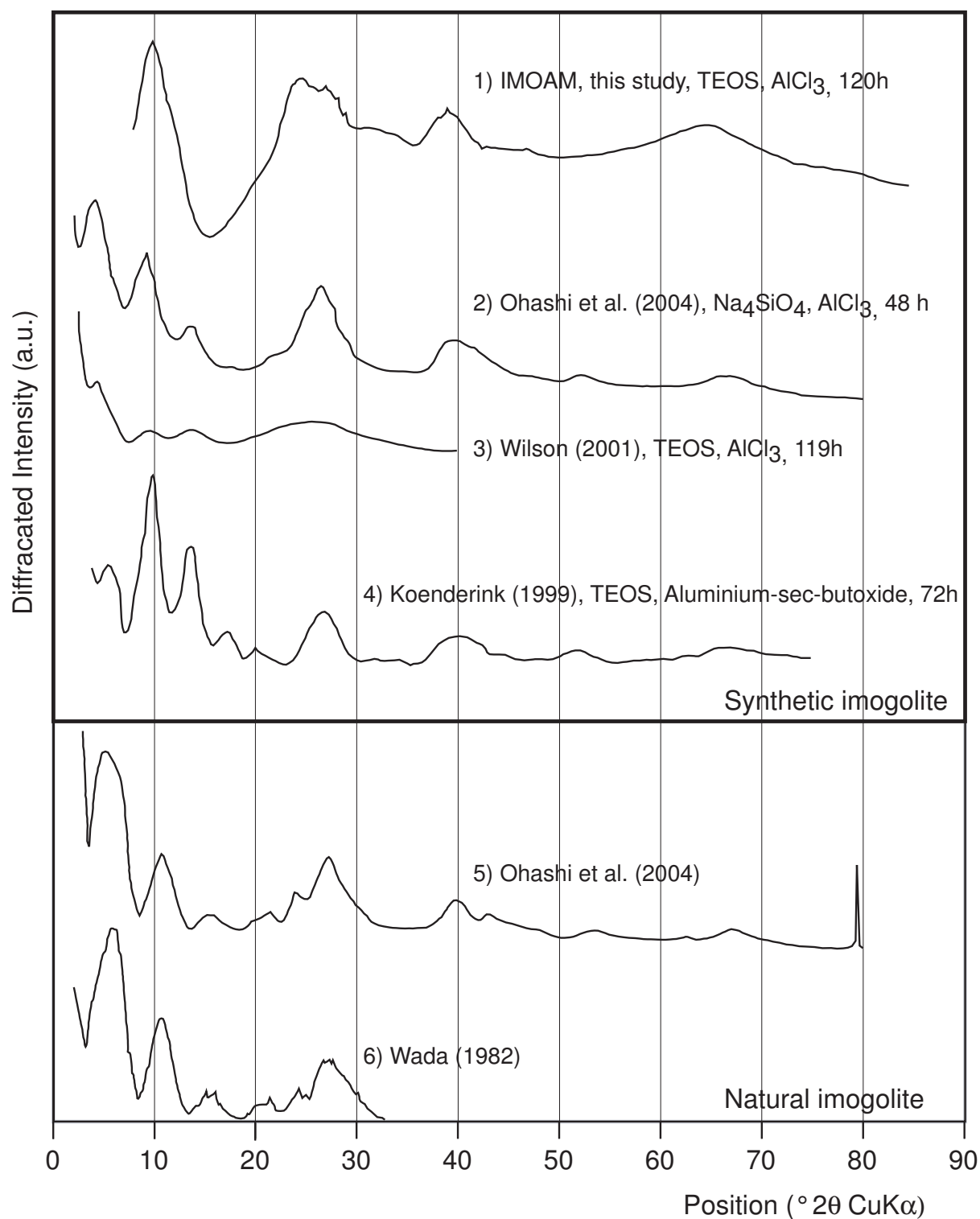


Figure 9.5: XRD spectrums of imogolite published in the literature. The reactants used for imogolite synthesis and reactions times are plotted.

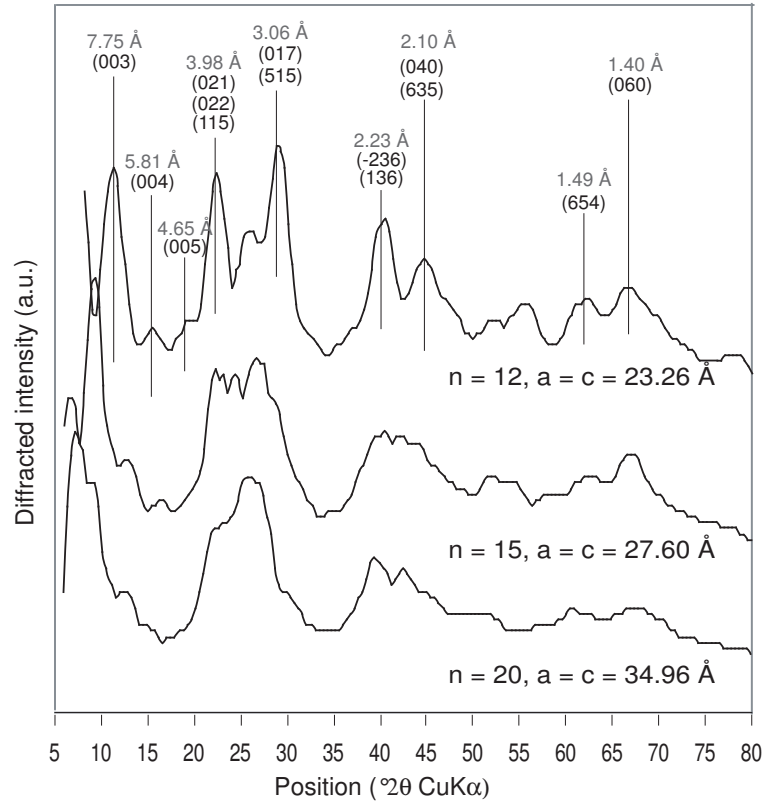


Figure 9.6: Sensitivity of simulated XRD profiles to variation in the number of imogolite unit cell n around the tube axis and to variations of the a and c axis lengths (with constant $b = 8.4 \text{ \AA}$ and $\beta = 90^\circ$).

function (Caglioti et al. 1958) were determined using the peak at $28^\circ 2\theta$ which contains the (017) and (517) reflections. These values were kept constant for all patterns and models ($U = 10$, $V = 0$, $W = 5$). A Rietveld-Toraya needle model was used with a texture along [010].

9.5 Sensitivity of calculated XRD patterns to structural parameters

A series of simulations have been performed to assess how key structural parameters influence the diffraction pattern. A stacking with monoclinic $P2_1/m$ symmetry for the imogolite bundles has been used. The monoclinic angle was varied from 90° , corresponding to a tetragonal arrangement, to 60° , corresponding to a hexagonal stacking. A decrease in the number of unit cells n around the tube axis (subcell) and a corresponding decrease of the a and c parameters of the supercell (due to the decrease in tube diameter) increases the complexity of the patterns (s. Fig. 6). b is kept constant at 8.4 \AA . On Fig. 9.6, the reflection at $11.4^\circ 2\theta$ (7.75 \AA), $15.2^\circ 2\theta$ (5.81 \AA) and $19.0^\circ 2\theta$ (4.65 \AA) can be indexed as (003), (004) and (005) respectively. The peak at $22.5^\circ 2\theta$ (3.98 \AA) is composed of three reflections e.g. (021), (022) and (115) and symmetry related planes. The peak at $29.1^\circ 2\theta$ (3.06 \AA) is mainly due to (515) and (017). The peak at $39.9^\circ 2\theta$ (2.23 \AA) consists of (-236) and (136) reflections and the one at $44.4^\circ 2\theta$ (2.1 \AA) consists of (040) and (635) reflections. The reflection

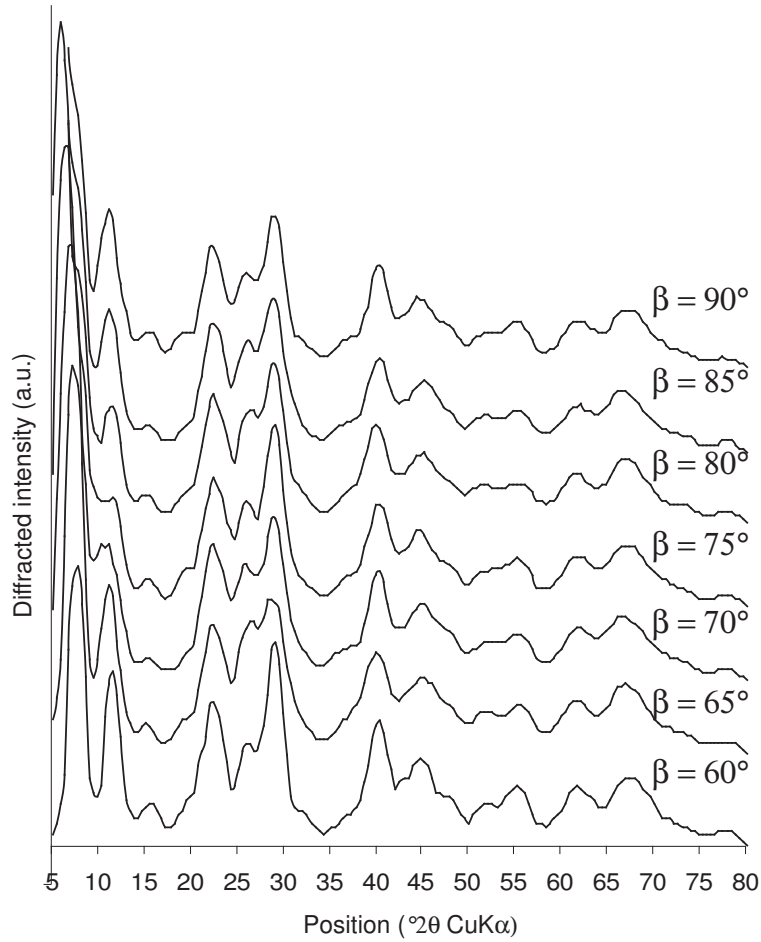


Figure 9.7: Sensitivity of simulated XRD profiles as function of the variation of the monoclinic angle β (with constant $n = 12$, $a = c = 23.5 \text{ \AA}$ and $b = 8.4 \text{ \AA}$). The variation of β does only influence the reflections at low angles ($< 15^\circ 2\theta$).

at $62.3^\circ 2\theta$ (1.49 \AA) corresponds mainly to (654). The salient features of the (0k0) reflection are located at $43^\circ 2\theta$ (2.1 \AA) for (040) and $66.8^\circ 2\theta$ (1.4 \AA) for (060). Changes in the angle β (with constant $n = 12$, $a = c = 23.5 \text{ \AA}$ and $b = 8.4 \text{ \AA}$) affect only the low angle peaks ($< 15^\circ 2\theta$) (Fig. 9.7). Increase of the b-axis length affects most high angles peaks which are shifted to smaller 2θ values (Fig. 9.8). The above observations show that there are features which allow to discriminate between the crystallographic models used for XRD fitting.

9.6 Fitting natural imogolite

The natural imogolite XRD profile published by Ohashi et al. (2004) was chosen for the fitting procedure because it shows plenty of features that are not resolved or do not appear on the other published profiles of natural imogolites (Fig. 9.5). Fitting was started with a trial structure with $n = 12$, a monoclinic angle of 90° and $b = 8.4 \text{ \AA}$. All three parameters were systematically varied

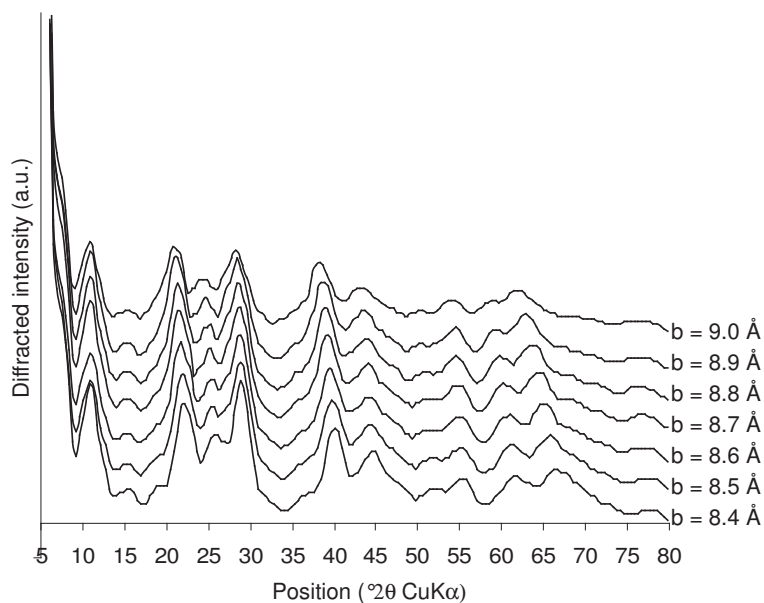


Figure 9.8: Sensitivity of simulated XRD profiles to changes in the b axis length (with constant $n = 12$, $a = c = 23.26$ Å and $\beta = 90^\circ$). The position of (060) at $67^\circ 2\theta$ is particularly sensitive to modifications of the b axis length.

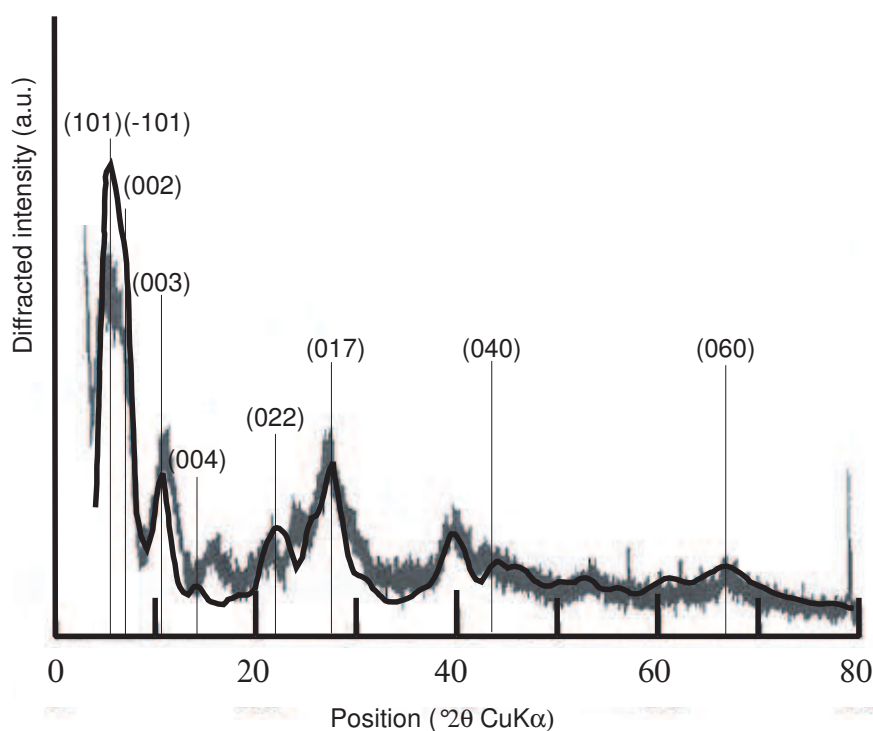


Figure 9.9: Comparison between experimental and calculated XRD patterns for natural imogolite (Ohashi et al 2004). The structural parameters are: $n = 12$, $\beta = 76^\circ$, $a = c = 24.5$ Å, $b = 8.4$ Å.

Table 9.2: Atomic coordinates and site population of natural imogolite with structural parameters used in Fig 9.9.

Atom	x/a	y/b	z/c	Population	Atom	x/a	y/b	z/c	Population
Si1	0.3216	0.5	0	1	O1	0.1281	1	0.7448	1
Si1	0.2899	1	0.0858	1	O1	0.1835	0.5	0.7712	1
Si1	0.2384	0.5	0.1657	1	O1	0.2264	1	0.8132	1
Si1	0.1707	1	0.2344	1	O1	0.2539	0.5	0.8679	1
Si1	0.0914	0.5	0.2871	1	O1	0.2641	1	0.9316	1
Si1	0.0058	1	0.3202	1	H1	0.0542	0.5	0.7758	1
O1	0.2563	0.5	0	1	H1	0.1087	1	0.7834	1
O1	0.2311	1	0.0684	1	H1	0.1558	0.5	0.8058	1
O1	0.19	0.5	0.1321	1	H1	0.1922	1	0.8415	1
O1	0.1361	1	0.1868	1	H1	0.2155	0.5	0.8879	1
O1	0.0728	0.5	0.2288	1	H1	0.2242	1	0.942	1
O1	0.0046	1	0.2552	1	O2	0.0654	1	0.6452	1
H1	0.2176	0.5	0	1	O2	0.1536	0.5	0.6518	1
H1	0.1961	1	0.058	1	O2	0.2314	1	0.6822	1
H1	0.1613	0.5	0.1121	1	O2	0.2933	0.5	0.7342	1
H1	0.1155	1	0.1585	1	O2	0.3353	1	0.8044	1
H1	0.0618	0.5	0.1942	1	O2	0.3544	0.5	0.8879	1
H1	0.0039	1	0.2166	1	O2	0.3494	1	0.979	1
O2	0.3205	0.5	0.0715	1	O3	0.3494	0.3333	0.979	1
O2	0.2698	1	0.1592	1	O3	0.0654	0.3333	0.6452	1
O2	0.2008	0.5	0.236	1	O3	0.1536	0.1667	0.6518	1
O2	0.118	1	0.2968	1	O3	0.2314	0.3333	0.6822	1
O2	0.0272	0.5	0.3373	1	O3	0.2933	0.1667	0.7342	1
O3	0.3205	0.1667	0.0715	1	O3	0.3353	0.3333	0.8044	1
O3	0.2698	0.3333	0.1592	1	O3	0.3544	0.1667	0.8879	1
O3	0.2008	0.1667	0.236	1	Al1	0.0043	0.3214	0.61	1
O3	0.118	0.3333	0.2968	1	Al1	0.1079	0.1786	0.5993	1
O3	0.0272	0.1667	0.3373	1	Al1	0.2042	0.3214	0.6159	1
Al1	0.3861	0.1786	0.0113	1	Al1	0.2865	0.1786	0.6586	1
Al1	0.345	0.3214	0.1147	1	Al1	0.3493	0.3214	0.7247	1
Al1	0.2804	0.1786	0.2102	1	Al1	0.3883	0.1786	0.8095	1
Al1	0.1967	0.3214	0.2914	1	Al1	0.4009	0.3214	0.9072	1
Al1	0.0996	0.1786	0.3527	1	O4	0.4452	0.5	0.9233	1
O4	0.4217	1	0.0397	1	O4	0.0319	0.5	0.5603	1
O4	0.3696	0.5	0.1534	1	O4	0.146	1	0.5554	1
O4	0.2922	1	0.2566	1	O4	0.2502	0.5	0.5809	1
O4	0.195	0.5	0.3424	1	O4	0.3374	1	0.6348	1
O4	0.0844	1	0.4048	1	O4	0.4015	0.5	0.7137	1
H2	0.4217	1	0.0397	1	O4	0.438	1	0.8121	1
H2	0.3696	0.5	0.1534	1	H2	0.4452	0.5	0.9233	1
H2	0.2922	1	0.2566	1	H2	0.0319	0.5	0.5603	1
H2	0.195	0.5	0.3424	1	H2	0.146	1	0.5554	1
H2	0.0844	1	0.4048	1	H2	0.2502	0.5	0.5809	1
O5	0.4153	0.3012	0.0583	1	H2	0.3374	1	0.6348	1
O5	0.3588	0.1988	0.1708	1	H2	0.4015	0.5	0.7137	1
O5	0.2778	0.3012	0.2717	1	H2	0.4383	1	0.8121	1
O5	0.178	0.1988	0.3541	1	O5	0.0505	0.1988	0.5575	1
O5	0.066	0.3012	0.4123	1	O5	0.1636	0.3012	0.5575	1
H3	0.4153	0.3012	0.0583	1	O5	0.2655	0.1988	0.5877	1
H3	0.3588	0.1988	0.1708	1	O5	0.3493	0.3012	0.6459	1
H3	0.2778	0.3012	0.2717	1	O5	0.4093	0.1988	0.7283	1
H3	0.178	0.1988	0.3541	1	O5	0.4414	0.3012	0.8292	1
H3	0.066	0.3012	0.4123	1	O5	0.4434	0.1988	0.9417	1
Si1	0.0802	0.5	0.6685	1	H3	0.0505	0.1988	0.5575	1
Si1	0.1607	1	0.6798	1	H3	0.1636	0.3012	0.5575	1
Si1	0.2303	0.5	0.7129	1	H3	0.2655	0.1988	0.5877	1
Si1	0.2841	1	0.7656	1	H3	0.3493	0.3012	0.6459	1
Si1	0.3186	0.5	0.8343	1	H3	0.4093	0.1988	0.7283	1
Si1	0.3314	1	0.9142	1	H3	0.4414	0.3012	0.8292	1
O1	0.0639	0.5	0.7358	1	H3	0.4434	0.1988	0.9417	1

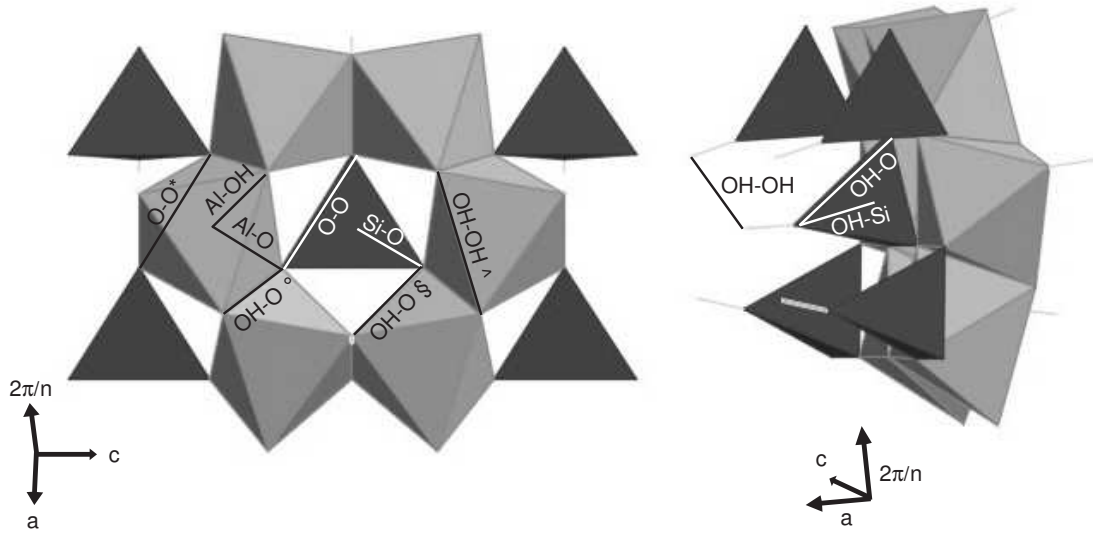


Figure 9.10: Interatomic distances in imogolite. Legend: gray lines = interatomic distances in tetrahedral layer; black lines = interatomic distances in rolled gibbsite layer.

and the patterns were compared with the measured profile according to the procedure described above. The best fit was obtained for $n = 12$ corresponding to $a = c = 24.5 \text{ \AA}$, $b = 8.4 \text{ \AA}$ and $\beta = 76^\circ$ (Fig. 9.9). The fractional atomic coordinates of the asymmetric unit corresponding to this best-fitting structure are listed in Table 9.5. The resulting bond distances for selected atom pairs are summarized Table 9.3. These distances are consistent with Si-O, Al-O, O-O, O-OH distances commonly observed in aluminosilicates and are depicted in Fig. 9.10. Although the fit to the experimental data for this trial structure is not perfect, the main features of the diffraction pattern are fairly well reproduced by the simulation. The major discrepancies are the large difference in the intensity of the (002) peak and in the region around $16^\circ 2\theta$ and between 21° and $23^\circ 2\theta$.

9.7 Fitting synthetic imogolite

We selected the synthetic imogolite XRD profile published by Ohashi et al. (2004) (n° 2 on Fig. 9.5) and a pattern of the IMOAM sample (n° 1 on Fig. 9.5). As observed on Fig. 9.5, synthetic imogolites show a slight displacement of the (060) reflection toward higher d-spacings compare to natural imogolite. This can be simulated by increasing the b-axis length, which has only very small effect on the low-angle reflections as discussed before. The synthetic imogolite of Ohashi et al. (2004) shows characteristic diffraction peaks at $d = 20.0 \text{ \AA}$, 9.5 \AA , 6.5 \AA and 3.3 \AA . The first two peaks were attributed by Ohashi et al. to (010) and (020) which corresponds to (001) and (002) in the setting used in the present investigation. These main features can be fairly well reproduced with the following model parameters: $n = 15$, $\beta = 85^\circ$, $a = c = 30 \text{ \AA}$, $b = 8.4 \text{ \AA}$ (Fig. 9.11). The higher value of n relative to the natural imogolite is expressed by the position of the maxima centred at the position of the (001) reflection, for example (003), which are shifted to lower angles, and the condensation of the three peaks between $20\text{-}30^\circ 2\theta$ in natural imogolite to two peaks or

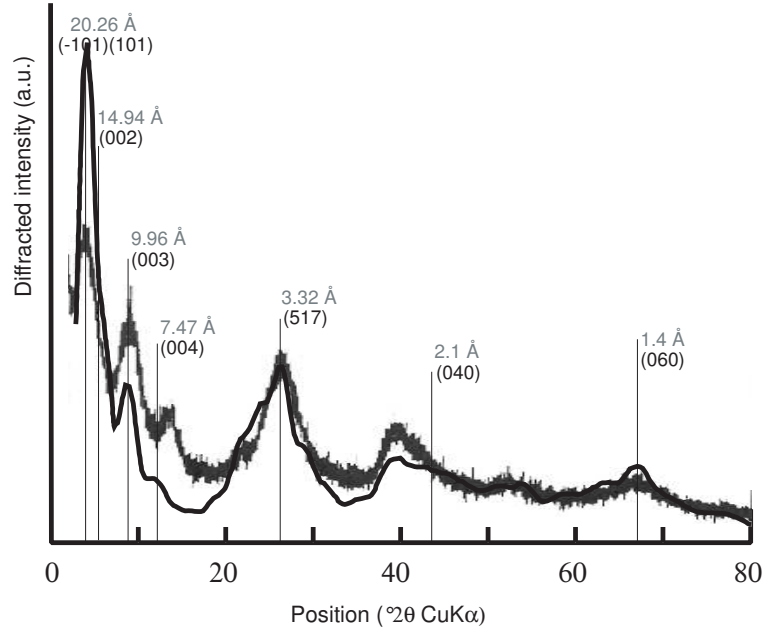


Figure 9.11: Comparison between experimental and calculated XRD patterns for synthetic imogolite (Ohashi et al. 2004). The structural parameters are: $n = 15$, $\beta = 85^\circ$, $a = c = 30 \text{ \AA}$, $b = 8.4 \text{ \AA}$.

even a single one. The loss of resolution may, however, also be explained by a mixture of imogolites with different n 's and packing schemes.

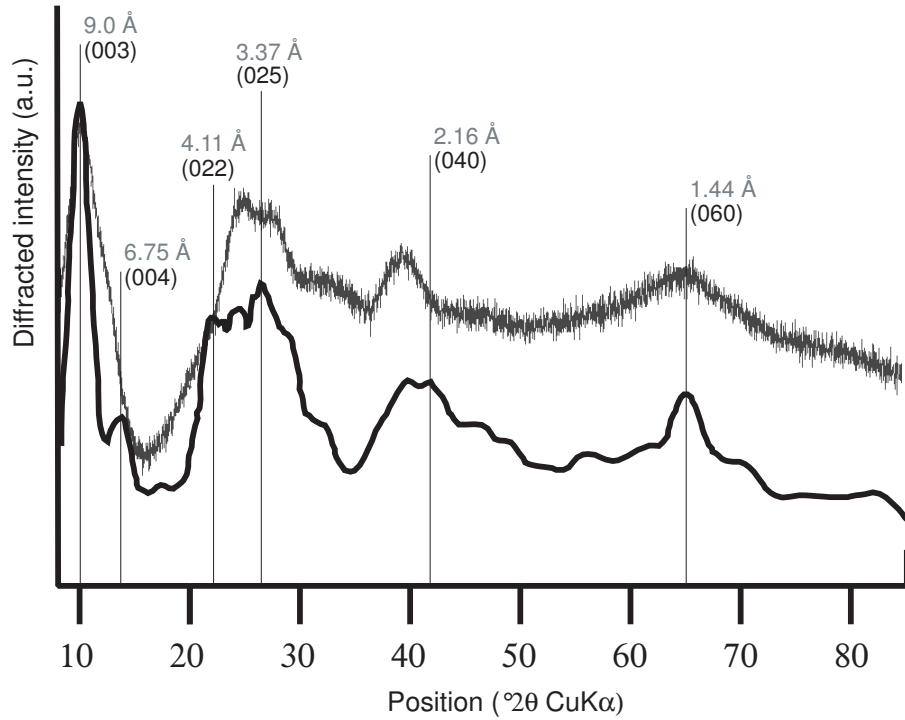
The IMOAM powder sample is best modelled with: $n = 14$, $a = c = 27 \text{ \AA}$, $b = 8.64 \text{ \AA}$, $\beta = 90^\circ$ (Fig. 9.12). No structure with n different of 14 could satisfactory fit the measured XRD patterns. The group of three peaks between $20\text{--}30^\circ 2\theta$ are not very well resolved. The position of the maxima of the peak centred at the position of the (060) reflection is shifted to lower 2θ values compared to the previous sample, which may indicate a larger b -axis parameter e.g. around 8.64 \AA instead of 8.4 \AA as in the natural imogolite. Like natural imogolite and Ohashi imogolite, the strongest (0 k 0) reflections are (060) and (040), whereas (020) is weak. The (001) intensities have the reverse behaviour. They are important for the (003) and (004) planes but decrease sharply for $l > 4$. Similar to observations on TEM diffraction patterns (Mukherjee et al. 2005), the strongest (031) XRD intensity corresponding to (036). This is also the case for natural imogolite (see above and Cradwick et al., 1972).

9.8 Simulation of the low angle region (4-13 2θ CuK α). The bundle geometry.

Based on small angle XRD diffraction, van der Gaast et al. (1985) proposed a hexagonal packing model, e.g. $\beta = 60^\circ$, for bundles of synthetic imogolite nanotubes. Based on grazing angle incidence XRD patterns Mukherjee et al. (2005) suggested a monoclinic packing with a monoclinic angle $\beta = 78^\circ$. The simulations presented in Fig. 9.13 show the influence of the packing geometry on the peaks in the region between 4 and $13^\circ 2\theta$. The single reflection containing (-101) and (101) for a 2θ

Table 9.3: Interatomic spacing (\AA) in in Tubes of C24h symmetry.

	Atoms	\AA	\AA	\AA
SiO ₄ H	Si-OH	1.62		
	Si-O	1.74	1.57	1.57
	O-O	2.76	2.62	2.62
	O-OH	2.62	2.61	2.61
	OH-OH	3.25		
Gibbsite sheet	Al-O	1.85	1.9	1.99
	Al-OH	1.81	1.93	1.94
	O-O	2.6	2.6	2.76
	OH-OH	2.53	2.85	2.9
	OH-OH	3.29	3.6	3.61
	O-OH	2.52	2.52	2.58
	O-OH	2.78	2.8	2.82

Figure 9.12: Comparison between experimental and calculated XRD patterns for synthetic imogolite. The structural parameters are: $n = 14$, $a = c = 27 \text{ \AA}$, $b = 8.64 \text{ \AA}$, $\beta = 90^\circ$.

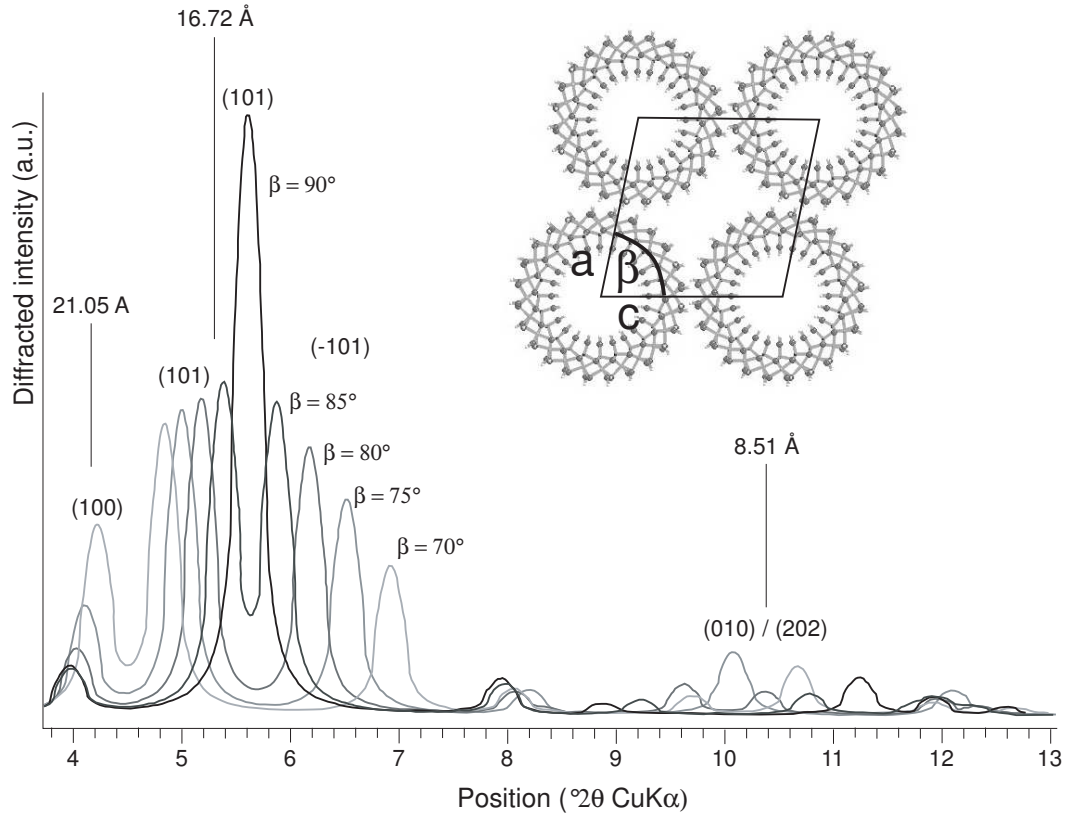


Figure 9.13: Variation of the XRD pattern as function of the monoclinic angle β at low 2θ angles. The monoclinic solid state packing model for bundles imogolite nanotubes is depicted upper right. Legend: vertical lines = positions of the XRD reflections measured by Mukherjee et al (2005) from imogolite in monoclinic state packing.

angle = 90° , splits into two reflections, for 2θ angle $< 90^\circ$, the individual reflections are displaced in opposite directions, the (-101) position to higher and the (101) position to lower angles. The splitting, however, is too small relative to the peak widths in the measured patterns. It is therefore very difficult to assess the correct stacking geometry. If one considers the overall fits, simulation with monoclinic angles between 70° and 80° for the natural samples and an angle of 90° for the synthetic samples give the best results.

9.9 Discussion

In the light of the present simulations, we can interpret the differences between the published imogolite XRD spectra (s. Fig. 5) as the result of different tube diameters, but probably also different packing geometries. The patterns from Wada (1982) and Ohashi et al. (2004) for natural imogolites are very similar and can be modelled with tubes consisting of 12 imogolite unit cells around the tube axis and the supercell geometry is best modelled with monoclinic bundles. These natural imogolites have a b-axis parameter of 8.4 Å. The only major peak at $14.6^\circ 2\theta$ not accounted for by the simulation is probably due to the presence of boehmite. Boehmite has been observed

in synthesis runs with excess aluminium (Wada et al. 1979). The XRD patterns for the various synthetic imogolites are more variable and the peaks less well defined. It is, however, evident that the value of n must be larger than for the natural samples, e.g. n is between 14 and 15. The packing may also be different e.g. instead of monoclinic, the packing would rather be quadratic with $\beta = 90^\circ$, which is in contrast with hexagonal stacking proposed by van der Gaast et al. (1985). A longer b -axis is also likely. Reasons for the differences between natural and synthetic imogolites may be found in the chemical composition or in the formation conditions. Despite of the different starting materials used by Ohashi and Koenderink the product imogolites present very similar XRD patterns raising doubts that the differences in imogolite structures is only due to the chemical products and routes used for their synthesis. For example, the IMOAM and the imogolite prepared by Wilson et al. (2001) samples were both synthesized using tetraethoxysilane and aluminium chloride and during similar reactions times (119 and 120 hours) but show slightly different XRD patterns. On the other hand, the difference between natural and synthetic imogolite structure may probably be explained by the difference in "synthesis" parameters and time. The tube diameter of imogolite nanotubes, which were synthesized in long duration runs, is smaller diameters than for short duration syntheses. Natural imogolites can also be considered "very long duration" reaction products, and have, therefore, the smallest tube diameters of all imogolite samples analysed so far.

9.10 Conclusions

A new code has been developed that allow batch calculations of the imogolite structure proposed by Cradwick et al. (1974). The calculated XRD patterns are in good agreement with the experimental data, all the features of the XRD patterns recorded on imogolite could be modelled. Natural imogolite is best simulated with 12 unit cells around the tube axis. Synthetic imogolite is best simulated with 14-15 unit cells around the tube. The sensitivity of the XRD pattern to the parameters $\langle n, a, b, c, \beta \rangle$ shows that the region $< 15^\circ 2\theta$ ($> 5.9 \text{ \AA}$) is particularly sensitive to changes in the angle β . The shape and positions of the reflections with angles ranging from $15^\circ 2\theta$ to $50^\circ 2\theta$ are particularly sensitive to the parameter n . The $[100]$, $[010]$, $[001]$ lengths have an influence on the whole spectrum. The monoclinic symmetry proposed for Al-Si nanotubes postulated by Mukherjee et al. (2005) is confirmed by the XRD calculations.

9.11 Acknowledgements

M. Poffet at the University of Fribourg for her help in chemical synthesis of synthetic imogolite. M.S. Mukherjee and S. Nair at the Georgia Institute of Technology for their synthetic imogolite sample and useful communications. K. Kawamura at Tokyo Institute of Technology for having kindly delivered his molecular dynamic code.

9.12 References

- Caglioti G., Paoletti A. & Ricci F.P. (1958): Choice of collimators for a crystal spectrometer for neutron diffraction. *Nucl. Instrum. Methods*, 35, 223-228.
- Cradwick P.D.G., Farmer V.C., Russell J.D., Masson C.R., Wada K. & Yoshinaga N. (1972): Imogolite, a hydrated aluminium silicate of tubular structure. *Nature*, 240, 187-189.
- Farmer V., Fraser A.R. & Tait J.M. (1977): Synthesis of imogolite: A tubular aluminium silicate polymer. *J.C.S. Chem. Comm.*, 462-463.
- Farmer V.C., Smith B.F.L. & Tait J.M. (1979): The stability, free energy and heat of formation of imogolite. *Clays Minerals*, 14, 103-107.
- Gense C. (1973): Conditions de formation de l'imogolite dans les produits d'altération de roches volcaniques basiques de l'île de la Réunion. *Bull. Groupe. Franc. Argiles*, 79, 79-83.
- Henmi T. & Wada K. (1976): Morphology and composition of allophane. *Am. Mineral.*, 61, 379-390.
- Koenderink G.H., Kluijtmans S.G.J.M. & Philipse A.P. (1999): Note on the synthesis of colloidal imogolite fibers. *J. of Colloid and Interface Sc.*, 216, 429-431.
- Lulli L., Bidini D., Dabin B. & Quantin P. (1983): Etude de deux sols andiques dérivés de roches volcaniques d'Italie du Sud (Mont Roccamonfina et Vulture) à caractère cryptopodzolique. *Cah. O.R.S.T.O.M., sér. Pédol.*, 20, 27-44.
- Mukherjee S., Bartlow V.M. & Nair S. (2005): Phenomenology of the growth of single-walled aluminosilicate and aluminogermanate nanotubes of precise dimensions. *Chem. Matter.*, 17, 4900-4909.
- Ohashi F., Tomura S., Akaku K., Hayashi S. & Wada S.I. (2004) : Characterization of synthetic imogolite nanotubes as gas storage. *J. of Material Sc.*, 39, 1799-1801.
- Russell J.D., McHardy W.J. & Fraser A.R. (1969): Imogolite: A unique aluminosilicate, *Clay Min.*, 8, 87-99.
- Tamura K. & Kawamura K. (2002): Molecular dynamics modelling of tubular aluminium silicate: Imogolite. *J. Phys. Chem. B.*, 106, 271-278.
- Van der Gaast S.J., Wada K., Wada S.I. & Kakuto Y. (1985): Small-angle X-Ray powder diffraction, morphology, and structure of allophane and imogolite. *Clays Clay Miner.*, 33, 237-243.
- Vainshtein B.K., (1966): Diffraction of X-Rays by Chain Molecules. Elsevier Publ. Co.
- Wada K., (1967): A structural scheme of soil allophane. *Am. Mineral.*, 52, 690-708.
- Wada K. & Yoshinaga N. (1969): The structure of imogolite. *Am. Mineral.*, 54, 50-56.
- Wada K., Yoshinaga N., Yotsumoto H., Ibe K. & Aida S. (1970): High resolution electron micro-

graphs of imogolite. *Clay Min.*, 8, 487-489.

Wada S.I., Eto A. & Wada K. (1979): Synthetic allophane and imogolite. *J. Soil Sci.*, 30, 347-355.

Wada S & Wada K. (1982): Effects of Substitution of Germanium for Silicon in Imogolite. *Clays Clay Miner.*, 30, 123-128.

Wada S. (1987): Imogolite Synthesis at 25. *Clays Clay Miner.*, 35, 379-384.

Wilson M.A., Lee G.S.H. & Taylor R.C. (2001): Tetrahedral rehydration during imogolite formation. *J. of Non-Crystalline Solids*, 296, 172-181.

Yoshinaga N. & Aomine S. (1962): Imogolite in some ando soils. *Soil Sci. Plant Nutr.*, 8, 114-121.

Chapter 10

Conclusions and outlook

Three kind of nanotubes were studied, namely chrysotile, tellurium and imogolite nanotubes. Different techniques and apparatus ranging from TEM, SEM, XRD, HT-XRD, EDS, IR-spectrometry, porosimetry, magnetic induction furnace and high pressure piston cylinder were used for characterization, synthesis and evaluation of the potential applications of these materials.

8 samples of natural chrysotile nanotubes were studied from the point of view of thermal stability. The results of these thermal stability studies were used for the dimensioning of injection experiments of liquid metals under high pressure conditions (4-10 Kbar) in order to manufacture metallic nanowires. Hg and Pb nanowires were successfully produced through this method but others metals with melting temperature below $< 700^{\circ}\text{C}$ such as Al, Zn, Ga, In, Se, etc. may also be suitable for injection experiments. Injection of Cu, with a melting temperature well above the 700°C stability limit, was unsuccessful as well as injections of Sn. Characterization of the metallic nanowires through transmission electron microscopy remains a challenge because of the fast moving metal melt inside the tube and beam damages on chrysotile.

In a second case study, tellurium nanotubes were synthesized through physical vapor deposition (PVD) (between 150°C and 200°C) in an induction magnetic furnace. The nanotubes show an hexagonal symmetry and a preferred orientation relative to the silicon wafer (used as target). The (001) plane of the tellurium nanotubes are parallel to the (111) surface of the silicon wafer. The PVD method allows synthesis of tellurium nanotubes and nanowires without the use of template nor catalyst. The growth of the nanotubes is thought to proceed by a nucleation and growth process. No nanotubes were produce in vacuum without magnetic induction.

In the third case study, imogolite nanotubes synthesized via a mild chemistry route using TEOS and AlCl_3 have been analyzed using X-rays diffraction. A rigid-body crystallographic model of the tubular and 'bundle' structures has been computed. XRD calculations were performed based on the rigid-body model and compared with experimental data. The structural model proposed by Cradwick et al. (1972) is confirmed and a monoclinic geometry for the bundle is proposed. These results are in agreement with the experimental data of Mukherjee et al (2005). Natural imogolite is shown to have 12 unit cells around the tube axis and synthetic imogolite is shown to have 14-15 unit cells around the tube axis.

Appendix A

XRD patterns on chrysotile nanotubes

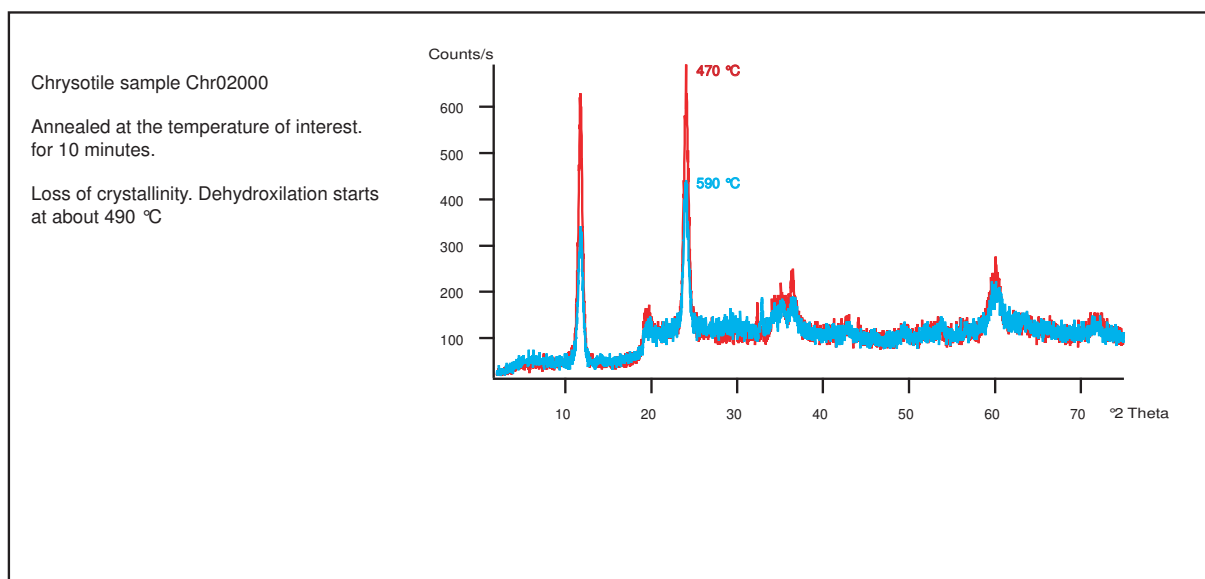
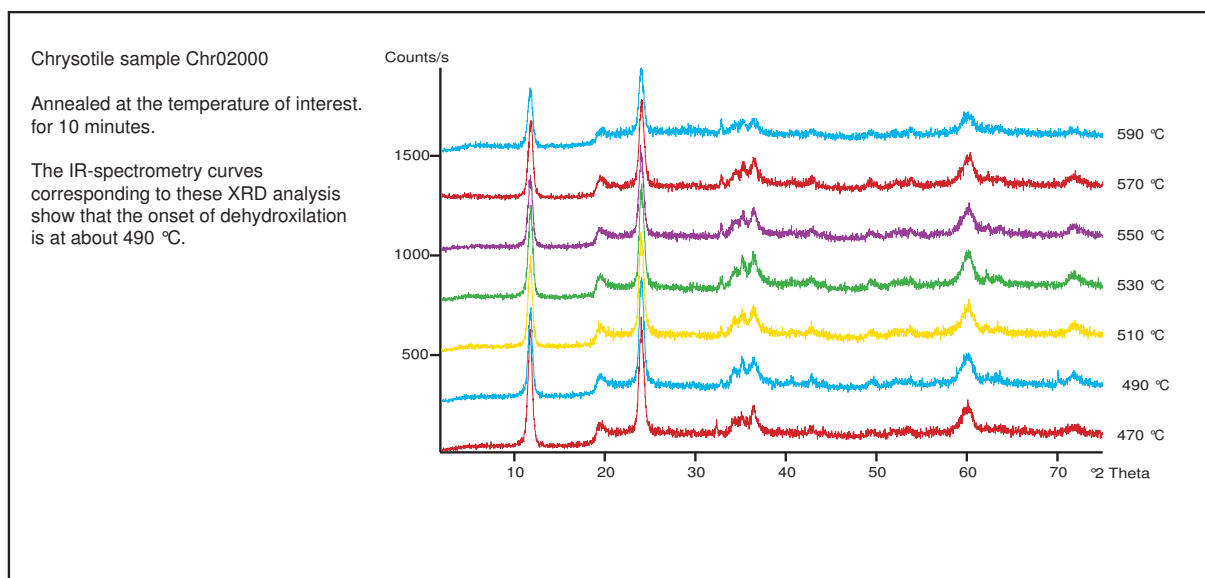
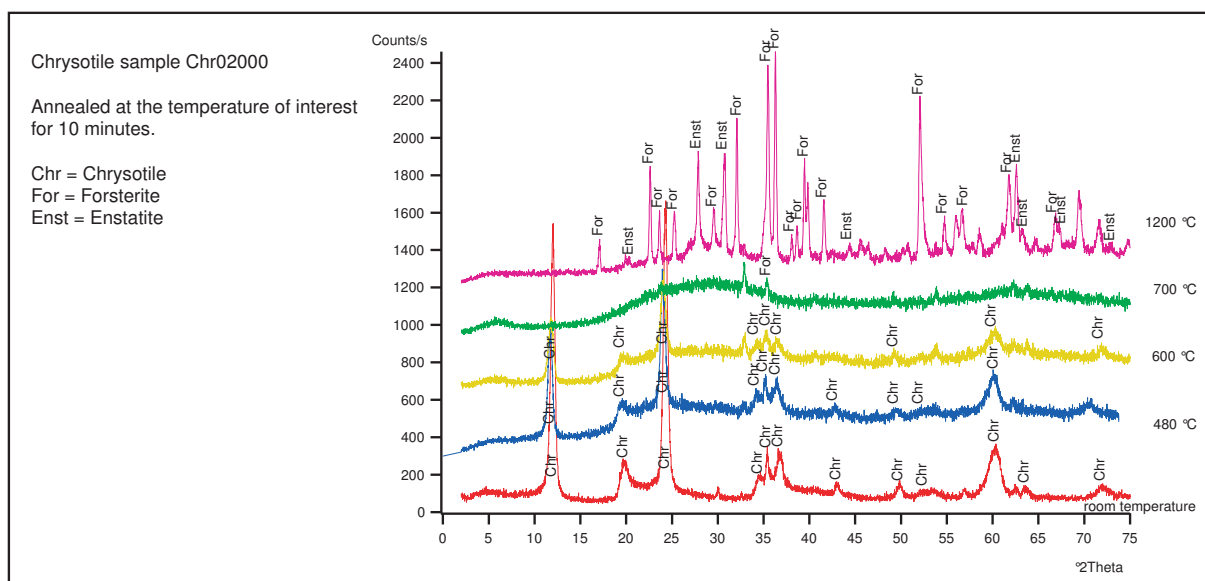


Figure A.1:

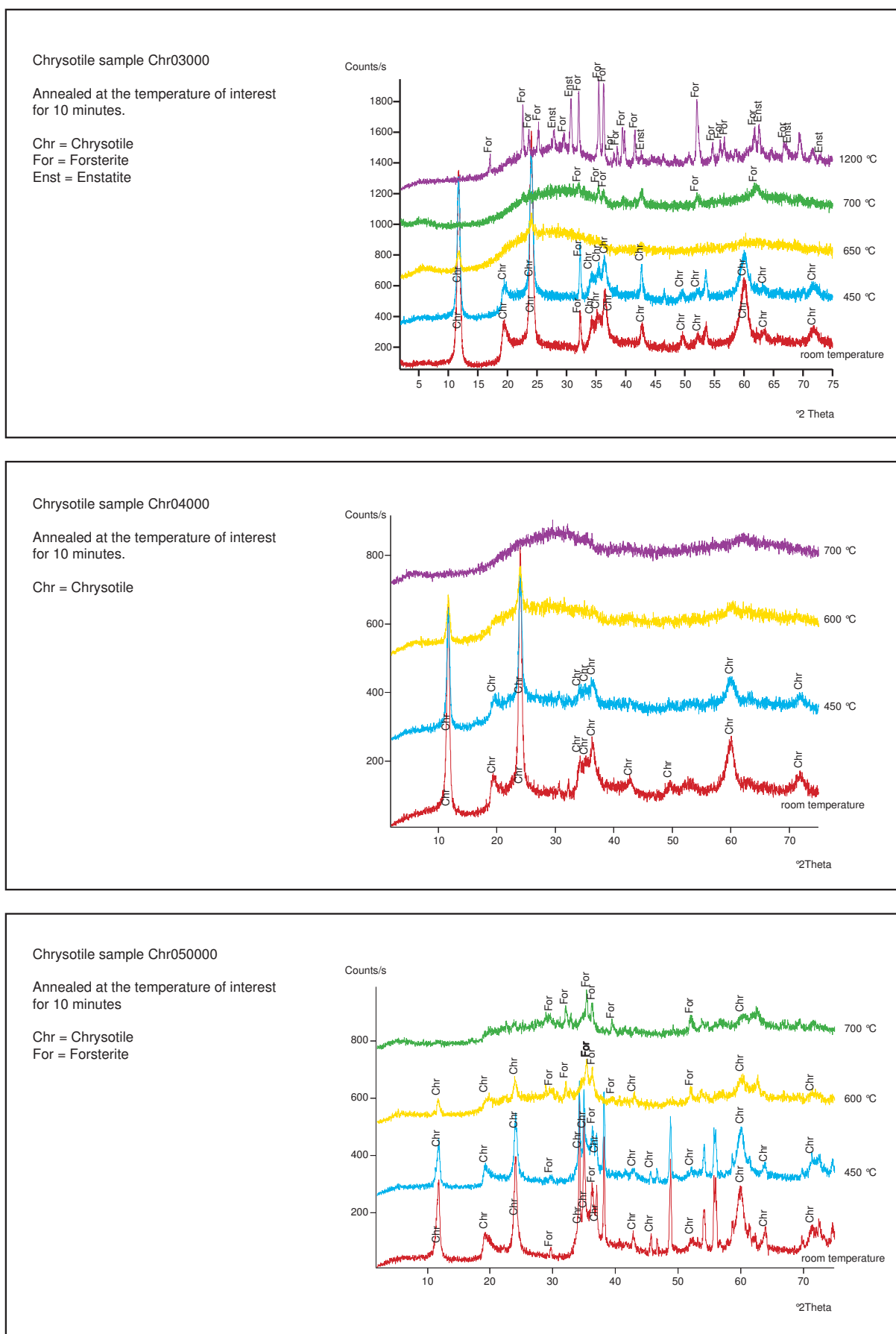


Figure A.2:

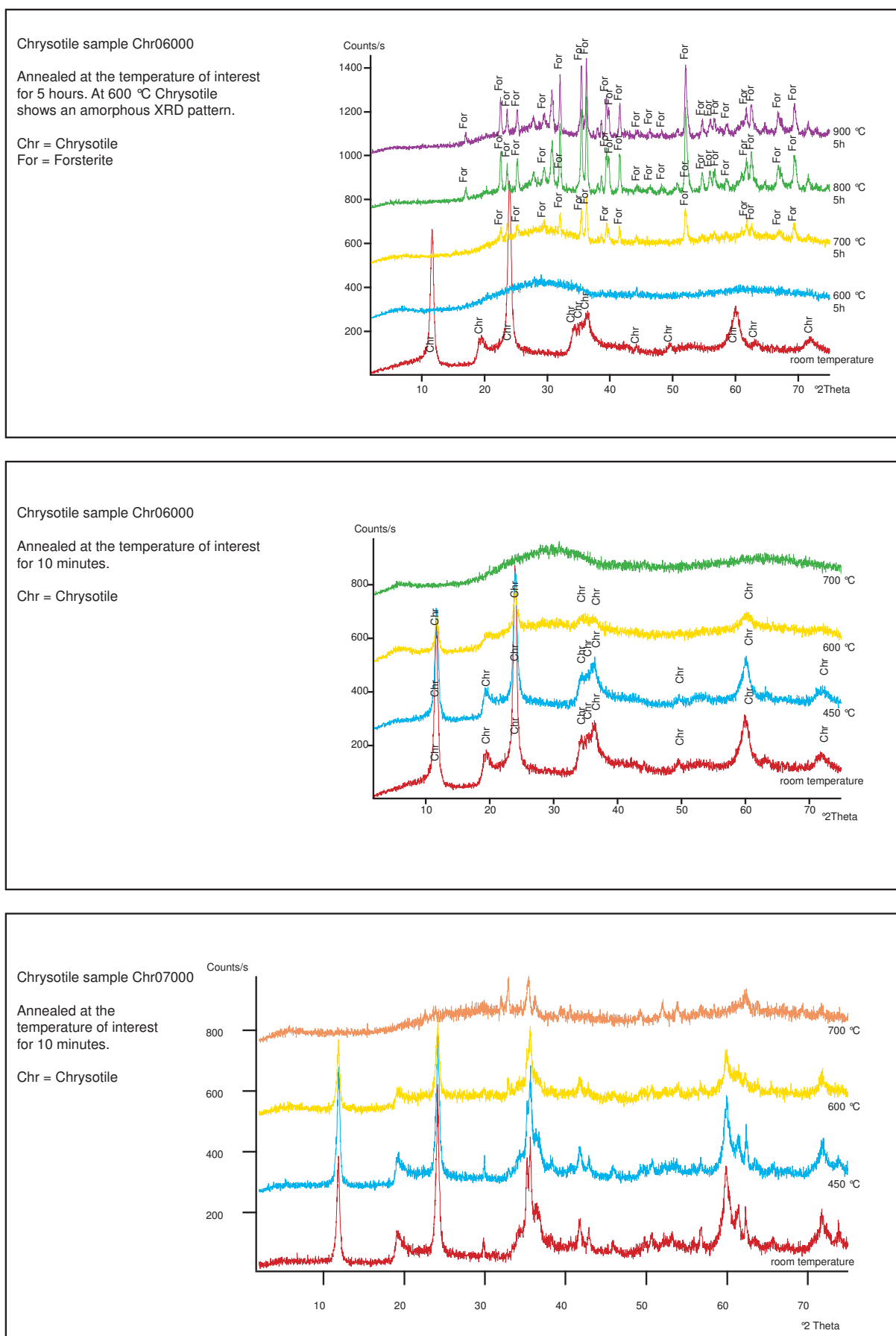


Figure A.3:

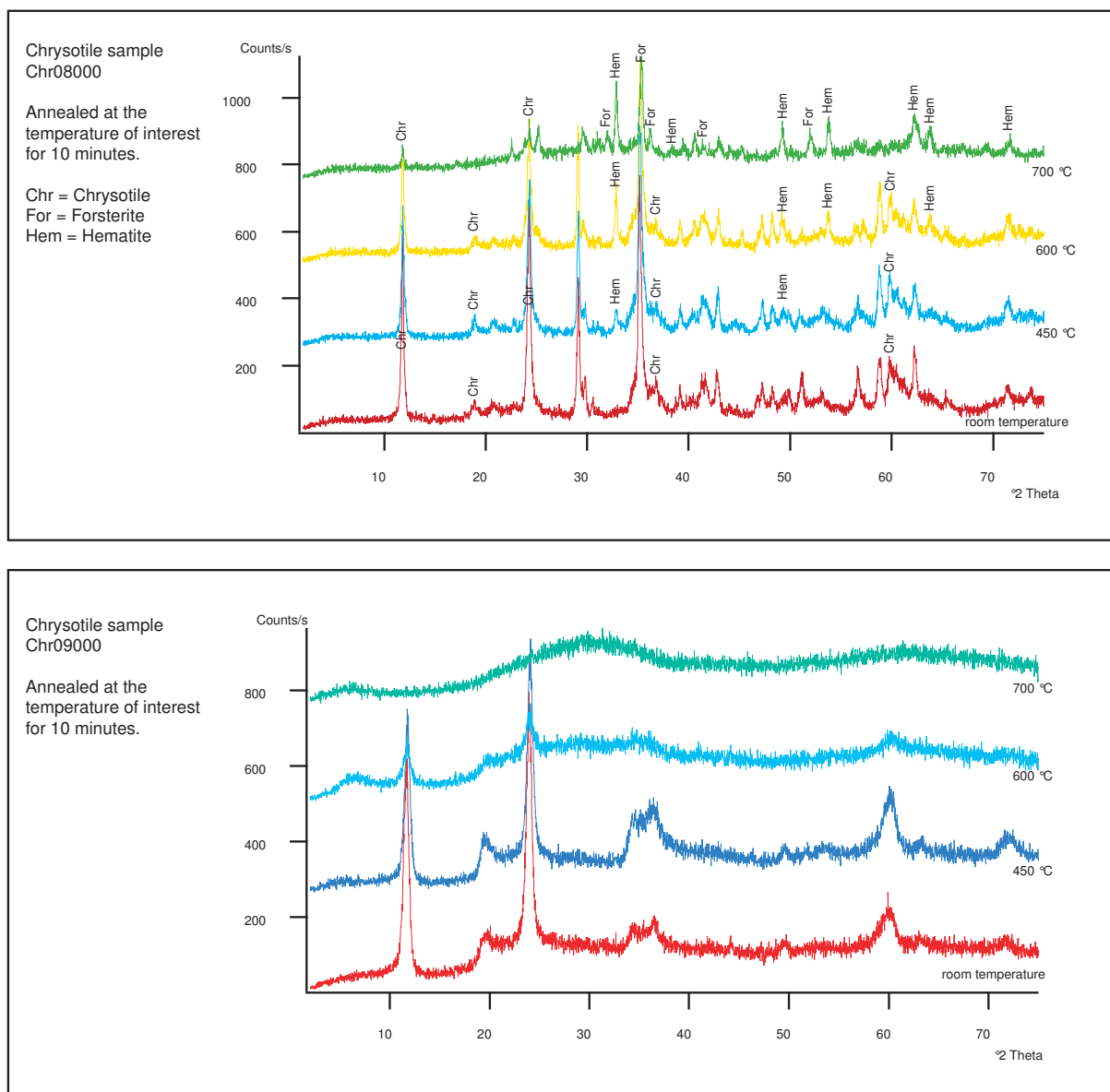


Figure A.4:

Appendix B

IR spectrometry on chrysotile

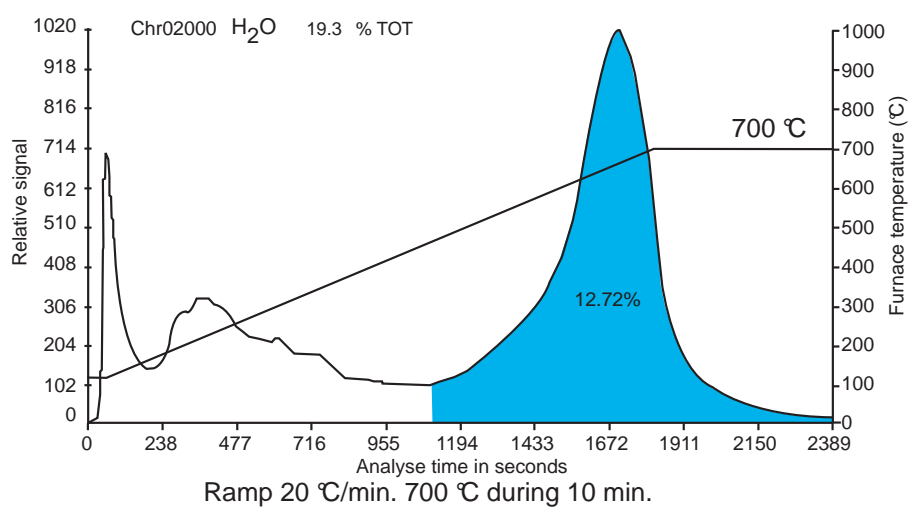
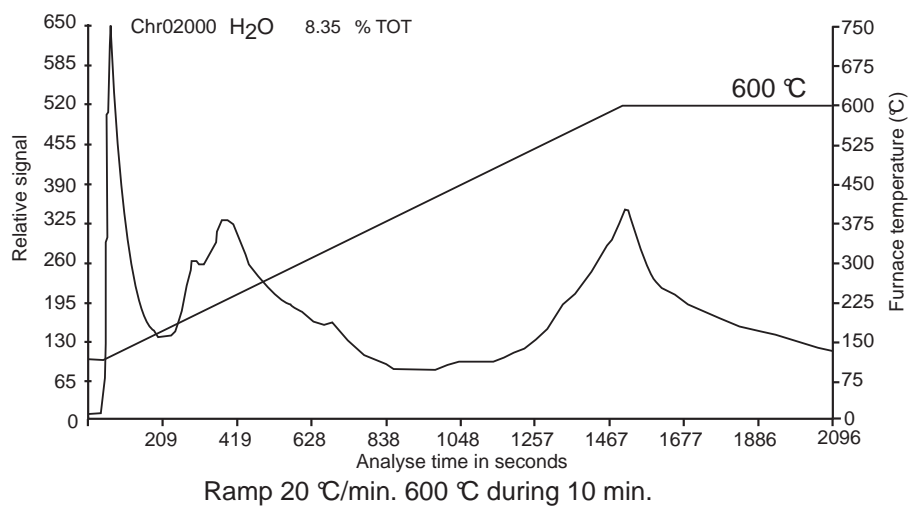
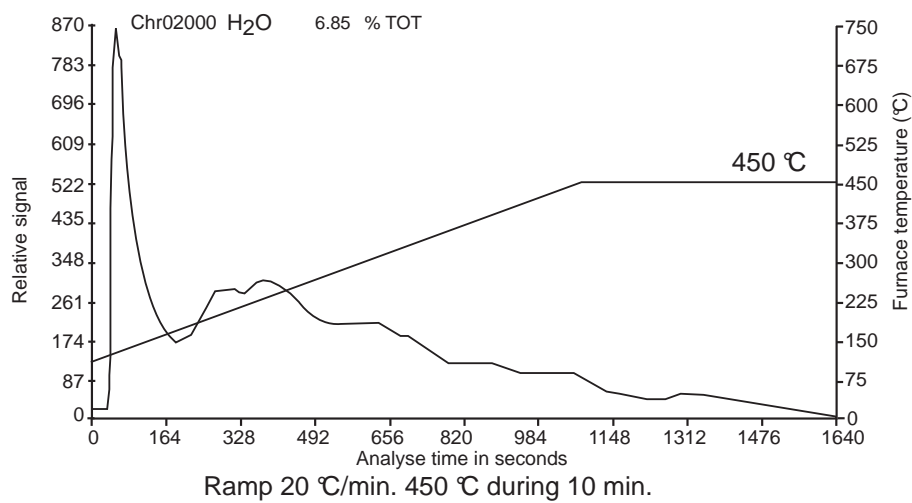


Figure B.1:

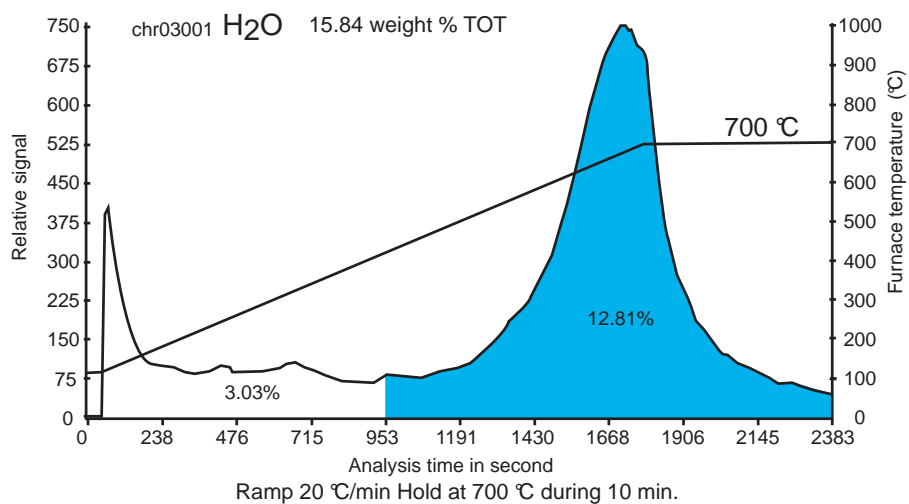
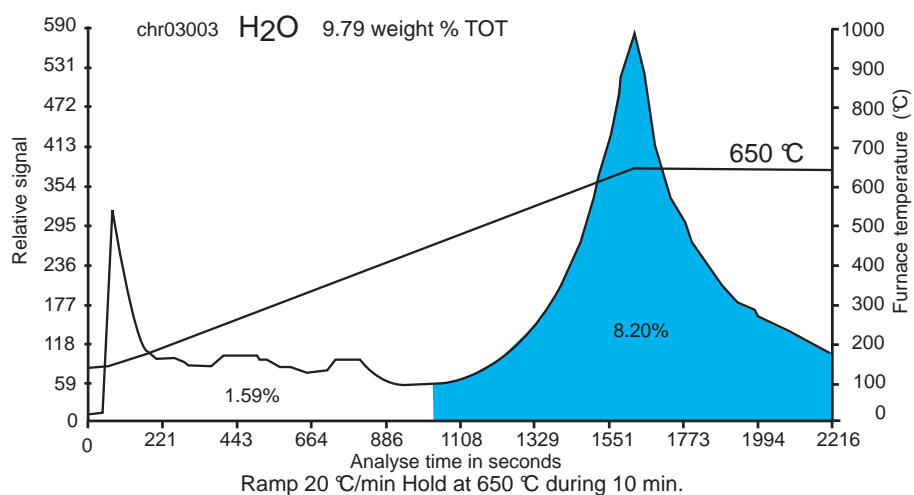
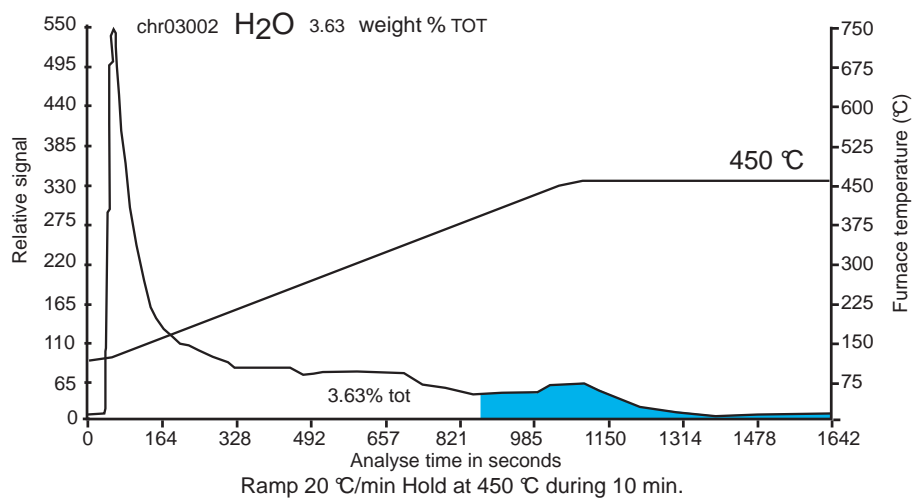


Figure B.2:

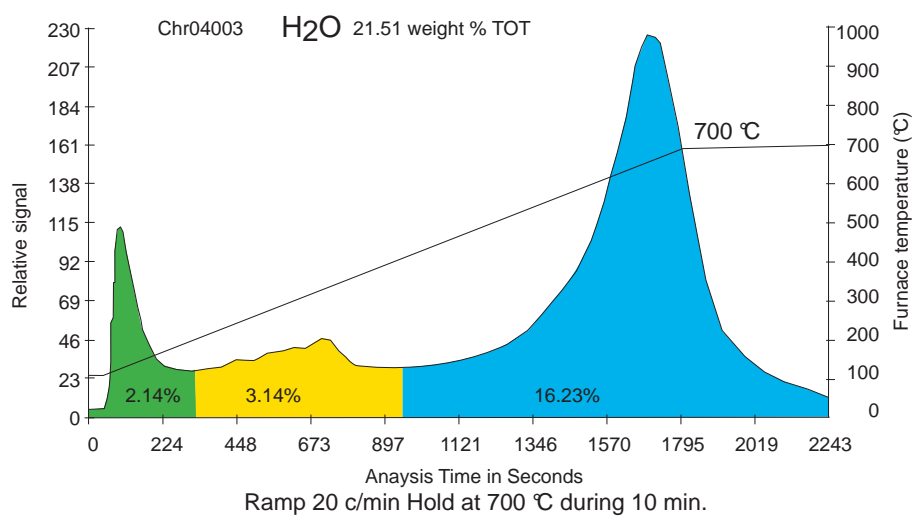
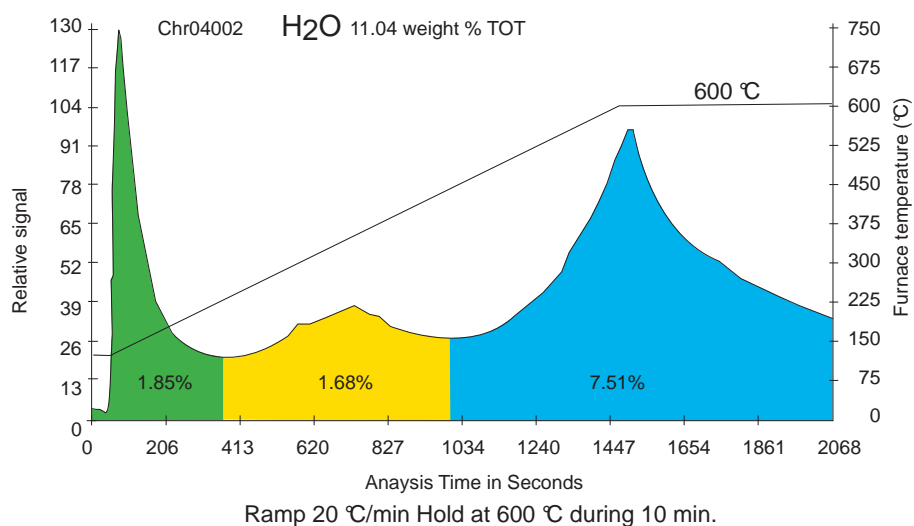
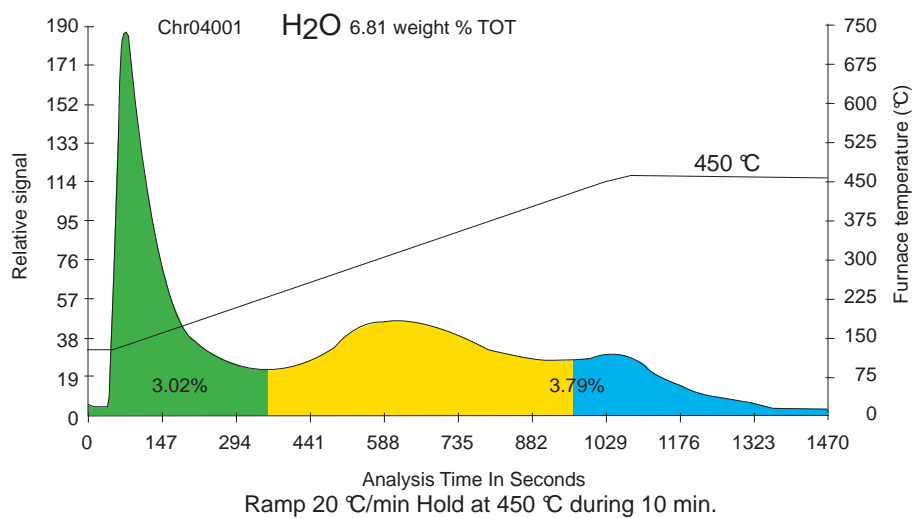


Figure B.3:

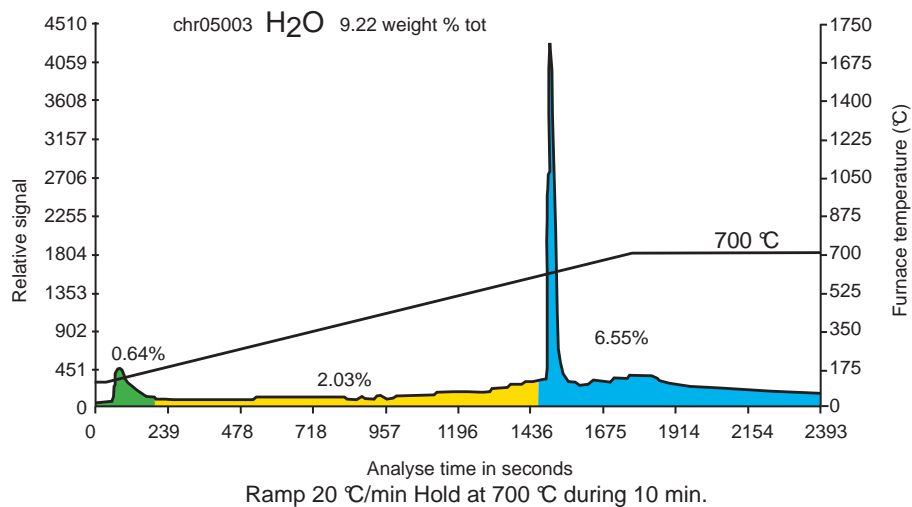
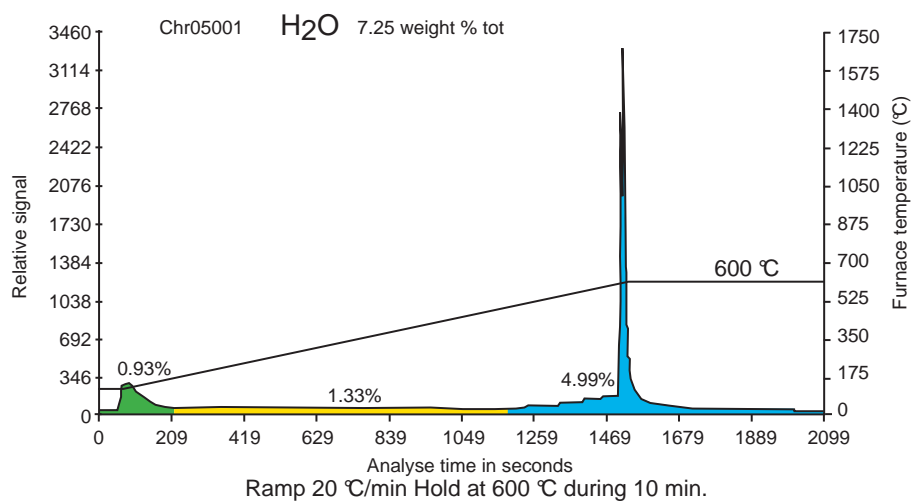
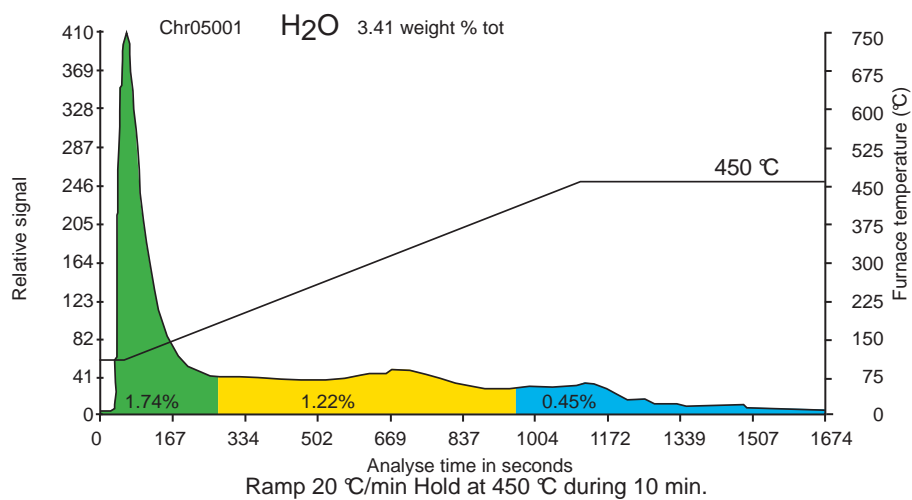


Figure B.4:

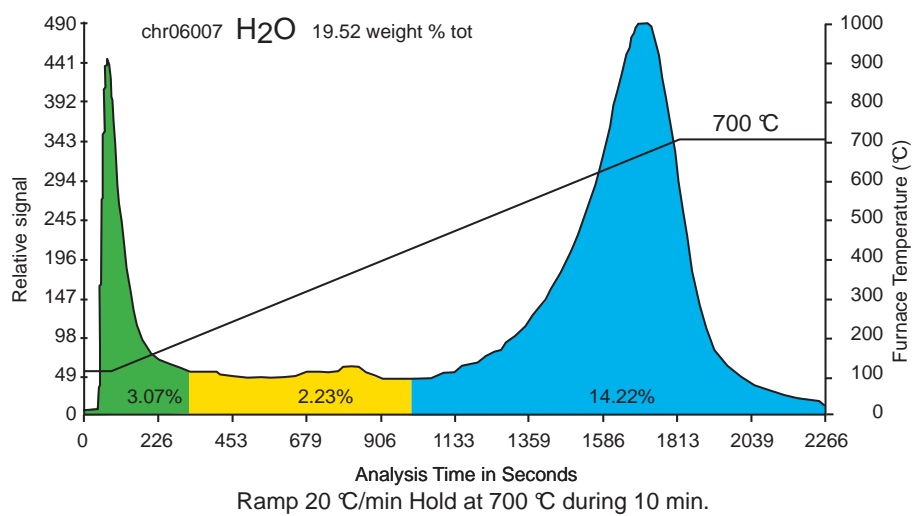
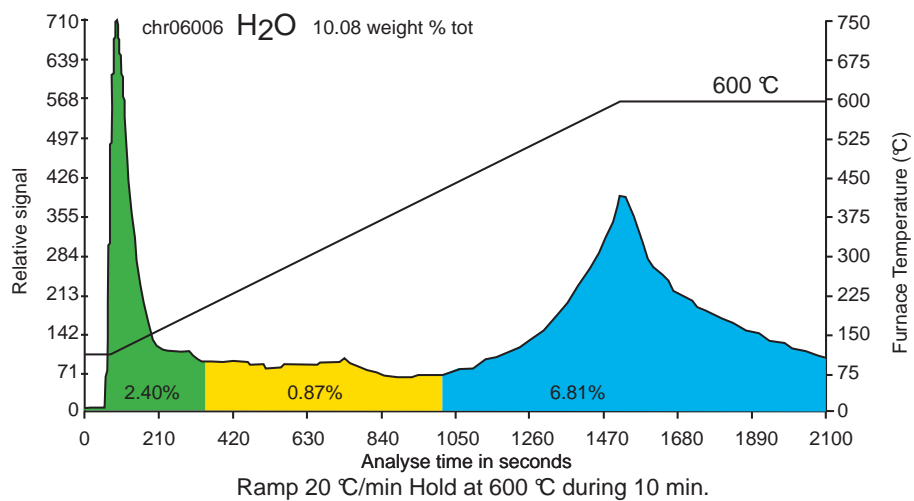
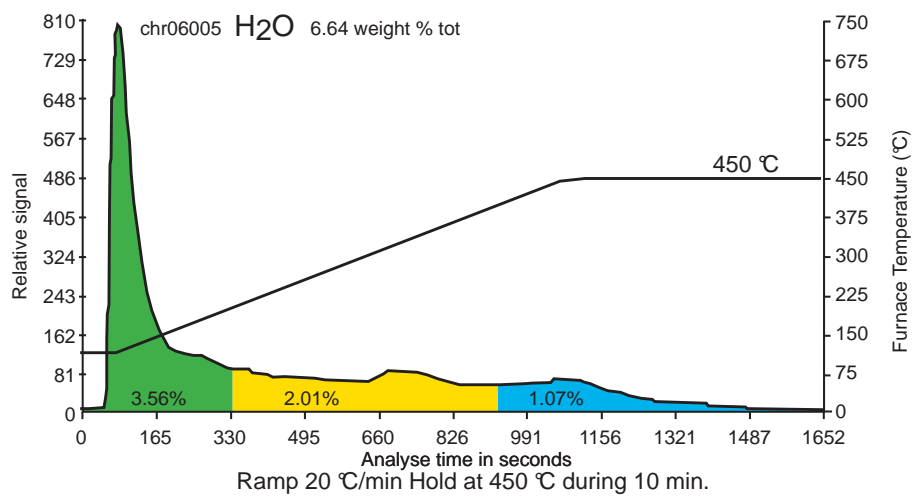


Figure B.5:

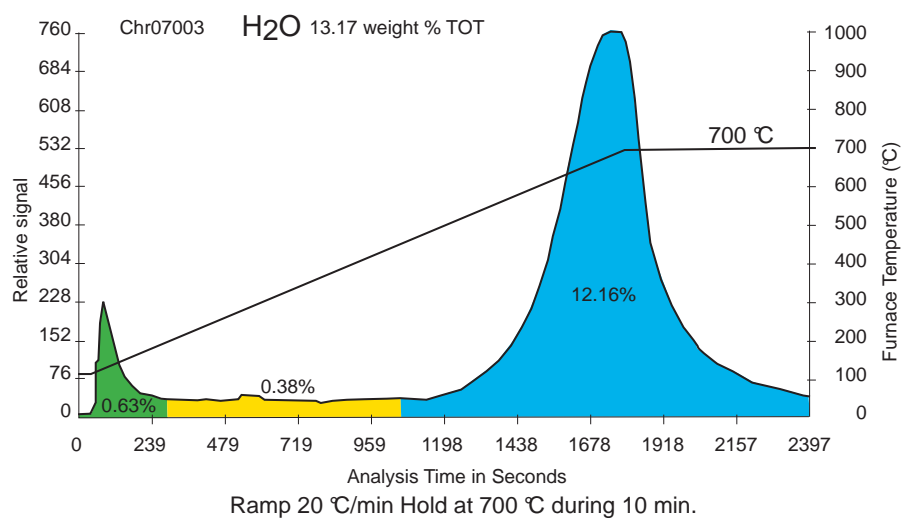
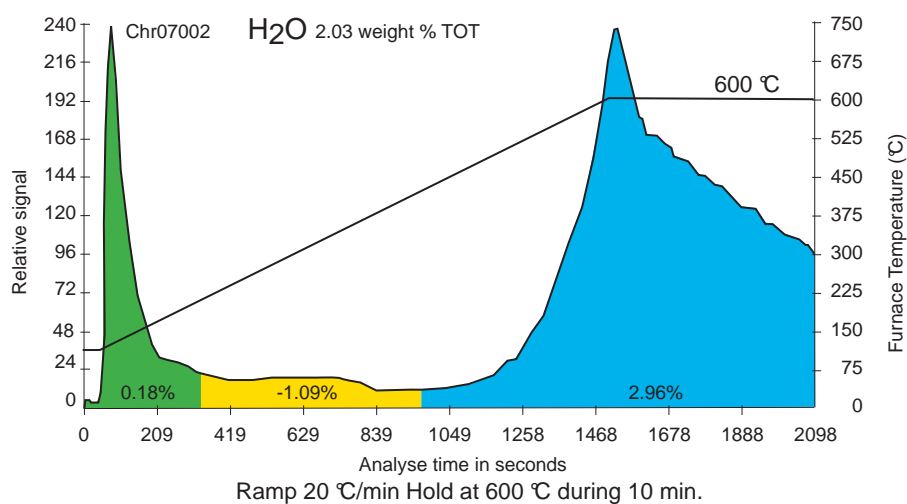
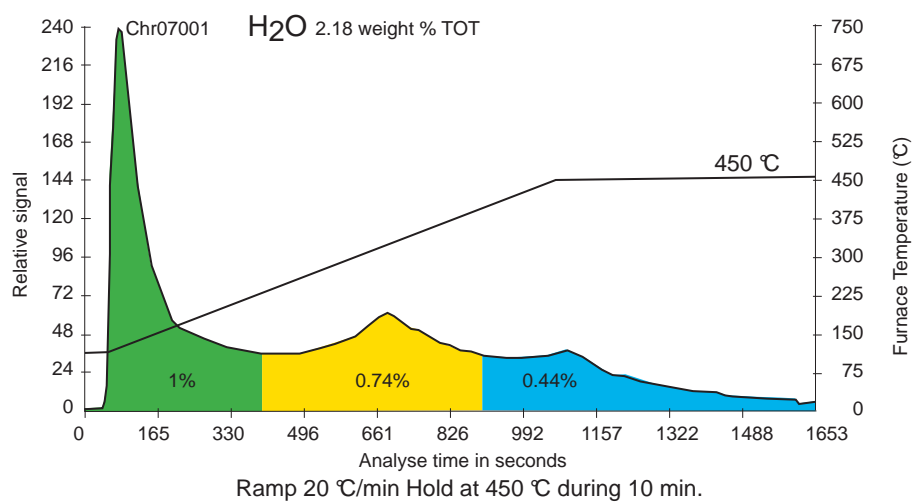


Figure B.6:

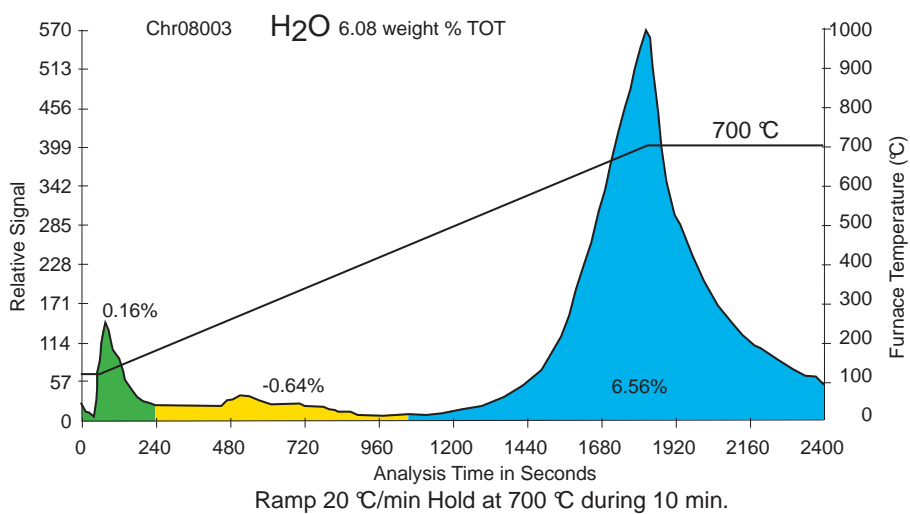
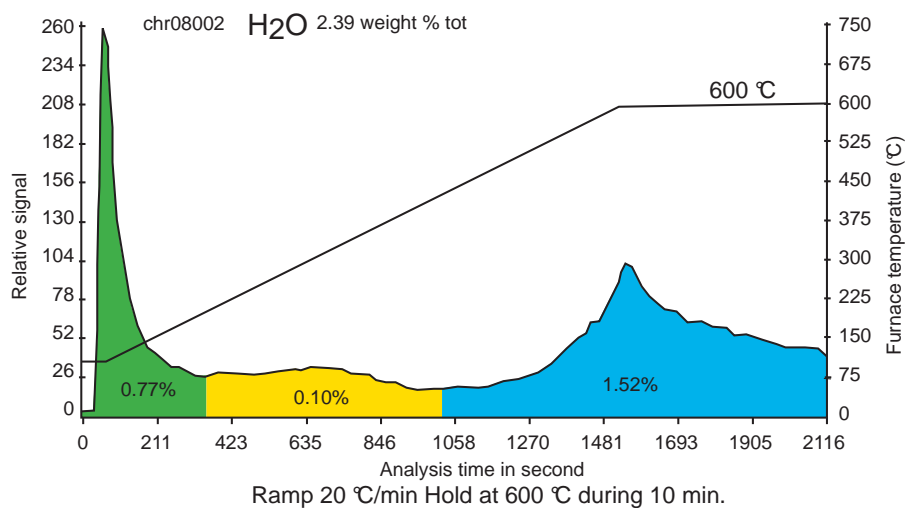
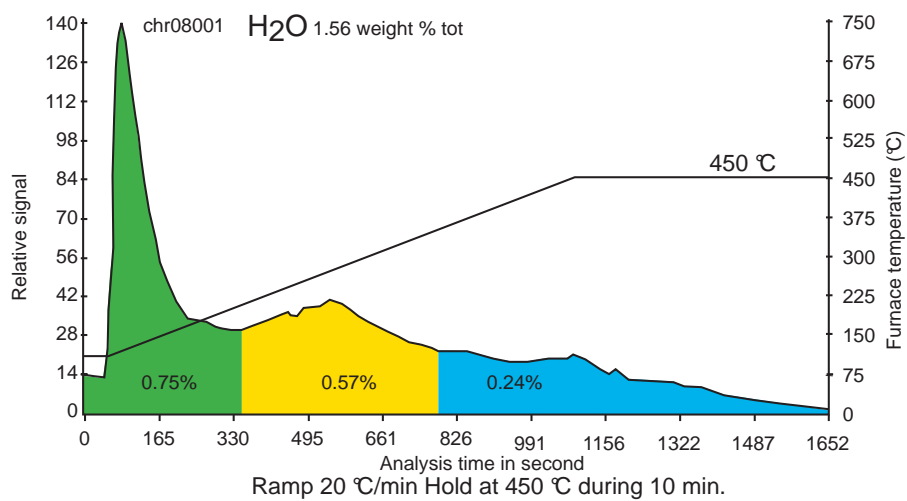


Figure B.7:

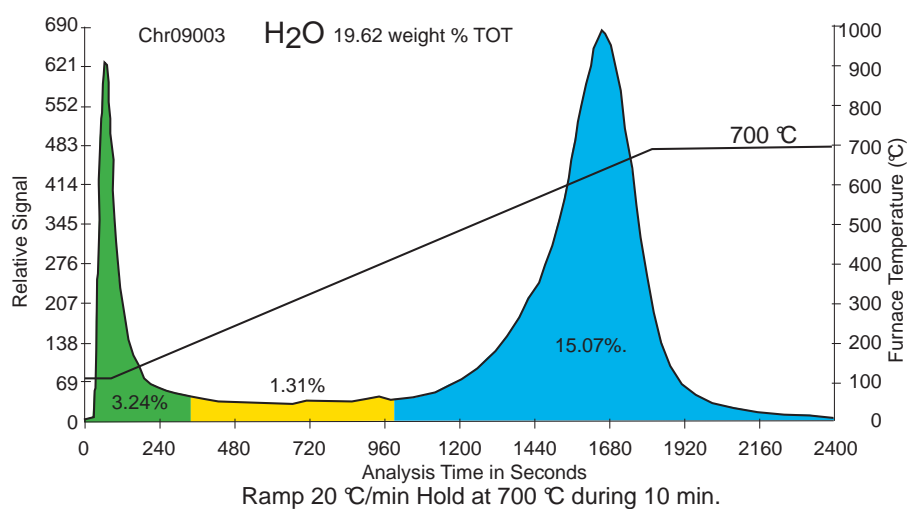
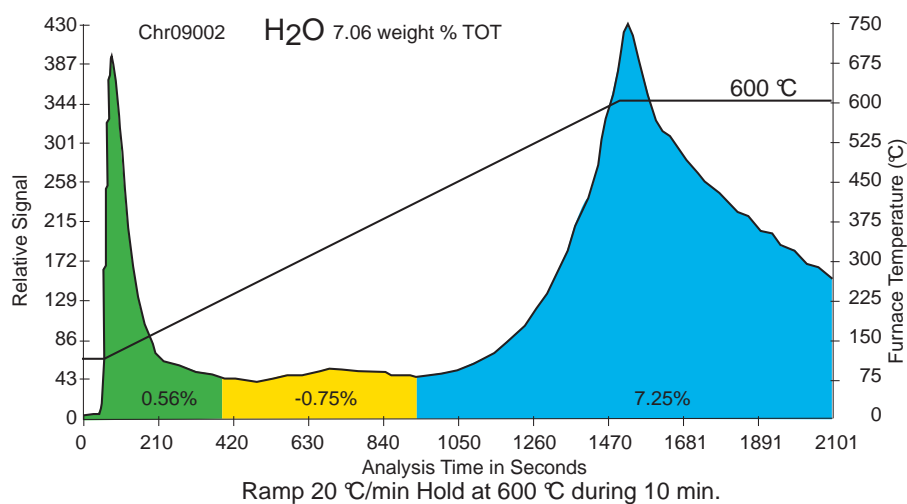
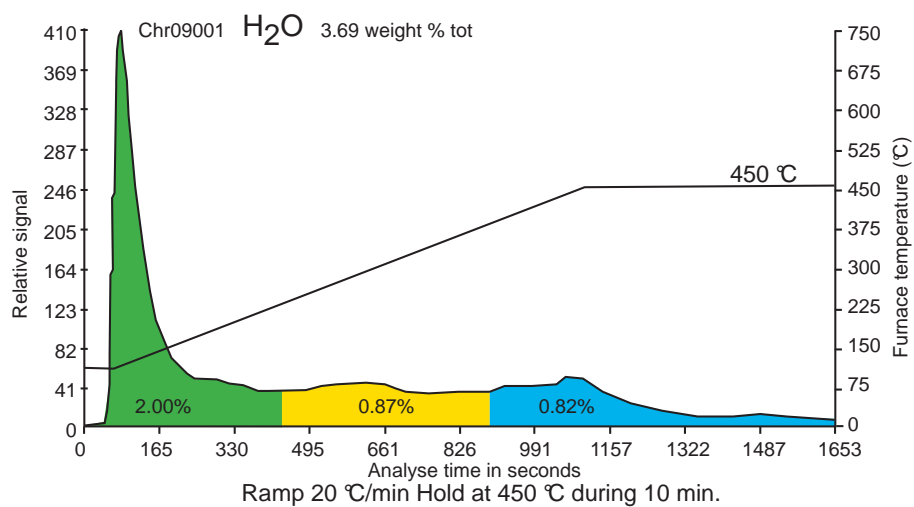
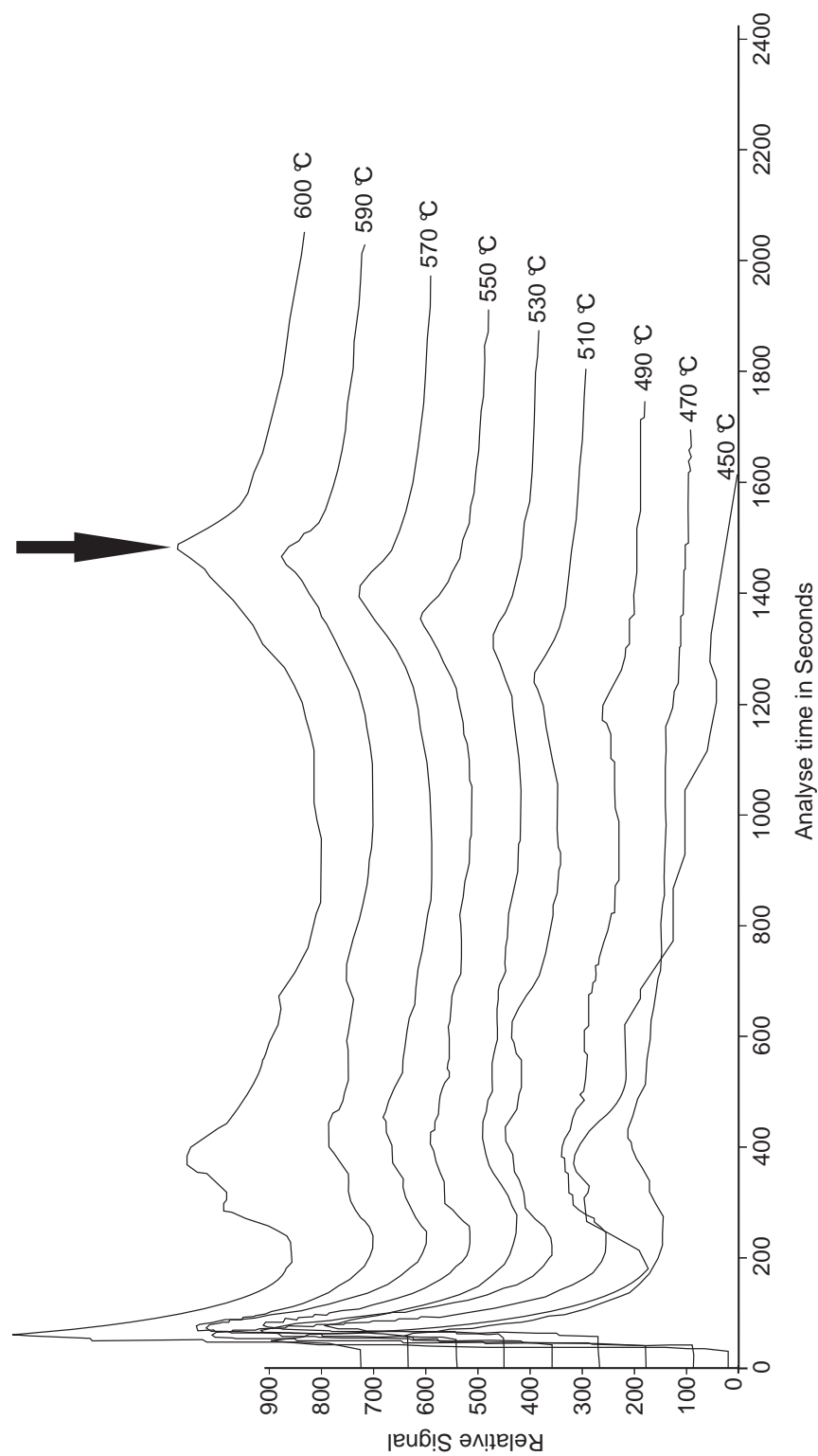


Figure B.8:



IR-Analysis: Chrysotile (Chr02000 sample). Ramp 20 °C/min. Hold at the indicated temperature during 10 min.

Figure B.9:

Bibliography

- [1] H.W. Kroto, J.R. Heath, S.C. O'Brien, R.F. Curl, R.E. Smalley, " C_{60} : Buckminsterfullerene" , *Nature*, 318, 162, 1985.
- [2] P.J.F. Harris, "Carbon nanotubes and related structures, new materials for the twenty-first century" , *Cambridge University Press*, 1999.
- [3] S. Iijima, "Helical microtubules of graphitic carbon" , *Nature*, 354, 56-68, 1991.
- [4] S. Ciraci, A. Buldum, I. P. Batra, "Quantum effects in electrical and thermal transport through nanowires" , *J. Phys.: Condens. Matter*, 13, R537–R568, 2003.
- [5] R. Tenne, L. Margulis, M. Genut, G. Hodes, "Polyhedral and cylindrical structures of tungsten disulphide" , *Nature*, 360, 444, 1992.
- [6] P. Mauron "Growth Mechanism and Structure of Carbon Nanotubes" , *phD thesis, University of Fribourg*, 136 p., 2003.
- [7] S.J. Tans, M.H. Devoret, H. Dai, A. Thess, R.E. Smalley, L.J. Geerligs, C. Dekker, "Individual single-wall carbon nanotubes as quantum wires" , *Nature*, 386, 474, 1997.
- [8] J.W.G. Wildöer, L.C. Venema, A.G. Rinzler, R.E. Smalley, C. Dekker, "Electronic structure of atomically resolved carbon nanotubes" , *Nature*, 391, 59-62, 1998.
- [9] T.W. Odom, J.-L. Huang, P. Kim, C.M. Lieber, "Atomic structure and electronic properties of single-walled carbon nanotubes" , *Nature*, 391, 62-64, 1998.
- [10] P. Kim, T.W. Odom, J.L. Huang, C.M. Lieber "Electronic density of states of atomically resolved single walled carbon nanotubes: Van Hoves singularities at end states" , *Phys. Rev. Lett.*, 82, 1225-1228, 1999.
- [11] C.T. White, T.N. Todorov, "Carbon nanotubes as long ballistic conductors" , *Nature*, 393, 240, 1998.
- [12] S. Frank, P. Poncharal, Z. Wang , W. de Heer, "Carbon nanotubes quantum resistors" , *Science*, 280, 1744, 1998.

- [13] S. Sanvito, Y.-K. Kwon, D. Tománek, C.J. Lambert, “Fractional quantum conductance in carbon nanotubes” , *Phys. Rev. Lett.*, 84, 1974, 2000.
- [14] Q.H. Wang, A.A. Setlur, J.M. Lauerhaas, J.H. Day, E.W. Seelig, R.P.H. Chang, “A nanotube-based field-emission flat panel display” , *Appl. Phys. Lett.*, 72, 2192, 1998.
- [15] S. Fan, M.G. Chopline, N.R. Franklin, T.W. Tombler, A.M. Cassel, H. Dai, “Self-oriented regular arrays of carbon nanotubes and their field emission properties” , *Science*, 283, 512, 1999.
- [16] S.J. Tans, A.R.M. Verschueren, C. Dekker, “Room-temperature transistor based on a single carbon nanotube” , *Nature*, 393, 49, 1998.
- [17] Y.Y. Wei, G. Eres, “Direct fabrication of carbon nanotubes circuits by selective area chemical vapor deposition on pre-patterned structures” , *Nanotechnology*, 11, 61, 2000.
- [18] Y. Huang, X. Duan, Q. Wei, C.M. Lieber, “Directed assembly of one-dimensional nanostructures into functional networks” , *Science*, 291, 630, 2001.
- [19] A.C. Dillon, K.M. Jones, T.A. Bekkedahl, C.H. Kiang, D.S. Bethune, M.J. Heben, “Storage of hydrogen in single-walled carbon nanotubes” , *Nature*, 386, 377, 1997.
- [20] H.D. Wagner, O. Lourie, Y. Feldman, R. Tenne, “Stress-induced fragmentation of multiwall carbon nanotubes in a polymer matrix” , *Appl. Phys. Lett.*, 72, 188, 1998.
- [21] J. Che, T. Cagin, W.A. Goddard III, “Thermal conductivity of carbon nanotubes” , *Nanotechnology*, 11, 65, 2000.
- [22] Y. Feldman, E. Wasserman, D.J. Srolovitch, R. Tenne, “High-rate, gas-phase growth of MoS₂ nested inorganic fullerenes and nanotubes” , *Science*, 267, 222, 1995.
- [23] M. Nath, A. Govindaraj, C.N.R. Rao, “Simple synthesis of MoS₂ and WS₂ nanotubes” , *Adv. Mater.*, 13, 283, 2001.
- [24] N.G. Chopra, R.J. Luyken, K. Cherrey, V.H. Crespi, M.L. Cohen, S.G. Louie, A. Zettl, “Boron nitride nanotubes” , *Science*, 269, 966, 1995.
- [25] I. Narita, T. Oku, “Synthesis of boron nitride nanotubes by using NbB₂, YB₆ and YB₆/Ni powders” , *Diamond and Related Materials*, 12, 1912, 2003.
- [26] D. Goldberg, A. Rode, Y. Bando, M. Mitome, E. Gamaly, B. Luther-Davies, “Boron nitride nanostructures formed by ultra-high-repetition rate laser ablation” , *Diamond and Related Materials*, 12, 1269, 2003.
- [27] Y. Ma, L. Qi, J. Ma, H. Cheng, “Micelle mediated synthesis of single crystalline selenium nanotubes” , *Adv. Mater.*, 16, 1023, 2004.

- [28] B. Mayers, B. Gates, Y. Yin, Y. Xia, "Large-scale synthesis of monodisperse nanorods of Se/Te alloys through a homogeneous nucleation and solution growth process" , *Adv. Mater.*, 13, 1380, 2001.
- [29] A. Abdelouas, W.L. Gong, W. Lutze, J.A. Shelnutt, R. Franco, I. Moura, "Using cytochrome C₃ to make selenium nanowires" , *Chem. Mater.*, 12, 1510, 2000.
- [30] B. Gates, B. Mayers, B. Cattle, Y. Xia, "Synthesis and characterization of uniform nanowires of trigonal selenium" , *Adv. Funct. Mater.*, 12, 219, 2002.
- [31] Z.Y. Jiang, Z.X. Xie, S.Y. Xie, X.H. Zhang, R.B. Huang, L.S. Zheng, "High purity trigonal selenium nanorods growth via laser ablation under controlled temperature" , *Chem. Phys. Letters*, 368, 425, 2003.
- [32] X. Jiang, B. Mayers, T. Herrichs, Y. Xia, "Direct synthesis of Se@CdSe nanocables and CdSe nanotubes by reacting cadmium salts with Se nanowires" , *Adv. Mater.*, 15, 1740, 2003.
- [33] N. Furuta, H. Itinose, N. Maruyama, Y. Ohasi, "Morphology and dislocation structure of tellurium whiskers grown from the vapor" , *Jpn. J. Appl. Phys.*, 11, 1113, 1972.
- [34] F. Fiévet, J.P. Lagier, M. Figlarz, "Preparing monodisperse metal powders in micrometer and submicrometer sizes by the polyol process" , *MRS Bull.*, December 29, 1989.
- [35] G. Wei, Y. Deng, Y.H. Lin, C.W. Nan, "Solvothermal synthesis of porous tellurium nanotubes" , *Chem. Phys. Lett.*, 372, 590, 2003.
- [36] B. Mayers, Y. Xia, "One-dimensional nanostructures of trigonal tellurium with various morphologies can be synthesized using a solution-phase approach" , *Journal of Mater. Chem.*, 12, 1875, 2002.
- [37] B. Mayers, Y. Xia, "Formation of tellurium nanotubes through concentration depletion at the surfaces of seeds" , *Adv. Mater.*, 14, 279, 2002.
- [38] C. Klein, C.S. Hurlbut, "Manual of mineralogy, 20th edition (after J.D. Dana)" , *John Wiley and Sons*, 1985.
- [39] F. Pundsack, "The properties of asbestos. I. The colloidal and surface chemistry of chrysotile" , *Journal of Phy. Chem.*, 59, 892, 1955.
- [40] N. Yoshinaga, S. Aomine, "Imogolite in some ando soils" , *Soil Sci. Plant Nutr.*, 8, 22, 1962.
- [41] V.C. Farmer, A.R. Fraser, J.M. Tait, "Synthesis of imogolite: A tubular aluminum silicate polymer" , *J.C.S. Chem. Comm.*, 240, 462, 1977.
- [42] P.D.G Cradwick, V.C. Farmer, J.D. Russell, C.R. Masson, K. Wada, N. Yoshinaga, "Imogolite, a hydrated aluminum silicate of tubular structure" , *Nature*, 240, 187, 1972.

- [43] M. Lahmani, C. Dupas, P. Houdy, "Les nanosciences 1. Nanotechnologies et nanophysique" , *Belin*, 2006.
- [44] W.I. Park, D.H. Kim, S.W. Jung, G.C. Yi, "Metalorganic vapor-phase epitaxial growth of vertically well-aligned ZnO nanorods" , *Appl. Phys. Lett.*, 80, 4232, 2002.
- [45] W. Johannes, D.W. Chipman, J.F. Hays, P.M. Bell, H.K. Mao, A.L. N. Boettcher, F. Seifer, "An interlaboratory comparison of piston-cylindre pressure calibration using the albite breakdown reaction" , *Contributions to Mineralogy and Petrology*, 24, 32, 1971.
- [46] S.R. Bohlen, E.J. Essene, A.L. Boettcher, "Reinvestigation and application of olivine - qtz - opx barometry" , *Earth and Planetary Science Letters*, 1, 47, 1980.
- [47] D.B. Williams, C.B. Carter, "Transmission electron microscopy, basics" , *Plenum Press*, 1996.
- [48] FEI and Philips, "XL SFEG Scanning electron microscopes, training course" , *FEI and Philips*, First Edition, 1998.
- [49] Leco corporation "Leco RC-412" , *Instruction manual: RC-412 multiphase carbon/hydrogen/moisture determinator*, 1992.
- [50] B. Devouard, A. Baronnet, "Axial diffraction of curved lattices: geometrical and numerical modelling. Application to chrysotile" , *Eur. J. Mineral.*, 7, 835, 1995.
- [51] A. Baronnet, M. Mellini, B. Devouard, "Sectors in polygonal serpentine. A model based on dislocations" , *Minerals*, 21, 330, 1994.
- [52] M. Mellini, "The crystal structure of lizardite 1T: hydrogen bounds and polytypism" , *Amer. Min.*, 62, 587, 1982.
- [53] K. Yada, "Study of chrysotile asbestos by a high resolution electron microscope" , *Acta. Cryst.*, 23, 704, 1967.
- [54] K. Yada, "Study of microstructure of chrysotile asbestos by high resolution electron microscopy" , *Acta. Cryst.*, 27, 659, 1971.
- [55] B.A. Cressey, E.J. Whittaker, "Five-fold symmetry in chrysotile asbestos revealed by transmission electron microscopy" , *Min. Mag.*, 57, 729, 1993.
- [56] E.J.W. Whittaker, "The diffraction of X-rays by a cylindrical lattice. II" , *Acta Cryst.*, 8, 261, 1955.
- [57] M.H. Hey, F.A. Bannister, "A note on the thermal decomposition of chrysotile" , *Min. Mag.*, 28, 333, 1948.

- [58] G.W. Brindley, J. Zussman, "A structural study of the thermal transformation of serpentine minerals to forsterite" , *Amer. Min.*, 42, 461, 1957.
- [59] M.C. Ball, H.F.W. Taylor, "An X-Ray study of some reactions of chrysotile" , *J. Appl. Chem.*, 13, 145, 1963.
- [60] H. de Souza Santos, K. Yada, "Thermal transformation of chrysotile studied by high resolution electron microscopy" , *Clays and Clay Minerals*, 27, 161, 1979.
- [61] M.C. Ball, H.F.W. Taylor, "The dehydration of chrysotile in air and under hydrothermal conditions" , *Mineral. Mag.*, 33, 467, 1963.
- [62] G.W. Brindley, R. Hayami, "Kinetics and mechanisms of dehydration and recrystallization of serpentine - I" , *Clays and Clay Minerals*, 34, 35, 1964.
- [63] G.W. Brindley, R. Hayami, "Mechanism of formation of forsterite and enstatite from serpentine" , *Mineral. Mag.*, 35, 189, 1965.
- [64] F. Pundsack, "The pore structure of chrysotile asbestos" , *J. Phys. Chem.*, 65, 30, 1961.
- [65] A.W. Naumann, W.H. Drescher, "The influence of sample texture on chrysotile dehydroxilation" , *Amer. Min.*, 51, 711, 1966.
- [66] S.A. Sapp, B.B. Lakshmi, C.R. Martin, "Template synthesis of bismuth telluride nanowires" , *Adv. Mater.*, 11, 402, 1999.
- [67] T.E. Hubert, R. Calcao, "Thermoelectric properties of Bi And Bi₂Te₃ composites" , *In 16th International Conference on Thermoelectrics, Dresden, Germany*, American Institute of Physics Press, 1997.
- [68] C. Huber, M. Sadoqi, T. Huber, D. Chacko, "Microengineered conducting composites from nanochannel templates advanced materials" , *Adv. Mater.*, 7, 316, 1995.
- [69] S. Sander, R. Gronsky, T. Sands, A.M. Stacy, "Structure of bismuth telluride nanowire arrays fabricated by electrodeposition into porous anodic alumina templates" , *Chem. Mater.*, 15, 335, 2003.
- [70] M.S. Ivanova, Y.A. Kumzerov, V.V. Poborchii, Y.V. Ulashkevich, V.V. Zhuravlev, "Ultrathin wires incorporated within chrysotile asbestos nanotubes: optical and electrical properties" , *Microporous Mater.*, 4, 319, 1995.
- [71] S.G. Romanov, C.M. Sotomayor Torres, "Nanoscale science and technology" , *Edited by N. Garcia (Kluwer Academic Publishers, Dordrecht)*, 1998.

- [72] P.A. Webb, "An introduction to the physical characterization of materials by mercury intrusion porosimetry with emphasis on reduction and presentation of experimental data" , *Micromeritics Instrument Corp.*, 22 p, 2001.
- [73] E. Dujardin, T.W. Ebbesen, H. Hiura, K. Tanigaki, "Capillarity and wetting of carbon nanotubes" , *Science*, 265, 1850, 1994.
- [74] A.K. Helmy, E.A. Ferreiro, S.G. Bussetti, "The surface energy of talc" , *Journal of Colloid and Interface Science*, 285, 314, 2005.
- [75] Z. Wang, P. Lazor, S.K. Saxena, "A simple model for assesing the high pressure melting of metals: nickel, aluminum and platinum" , *Physica B*, 293, 408, 2001.
- [76] D. Mainprice, G. Barruol, W.B. Isamaïl, "The seismic anisotropy of the earth mantle: From single crystal to polycrystal" , *Geophysical Monograph*, 237, 117, 2000.
- [77] "Handbook of chemistry and physics" , *CRC Press*, 1995-1996.
- [78] W.B. Daniels, C.S. Smith, "Pressure derivative of the elastic constant of copper, silver and gold to 10'000 bar" , *Physical Review*, 111, 713, 1958.
- [79] P.E. Van Camp, V.E. Van Doren, J.T. Devereese, "Ground-state and electronic properties of covalent solids" , *Physical Review B*, 38, 12675, 1988.
- [80] D. He, Y. Zhao, L.L. Daemen, J. Qian, K. Lokshin, T.D. Shen, J. Zhang A.C. Lawson, "Thermoelastic and texture behavior of aluminum at high pressure and high temperature investigated by in situ neutron diffraction" , *J. of Appl. Phys.*, 95, 4645, 2004.
- [81] L.A. Davis, R.B. Gordon, "Compression of mercury at high pressure" , *J. of Chem. Phys.*, 46, 2650, 1966.
- [82] X.Y. Liu, M.S. Mo, X.Y. Chen, Y.T. Quian, "A rational redox route for the synthesis of tellurium nanotubes" , *Inorg. Chem. Comm.*, 7, 257, 2004.
- [83] M. Biemann, "Surface scientific aspects of materials relevant to tribology" , *phD thesis, University of Fribourg*, 126 p., 2004.
- [84] www.veeco.com
- [85] K. Wada, N. Yoshinaga, "The structure of imogolite" , *Amer. Min.*, 54, 50, 1969.
- [86] J.D. Russell, W.J. McHardy, A.R. Fraser, "Imogolite: a unique aluminosilicate" , *Clay Min.*, 8, 87, 1969.
- [87] S. Wada, K. Wada, "Effects of Substitution of germanium for silicon in imogolite" , *Clays and Clay Minerals*, 30, 123, 1982.

- [88] K. Wada, "A structural scheme of soil allophane" , *Amer. Min.*, 52, 690, 1967.
- [89] F. Ohashi, S. Tomura, K. Akaku, S. Hayashi, S.I. Wada, "Characterization of synthetic imogolite nanotubes as gas storage" , *J. of Material Sc.*, 39, 1799, 2004.
- [90] G.H. Koenderink, S.G.J.M. Kluijtmans, A.P. Philipse, "Note on the synthesis of colloidal imogolite fibers" , *J. of Colloid and Interface Sc.*, 216, 429, 1999.
- [91] S. Mukherjee, V.M. Bartlow, S. Nair, "Phenomenology of the growth of single-walled aluminosilicate and aluminogermanate nanotubes of precise dimensions" , *Chem. Mater.*, 17, 4900, 2005.
- [92] M.A. Wilson, G.S.H. Lee, R.C. Taylor, "Tetrahedral rehydration during imogolite formation" , *J. of Non-Crystalline Solids*, 296, 172, 2001.
- [93] K. Yamamoto, H. Otsuka, S.I. Wada, D. Sohn, A. Takahara, "Transparent polymer nanohybrid prepared by in situ synthesis of aluminosilicate nanofibers in (poly)vinyl alcohol solution" , *Soft Matter*, 1, 372, 2005.
- [94] S. Imamura., T. Kokubu, T. Yamashita, Y. Okamoto, K. Kajiwara, H. Kanai, "Shape-selective copper-loaded imogolite catalyst" , *J. of Catalysis*, 160, 137, 1996.
- [95] W.C. Ackermann, D.M. Smith, J.C. Huling, Y.W. Kim, G. Bailey, C.J. Brinkertps, "Gas/vapor adsorption in imogolite : a microporous tubular aluminosilicate" , *Langmuir*, 9, 1051, 1993.
- [96] S.I. Wada , A. Eto, K. Wada, "Synthetic allophane and imogolite" , *J. Soil Sci.*, 30, 347, 1979.
- [97] L.A. Bursill, J.L. Peng, L.N. Bourgeois, "Imogolite: an aluminosilicate nanotube material" , *Philos. Mag. A*, 1, 105, 2002.
- [98] S.J. Van der Gaast, K. Wada, S.I. Wada, Y. Kakuto, "Small-angle X-Ray powder diffraction, morphology, and structure of allophane and imogolite" , *Clays Clay Miner.*, 33, 237, 1985.
- [99] www.bam.de
- [100] R.A. Young, "Introduction to the Rietveld method," , *The Rietveld Method*, Oxford Science Publications, 1996.
- [101] K. Wada, N. Yoshinaga, H. Yotsumoto, K. Ibe, S. Aida, "High resolution electron micrographs of imogolite" , *Clay Min.*, 8, 487, 1970.
- [102] S. Wada, "Imogolite synthesis at 25°C" , *Clays Clay Miner.*, 35, 379, 1987.

Appendix C

Curriculum Vitae

Cédric Métraux

19.02.1974, single

Route des Pervenches 1

1700, Fribourg

026 466 16 12

Education

- **University of Fribourg**
PhD in Technical Mineralogy, 2008
- **ETH Zürich**
Postgraduate Study in Geographical Information Systems, 2004
- **University of Fribourg**
Postgraduate Diploma in Computer Science, 2002
- **University of Neuchâtel**
Master in Geosciences, 2000
- **Gymnase cantonal, Neuchâtel**
Baccalauréat en langues modernes, 1993

Work History

- **Geographical information systems engineer**
swisstopo
 - designed and implemented data exchange architectures.
 - developed, documented and maintained geographical information systems.
 - performed configuration management of systems.
 - taught users in training classes.

2005 - Present
Bern
- **Geographical information systems engineer**
CREALP
 - developed an application for digitizing geological maps using GIS.

2004
Sion
- **Geographical information systems specialist**
Geological Survey, Federal Office for Water and Geology
 - migrate geological maps on a geographical information system.

2004
Bern
- **Internship as geologist**
Geological Survey, Federal Office for Water and Geology
 - migrate geological maps on a geographical information system.
 - create a database for the "Geological Atlas" administration.

2003
Bern
- **Informatic project**
Hydrological Survey, Federal Office for Water and Geology
 - Creating a Java/XML/Wap application to monitor water parameters.

2002
Bern

Skills

Languages: French, German, English, Spanish

Programming languages: C#, .NET, AML, VBA, Java, Python, shell scripting, SQL

Operating Systems: IBM AIX, Windows, Linux

Applications: ArcGIS, ArcInfo, Oracle 10g, Visual Studio

Miscellaneous: System administration in UNIX, software configuration management